

# An in-situ experimental-numerical approach for interface delamination characterization

**Citation for published version (APA):**

Murthy Kolluri, N. V. V. R. (2011). *An in-situ experimental-numerical approach for interface delamination characterization*. [Phd Thesis 1 (Research TU/e / Graduation TU/e), Mechanical Engineering]. Technische Universiteit Eindhoven. <https://doi.org/10.6100/IR714598>

**DOI:**

[10.6100/IR714598](https://doi.org/10.6100/IR714598)

**Document status and date:**

Published: 01/01/2011

**Document Version:**

Publisher's PDF, also known as Version of Record (includes final page, issue and volume numbers)

**Please check the document version of this publication:**

- A submitted manuscript is the version of the article upon submission and before peer-review. There can be important differences between the submitted version and the official published version of record. People interested in the research are advised to contact the author for the final version of the publication, or visit the DOI to the publisher's website.
- The final author version and the galley proof are versions of the publication after peer review.
- The final published version features the final layout of the paper including the volume, issue and page numbers.

[Link to publication](#)

**General rights**

Copyright and moral rights for the publications made accessible in the public portal are retained by the authors and/or other copyright owners and it is a condition of accessing publications that users recognise and abide by the legal requirements associated with these rights.

- Users may download and print one copy of any publication from the public portal for the purpose of private study or research.
- You may not further distribute the material or use it for any profit-making activity or commercial gain
- You may freely distribute the URL identifying the publication in the public portal.

If the publication is distributed under the terms of Article 25fa of the Dutch Copyright Act, indicated by the "Taverne" license above, please follow below link for the End User Agreement:

[www.tue.nl/taverne](http://www.tue.nl/taverne)

**Take down policy**

If you believe that this document breaches copyright please contact us at:

[openaccess@tue.nl](mailto:openaccess@tue.nl)

providing details and we will investigate your claim.

**An *in-situ* experimental-numerical approach  
for interface delamination characterization**

This research was carried out under the project number MC2.05235 in the framework of the Research Program of the Materials innovation institute (M2i) in the Netherlands ([www.m2i.nl](http://www.m2i.nl)).

CIP-DATA LIBRARY TECHNISCHE UNIVERSITEIT EINDHOVEN

Murthy Kolluri, N.V.V.R

An *in-situ* experimental-numerical approach for interface delamination characterization.

Eindhoven University of Technology, 2011.

Proefschrift.

A catalogue record is available from the Eindhoven University of Technology Library.

ISBN: 978-90-77172-75-9

This thesis is prepared with L<sup>A</sup>T<sub>E</sub>X<sub>2</sub> $\epsilon$

Cover design: Paul Verspaget Grafische Vormgeving-Communicatie

Printed by the Universiteitsdrukkerij TU Eindhoven, Eindhoven, The Netherlands.

# **An *in-situ* experimental-numerical approach for interface delamination characterization**

## **PROEFSCHRIFT**

ter verkrijging van de graad van doctor aan de  
Technische Universiteit Eindhoven, op gezag van de  
rector magnificus, prof.dr.ir. C.J. van Duijn, voor een  
commissie aangewezen door het College voor  
Promoties in het openbaar te verdedigen  
op maandag 9 mei 2011 om 16.00 uur

door

**Naga Veera Venkata Ramana Kolluri Murthy**

geboren te Rajanagaram, India

Dit proefschrift is goedgekeurd door de promotor:

prof.dr.ir. M.G.D. Geers

Copromotoren:

dr.ir. J.P.M. Hoefnagels

dr.ir. J.A.W. van Dommelen

*To my beloved wife and parents*



# Contents

---

Summary	xi
<b>1 Introduction</b>	<b>1</b>
1.1 Industrial relevance and motivation	1
1.2 Goal	2
1.3 Literature	3
1.4 Strategy	4
1.5 Outline of the thesis	5
<b>2 <i>In-situ</i> characterization of interface delamination by a new miniature mixed mode bending setup</b>	<b>7</b>
2.1 Introduction	8
2.2 Design of the miniaturized mixed mode bending (MMMB) apparatus	10
2.2.1 New configuration for mixed mode loading	10
2.2.2 Design of the test apparatus	13
2.2.3 Finite element analysis	15
2.3 Validation	19
2.4 Experimental results and discussion	20
2.5 Conclusion	25
<b>3 An improved miniature mixed mode delamination setup for <i>in-situ</i> microscopic interface failure analyses</b>	<b>27</b>
3.1 Introduction	28
3.2 Brief review of the original MMMB setup	30
3.2.1 Advantages of the MMMB setup	32
3.2.2 Limitations - Motivation for an improved design	33
3.3 Improved Miniature Mixed Mode Bending setup	33
3.3.1 Optimization of the elastic hinge positions	33
3.3.2 Optimization of the hinge geometry	35
3.3.3 Final improved MMMB design	37
3.3.4 Clearance and Robustness of the setup	38
3.4 Analysis of the new improved MMMB setup	40
3.4.1 Validation and accuracy assessment	40



3.4.2	Finite Element Analysis . . . . .	41
3.5	Study of coated copper lead frame - molding compound epoxy (CuLF-MCE) . . . . .	42
3.5.1	Experimental procedure . . . . .	42
3.5.2	Results and discussion . . . . .	43
3.6	Conclusions . . . . .	48
<b>4</b>	<b>Modeling and characterization of irreversible mixed mode interface delamination using a cohesive zone with combined damage and plasticity</b>	<b>51</b>
4.1	Introduction . . . . .	52
4.2	Irreversible unloading-reloading: a combined damage-plasticity description . . . . .	55
4.2.1	Damage formulation . . . . .	56
4.2.2	Plasticity formulation . . . . .	58
Normal yielding	. . . . .	58
Tangential yielding	. . . . .	60
4.2.3	Combined plasticity-damage formulation . . . . .	60
4.3	Selection of a basis CZ law . . . . .	62
4.4	Extension of improved Xu-Needleman model with damage and plasticity . . . . .	64
4.4.1	Exponential cohesive zone law proposed by Van den Bosch et al.	64
4.4.2	Improved Xu-Needleman model with combined plasticity-damage unloading . . . . .	66
Full damage	. . . . .	66
Full Plasticity	. . . . .	66
Combined plasticity-damage	. . . . .	67
4.5	Model application: Computational case study . . . . .	67
4.6	Extraction of cohesive zone parameters . . . . .	71
4.6.1	Mode I cohesive zone parameter determination . . . . .	72
4.6.2	Mode II parameter determination . . . . .	74
4.6.3	Determination of the plastic limit . . . . .	75
4.7	Conclusions . . . . .	76
<b>5</b>	<b>A semi-analytical approach for the separation of interfacial toughness and structural plastic dissipation in a delamination experiment</b>	<b>79</b>
5.1	Introduction . . . . .	80
5.2	Procedure to extract interface fracture toughness . . . . .	85
5.2.1	Case 1: Structural plasticity, no plasticity in the fracture process zone at the interface . . . . .	85
5.2.2	Case 2: Structural plasticity and plasticity within the fracture process zone at the interface . . . . .	87
5.3	Numerical verification . . . . .	89
5.3.1	Summary of the irreversible interface model . . . . .	90
5.3.2	Verification of the assumptions . . . . .	91
5.3.3	Numerical verification of the approach . . . . .	95

---

5.4	Application: determination of the interface fracture toughness in CuLF-MCE . . . . .	95
5.5	Conclusions . . . . .	99
<b>6</b>	<b>Characterization of industrially relevant interface structures</b>	<b>101</b>
6.1	Introduction . . . . .	101
6.2	Sample specification . . . . .	102
6.3	Specimen preparation for digital image correlation . . . . .	103
6.4	Experimental results and discussion . . . . .	106
6.4.1	Measurement of CERR versus mode angle . . . . .	106
6.4.2	Extraction of cohesive zone parameters . . . . .	107
	Extraction of mode I traction-separation law . . . . .	107
	Mode II parameter extraction . . . . .	112
6.5	Conclusions . . . . .	113
<b>7</b>	<b>Conclusion and Recommendations</b>	<b>115</b>
7.1	Conclusions . . . . .	115
7.2	Recommendations . . . . .	119
	<b>Bibliography</b>	<b>121</b>
	<b>Samenvatting</b>	<b>133</b>
	<b>Acknowledgements</b>	<b>137</b>
	<b>Curriculum Vitae</b>	<b>141</b>



# An *in-situ* experimental-numerical approach for interface delamination characterization

## Summary

---

Interfacial delamination is a key reliability challenge in composites and micro-electronic systems due to (high density) integration of dissimilar materials. Delamination occurs due to significant stresses generated at the interfaces, for instance, caused by thermal cycling due to the mismatch in thermal expansion coefficient and Poisson's ratio of the adherent layers. Predictive finite element models are generally used to minimize delamination failures during the design and optimization of these materials and systems. Successful prediction, however, requires a relevant interface model that can capture the observed (irreversible) crack initiation and propagation behavior in experiments. To this end, dedicated delamination experiments with *in-situ* microscopic visualization are needed to identify the relevant delamination mechanism(s) and to accurately measure the interface properties, such as the interface toughness, as a function of mode mixity (i.e. loading angle). Hence, the goal of this research is to develop experimental-numerical tools required for accurate characterization and prediction of interface delamination.

As a first step to reach this goal, a novel Miniature Mixed Mode Bending (MMMB) delamination setup, which enables *in-situ* characterization of interface delamination in miniature multi-layer structures, was designed and realized. This setup employs an inventive loading configuration to sensitively measure global load-displacement delamination curves for the full range of mode mixities from which the interface toughness or Critical Energy Release Rate (CERR) can be determined, while it was designed with sufficiently small dimensions to fit in the chamber of a scanning electron microscope or under an optical microscope for detailed real-time fracture analysis during delamination. The performance of the setup was assessed using dedicated test samples, supported by finite element analyses. The measurement concept was successfully validated on homogeneous bilayer samples with a glue interface system. The validation experiments also revealed room for improvement of the measurement accuracy, robustness, and applicability. Therefore, further optimization in the design was performed and an improved version of the MMMB setup was developed. This setup can access a considerably larger range of interface systems, shows significantly higher accuracy and reproducibility in load-displacement measurements, and is more robust. The potential of the new *in-situ* experimental technique for interface parameter identification was also illustrated. For instance, high resolution *in-situ* SEM imaging during delamination allows for measurement of the strain maps and crack opening displacement (COD) fields using digital image correlation in addition

to the identification of the delamination failure mechanism.

*In-situ* SEM observation of delamination in different interface structures reveals failure mechanisms ranging from interface damage to interface plasticity. Hence, an irreversible model description of the interface behavior that can capture the observed unloading-reloading responses is needed for accurate prediction of, for instance, crack branching and crack propagation at multiple interfaces using predictive finite element models. Therefore, a combined damage and plasticity formulation was presented that is suitable for modeling of the unloading response of an interface ranging from full damage to full plasticity, while it introduces a minimum number of model parameters that can be experimentally determined. The unloading model can be used with the existing mixed-mode cohesive zone laws that describe the interface loading behavior. The relevance and applicability of the unloading model was demonstrated, in combination with the existing improved Xu-Needleman mixed mode cohesive law, by modeling the observed combined damage-plasticity unloading response of the above-mentioned glue interface system. In addition, a procedure to identify the model parameters has been presented.

Permanent deformation of the sample structure often occurs during delamination tests, particularly, if the layers forming the interface are ductile and the interface is strong. Therefore, accurate determination of the interface fracture toughness requires identification and separation of the contribution of structural plasticity to the total energy dissipation, taking into account the presence of plasticity mechanisms within the fracture process zone at the interface that contribute to the interface fracture toughness. To this end, a semi-analytical approach accounting for the structural plasticity in the sample layers was developed, in order to obtain an accurate value of the interface fracture toughness in a mode I experiment. The approach was numerically verified by employing a finite element model with cohesive zone elements (at the interface). The proposed approach was experimentally assessed by characterizing the interface fracture toughness of industrially relevant copper lead frame-molding compound epoxy (CuLF-MCE) structures with different layer thicknesses.

In summary, the combined application of *in-situ* MMMB experiments, the analytical procedure to determine the CERR, and the cohesive zone model with the parameter identification procedure allows for accurate characterization of the delamination mechanism(s) and prediction of the interface mechanics. As a demonstration, industrially relevant coated CuLF-MCE and uncoated CuLF-white molding compound (WMC) interface systems have been characterized in detail using the developed experimental tools.

## CHAPTER ONE

# Introduction

---

### Abstract

The industrial relevance and motivation for characterization and prediction of interfacial delamination are outlined. Then, the goal of the thesis, existing methods for delamination characterization and modeling followed by the strategy used to achieve the goal are discussed. Finally, an outline of the thesis is given.

### 1.1 Industrial relevance and motivation

In the past century, the ever increasing demand from the aerospace industry for lightweight structures with superior mechanical and physical properties has led to the development of several composite materials with many different combinations of matrix and reinforcement materials. On the other hand, the demand for continuous miniaturization and multi-functionality of electronic devices led to the development of new packaging technologies like "system in packages" in which multiple, thin, stacked layers manufactured using different materials and processes are integrated in a single package to achieve multi-functionality. The common feature in both systems (composites and electronic package) is that superior properties come along with a high density of interfaces that are formed between dissimilar materials. Therefore, interface integrity is inherently crucial for the reliability and performance of these systems. In spite of many efforts [1, 2] to improve the mechanical properties of these interfaces, interface delamination is often identified as the prominent failure mechanism in many of the modern interface structures ranging from micro-electronic packages [3–5], advanced aerospace composite structures [6–8] to the adhesive joints in honeycomb sandwich structures [8, 9] and wind turbine blades [10]. Figure 1.1 show the examples of delamination failures observed in a typical lead frame based

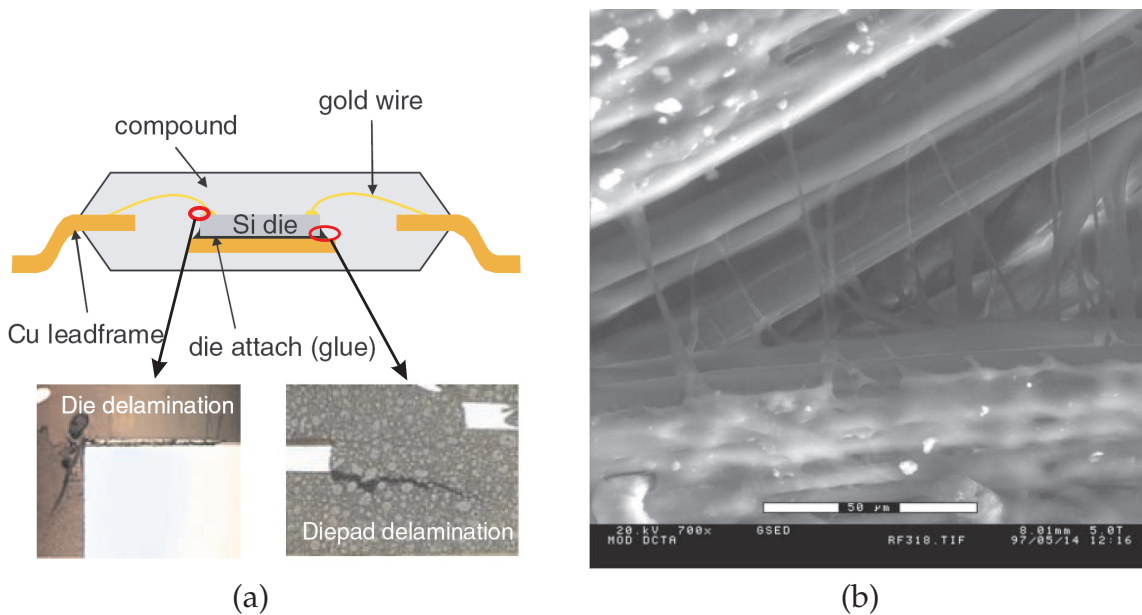


**Figure 1.1:** (Example of delamination failures in (a) lead frame based package [5] and (b)  $0^\circ/90^\circ$  ultra high molecular weight polyethylene composite [8].

micro-system package and a composite material. Delamination occurs mainly due to significant stresses generated at these interfaces during thermal cycling, triggered by the mismatch of the coefficient of thermal expansion (CTE) and the Poisson's ratio of the adherent layers or by mechanical loading of the structure. No adequate methodologies are currently available for the proper characterization and prediction of interfacial failure in these systems. As a consequence, the industry is still heavily depending on trial-and-error methods for product/process development. Predictive finite element models are required to minimize delamination failures during the design and optimization of these materials and systems. Successful prediction, however, requires a relevant interface model that can capture the observed (irreversible) crack initiation and propagation behavior in experiments.

## 1.2 Goal

To minimize the delamination failures and to improve the design rules of these products a generic experimental-numerical methodology that can accurately characterize and predict interface delamination is needed. Therefore, the goal of this thesis is to develop such a methodology that provides all the required tools, from an experimental setup to a numerical model, which are suitable for characterizing and predicting delamination failures:

- for a broad range of dissimilar material interfaces,
- over the full range of mixed mode loading conditions,

- over the complete (cyclic) loading-delamination-unloading path to which the interface is subjected.

In addition, the experimental setup should provide a stable crack growth during the experiment and the whole methodology should be applicable for (industrially relevant) cases where there is plasticity in the layers and at the interface.

## 1.3 Literature

In the literature, many experimental techniques are available for characterization of delamination, see for instance references [11–27], where it is noted that this is far from a complete list. There are techniques that are more specific and applicable for testing certain types of interface system. For example, indentation based techniques [15, 16, 18] are mostly used for testing brittle interfaces between a thin film and a substrate. Conversely, other techniques [12, 27], which are based on in-plane loading or super-layer methods, can be generally applicable but require manipulation of the thickness of the layers (with extensive specimen preparation) to achieve different mode mixities. Moreover, the stable crack growth regime and unloading regime are typically not probed in these experiments. Various other methods have been presented in the literature that employ mechanical loading on adherent layers [11, 13, 17, 19–24, 26] to trigger delamination. Most of these methods (i.e. based on mechanical loading of adherent layers) use a fracture mechanics approach where the critical load for delamination together with the crack length of the specimen are used in combination with analytical energy release rate formulas to obtain the interface fracture toughness. The associated assumptions involving the material behavior of the adherent layers and the interface limit the applicability of these approaches, for instance when there is a large fracture process zone at the interface or when the adherent layers are plastically deforming. On the contrary, an experimental approach that allows to find interface parameters such as the interface toughness without any assumptions about the fracture processes at the interface is highly preferred. There is much evidence in the literature [28–33] showing that plasticity often does occur in the adherent (bulk) layers, particularly, if the layers forming the interface are ductile and the interface is strong. Consequently, it has been reported that large errors in the measurement of the interface fracture toughness can occur if these bulk plastic dissipations are neglected. Therefore, it is necessary to develop an approach that is applicable when the adherent layers deform plastically during delamination. It well understood from the literature [34–39] that interface toughness varies with mode mixity. Hence, the approach should be capable of characterizing mixed mode loading behavior of the interface. Depending on the particular interface system the delamination mechanism can vary from a brittle cleavage type of fracture [40] to a more ductile mechanism like crack bridging [41] or fibrillation [42]. In order to understand these details of the delamination mechanism (which is important for accurate modeling of these interfaces) *in-situ* microscopic visualization of the delamination pro-



cess during the experiment is needed. Structures comprising high interface density sometimes fail by crack branching [43] and multiple cracking [44] at several interfaces. During this phenomenon some interfaces undergo unloading while others are loaded to fracture. Therefore, the experimental approach should allow for characterization of delamination behavior during loading as well as unloading of the interface. Finally, the approach should include a numerical interface model that can accurately predict interface delamination. There are several models presented in the literature to predict delamination, see for example references [45–60] (although it is noted that this not a complete list). Most of them are either fracture mechanics or cohesive zone based models. In order to predict such a complex behavior of the interface, a numerical model is needed that can simulate the mixed mode delamination behavior (with a coupling between different modes) incorporating not only loading but also irreversible unloading behavior resulting from damage and/or plasticity at the interface with a minimum number of model parameters that can be identified from the experiment.

## 1.4 Strategy

Therefore, the following strategy is applied to successfully achieve the goals of this project:

- Develop a generic experimental setup
  - that applies mixed mode loads to access the full range of mode mixities and uses only one specimen configuration for all loading modes,
  - allows for an unloading-reloading test with stable crack growth and
  - simultaneously enables *in-situ* visualization for real time fracture analysis of the interface and to obtain the parameters characterizing the fracture process zone. The goal is to obtain as much microscopic information as possible from the experiment.
- Develop an approach that allows for determination of interface parameters in the presence of plasticity at the interface and at the adherent (bulk) layers.
- Finally, develop a model that is capable of simulating delamination initiation and propagation with
  - mixed mode loading-unloading conditions along with a coupling between different modes and
  - has few parameters which can be characterized with the developed setup.

Consequently, provide a methodology for parameter identification from delamination experiments.

## 1.5 Outline of the thesis

The experimental-numerical tools developed in this thesis for characterization of interface delamination are described in detail in the following chapters. Note that each chapter is written in a journal publication format such that it can be read separately.

In Chapter 2, a new miniature mixed mode bending (MMMB) delamination setup, which enables *in-situ* characterization of interface delamination in miniature multi-layer structures, is designed and realized. The performance of the setup is assessed using specially-designed test samples and by finite element analyses. The measurement concept is validated by testing homogeneous bilayer samples with a glue interface system over the full range of mode mixities.

In Chapter 3, an improved MMMB setup is presented, which overcomes the main limitations of the original design. It is demonstrated that the improved design (i) can access a significantly larger range of interface systems due to its increased limits of maximum accessible load and stroke in all mode mixities, (ii) has significantly higher accuracy in load-displacement measurement due to its reduced clearance at the connectors, and (iii) has a high reproducibility due to a newly added setup alignment tool.

In Chapter 4, a new combined plasticity-damage interface unloading model that allows for both interface damage and/or interface plasticity is presented and a procedure for identification of all the model parameters from the *in-situ* mixed mode delaminating experiments is described.

In Chapter 5, a semi-analytical approach to separate the contribution of structural plastic dissipation to the total energy spent during a mode I delamination experiment is presented. Numerical verification of the approach and the underlying assumptions is performed. The experimental procedure for characterization is applied to CuLF-MCE samples for which the structural plastic contributions are separated in order to identify the correct interface toughness.

In Chapter 6, the experimental tools developed in this thesis are employed for the characterization of delamination in two types of industrially relevant CuLF-MCE interface samples. A comparative study of differences in the load-displacement responses, CZ traction separation laws, CERR versus mode angle trends and the observed delamination mechanisms is presented.

Finally, in Chapter 7, the main conclusions are summarized and recommendations for future work are given.



## CHAPTER TWO

# ***In-situ* characterization of interface delamination by a new miniature mixed mode bending setup<sup>1</sup>**

---

### **Abstract**

A new miniature mixed mode bending (MMMB) setup for *in-situ* characterization of interface delamination in miniature multi-layer structures was designed and realized. This setup consists of a novel test configuration to accomplish the full range of mode mixities and was specially designed with sufficiently small dimensions to fit in the chamber of a scanning electron microscope (SEM) or under an optical microscope for detailed real-time fracture analysis during delamination. Special care was taken to minimize the effects of friction, the influence of gravity, and non-linearities due to the geometry of the setup. The performance of the setup was assessed using specially-designed test samples supported by finite element analyses. Delamination experiments conducted on homogeneous bilayer samples in mode I and mixed mode loading were visualized with a scanning electron microscope and showed the formation of small micro cracks ahead of the crack tip followed by crack bridging and a full crack, thereby demonstrating the advantages of *in-situ* testing to reveal the microscopic delamination mechanism.

---

<sup>1</sup>*Reproduced from:* M. Kolluri, M.H.L. Thissen, J.P.M. Hoefnagels, J.A.W. van Dommelen, M.G.D. Geers, *In-situ* characterization of interface delamination by a new miniature mixed mode bending setup, *International Journal of Fracture*, 158, 183-195 (2009).

## 2.1 Introduction

The demand for the continuous miniaturization and multi-functionality of electronic devices led the electronic industry towards new packaging technologies like "System in Package" (SiP). SiP technology primarily involves assembly of several components (active components, passive components and MEMS) into a single package to achieve different functionalities. Consequently, SiP-microsystems contain several interfaces formed between stacked, multiple, thin layers, manufactured using different materials and processes. Interfaces are often recognized as critical regions for the reliability of these products because the presence of high stresses at these interfaces (e.g. due to a mismatch in coefficient of thermal expansion (CTE) and Poisson's ratio) and in-plane shear stresses often lead to delamination [35, 61–63]. Much research is ongoing to improve the interface behavior by adopting suitable coatings or cleaning techniques at the interface during manufacturing of these components [2]. However, detailed quantitative characterization of the interfaces in these systems is required in order to improve design rules for manufacturing and improve reliability during service of these products.

A number of experimental techniques have been developed and reported in the literature [e.g. 11, 13–20] to measure interfacial properties, most of which use a fracture mechanics approach because of its proven versatility. A fracture mechanics approach requires an experimental setup capable of triggering delamination and uses the resulting force-displacement data to obtain the interface fracture toughness or critical energy release rate (CERR) as an important interface parameter to characterize the interface. It has been shown by many authors [e.g. 34–39] that the CERR for crack propagation varies significantly with mode mixity. Furthermore, the presence of dissimilar materials forming the interface, which is common in microsystems, increases the complexity of the CERR measurement. This indicates that the experimental technique to characterize an interface system should be able to measure the CERR over the entire range of mode mixities, in order to identify valid input parameters in a design limit criterion. Techniques reported in the literature to measure the CERR include the well-known double cantilever beam (DCB) test for pure mode-I loading (ASTM D 5528-01, 2001 [64]) and end notch flexure (ENF) test for applying pure mode-II loading [65], as well as mixed mode bending (MMB) setups [e.g. 21–25, 66], which cover a range of mode mixities, see Fig. 2.1. Of all setups, only the MMB setups yield the CERR over a full range of mode mixities with a single test configuration.

The prime difficulty in many of the existing delamination experiments is the identification of the crack tip location in order to trace the crack length, which is needed to calculate the fracture toughness. To circumvent this problem, critical loads deduced from experiments, where the delamination starts for a given pre-crack length, were used to calculate the CERR with the aid of analytical formulae [22, 67, 68]. Stiffness lines generated with finite element (FE) models of known crack length specimens were used to evaluate the CERR by [25]. Some authors [e.g. 26, 69] reported that a crack length measurement with a simple optical magnification lens system may

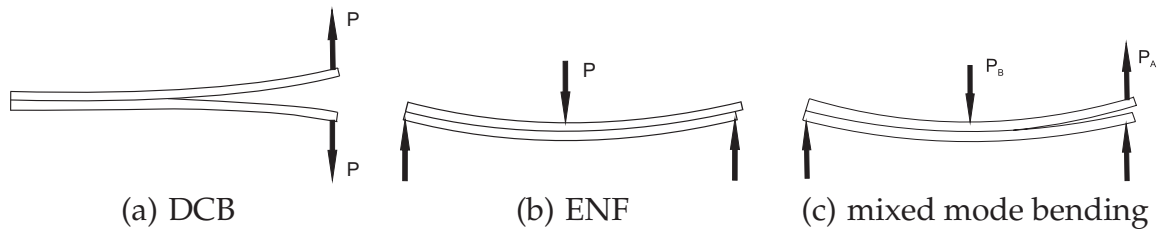


**Figure 2.1:** Sketch of different loading configurations for interface delamination

be erroneous and also highlighted the need for techniques which can measure crack lengths more accurately. Furthermore, detailed *in-situ* visualization of the delamination process is essential to accurately pin-point the crack tip location, to measure quantitative delamination characteristics such as the crack opening profile and the process zone size, and to obtain more insight in the fracture events along the interface. Experimental setups are presented in the literature, e.g. [66], that apply pure bending moments to trigger delamination which does not require crack length values to determine the CERR by using a fracture mechanics approach. However, for the detailed identification of fracture mechanisms *in-situ* visualization of the delamination front is still required.

*In-situ* characterization in a microscope, however, puts serious constraints on the overall size of the delamination setup. Evaluation of existing MMB setups elucidates the difficulties to use them for *in-situ* testing. In case of the setup of [21], shown in Fig. 2.2a, restricted dimensions of the design space prevent the lever from having sufficient length to cover the complete range of mode mixities. Furthermore, this test is difficult to perform in the horizontal plane (i.e. keeping the direction of load application in the horizontal plane), which is necessary to enable the use of standard microscopes to trace the crack tip movement during *in-situ* delamination testing (the viewing axis of a scanning electron microscope is always in the vertical direction). Merrill and Ho's setup [23], shown in Fig. 2.2b, was also constructed such that the loading direction is vertical, leading to similar limitations. Furthermore, gravity acts on both of the above mentioned setups, resulting in additional undesired forces on the sample. In the setup of [25], a counter balance was added to the loading configuration of [21] to minimize the influence of gravity. However, a persistent consequence of gravity is a strong dependence of the mode angle on the crack length. Sørensen et al. [66] presented a setup that applies pure bending moments to trigger delamination and is also designed to work in a vertical plane. The wires and springs used in this setup (to apply the required bending moments) can make it more difficult for the setup to miniaturize and modify it to be used in the horizontal plane. Later, Sørensen et al. [70] developed another setup, which applies a combination of an axial load and bending moment to achieve mixed mode loading, to study the micro-mechanics of mixed mode crack bridging in fibre composites in a scanning electron microscope (SEM). The authors reported, however that the mode angle in that setup is very sensitive to the sample deflection that occurs during the delamination and hence accurate control of the mode angle is difficult. Finally, all currently available

methods are hampered by frictional non-linearities in hinges that are attached to the sample and rotation points/joints in the loading frame. The detrimental influence of non-linearities increases when the setup and the sample are miniaturized to allow *in-situ* SEM operation.

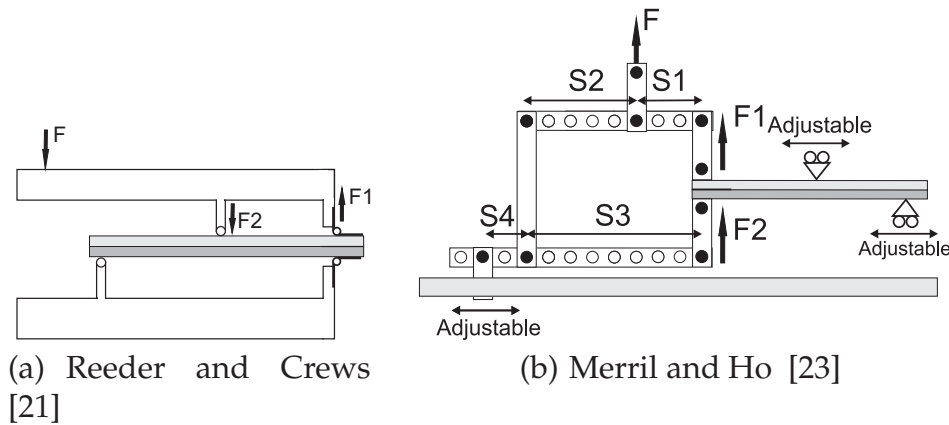


**Figure 2.2:** Two different existing concepts for mixed mode delamination testing

The present work focuses on the design and realization of a miniaturized mixed mode bending setup which enables *in-situ* delamination testing for the full range of mode mixities. This setup is designed such that effects of friction, gravity, and geometrical non-linearities are minimized. The performance of the setup is assessed using specially-designed test samples supported by FE analyses. *In-situ* delamination experiments performed on homogeneous bilayer samples are presented to prove the functionality of the setup and illustrate its capabilities for interfacial characterization.

## 2.2 Design of the miniaturized mixed mode bending (MMMB) apparatus

### 2.2.1 New configuration for mixed mode loading

A key constraint in the design of the new setup is its size, which should be small enough (i) to handle multi-layer structures that are representative for stacked layers present in SiPs and (ii) to be mounted in a commercially available micro tensile stage (Kammrath & Weiss GmbH, with an available design space of 55 x 47 x 29 mm) which in turn fits in the chamber of a SEM for *in-situ* delamination testing. Simple down scaling of existing MMB setups is not feasible because of the incompatible load frame configuration and the sample orientation that prevents *in-situ* microscopic observation. Therefore, a new test configuration was developed that meets the above men-

tioned requirements and realizes the MMB loading as shown in Fig. 2.1c. The MMB configuration is preferred because it is standardized (ASTM D6671-01, 2001, [71]) and generally accepted for characterization of interfacial delamination. A schematic representation of the new loading geometry of the MMMB apparatus is depicted in Fig. 2.3.

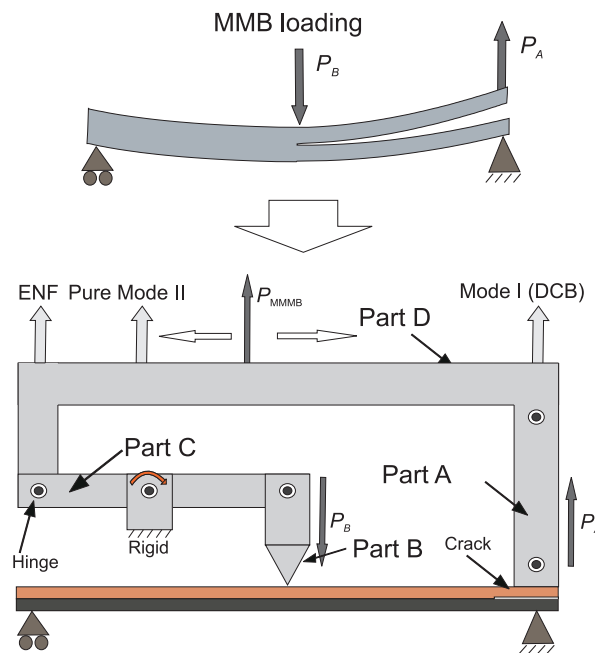


**Figure 2.3:** Schematic representation of the new loading geometry for mixed mode bending

The setup consists of four rigid parts (A to D in Fig. 2.3) connected with hinges. Advantages of the present design are: (i) its loading mechanism that allows to access the maximum range of interfacial loading modes, from double cantilever bending (pure mode I delamination), to pure mode II delamination, to end notch flexure in a single setup; (ii) its compact geometry (allowing it to be used in the chamber of an electron microscope); (iii) the insensitivity of its force measurements to its self weight, because the loading of the sample is done in the horizontal plane.

The mixed mode bending loads are applied by a new lever mechanism. Part 'C' is pinned to the outside world allowing it only to rotate in the testing plane. By the application of a force  $P_{MMMB}$  in a certain position on part 'D', part 'B' moves downward while part 'A' moves upward, generating two oppositely directed forces  $P_A$  and  $P_B$  on the sample. The ratio of the forces  $P_A$  and  $P_B$  depends on the position of the loading point on part 'D', triggering different loading modes as discussed in more detail below.

An analysis of the loads applied to the sample in the new test setup shows that the



loads transferred to the sample, which are depicted in the left hand side of Fig. 2.4, can be written as:

$$P_A = P_{\text{MMMB}}(1 - \xi) \quad (2.1a)$$

$$P_B = P_{\text{MMMB}} \frac{\alpha}{\beta} \xi \quad (2.1b)$$

$$P_C = \frac{P_B}{2} \quad (2.1c)$$

$$P_D = -P_A + \frac{P_B}{2}, \quad (2.1d)$$

where,  $\xi = \frac{H}{\gamma}$  is a dimensionless shape parameter which represents the relative position of the applied load,  $H$  is the corresponding absolute position and  $\alpha, \beta, \gamma$  are the characteristic dimensions of the loading mechanism. Finally,  $P_{\text{MMMB}}$  is the actual value of the applied mixed mode bending load. The load on the sample can be

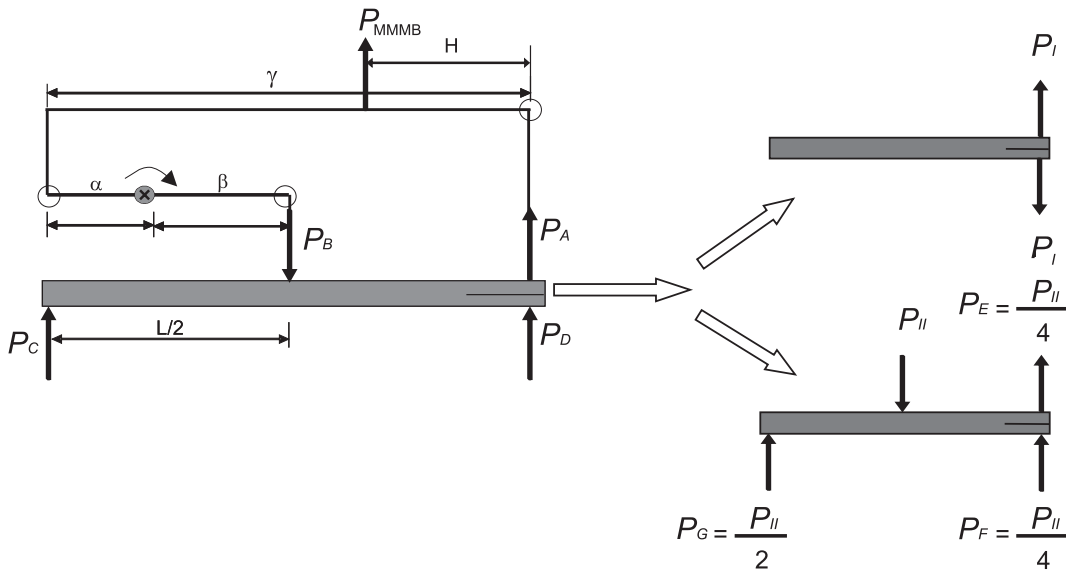


**Figure 2.4:** Schematic representation of the load distribution in mixed mode bending with the loads on the sample (left) and the decomposition of these loads into pure mode I and pure mode II components (right).

decomposed in its mode I and pure mode II components,  $P_I$  and  $P_{II}$ , respectively, which are defined by the load configurations depicted in the top and bottom right hand side of Fig. 2.4. It is noted that the loading configuration of the ENF test shown in Fig. 2.1(b) is different from a pure mode II configuration. Here, pure mode II loading is defined such that the two loads  $P_E$  and  $P_F$  acting on the end of the top and bottom arms of the specimen in the pre-cracked region (see bottom right of Fig. 2.4) are equal in order to avoid any compressive stress between two sample arms. Then,

the corresponding expressions for the mode I and mode II components are:

$$P_I = \frac{P_A + P_D}{2} = P_{\text{MMMB}} \left( 1 - \xi - \frac{\alpha}{4\beta} \xi \right) \quad (2.2)$$

$$P_{II} = P_B = P_{\text{MMMB}} \frac{\alpha}{\beta} \xi. \quad (2.3)$$

It is clear from the above analysis that when the load is applied at the right hand side of the upper lever (part 'D'), i.e. when  $\xi = 0$ , the applied loading corresponds to pure mode I loading:

$$P_I = P_A = P_{\text{MMMB}} \quad \text{and} \quad P_{II} = 0. \quad \text{for } \xi = 0. \quad (2.4)$$

In the other extreme, when the load is applied at the left end side of the upper lever (part 'D'), i.e. when  $\xi = 1$ , the applied load resembles conventional ENF loading (Fig. 2.1(b)), i.e.

$$P_{II} = P_B, \quad \text{but} \quad P_I = -P_{\text{MMMB}} \frac{\alpha}{4\beta}. \quad \text{for } \xi = 1. \quad (2.5)$$

Since in this case  $P_I \neq 0$ , this ENF test can be considered as a combined mode II and compressive mode I test. This compressive stress may cause (excessive) friction between the two sample arms. Therefore, the End Notch Flexure (ENF) case, which is frequently used for mode II fracture analysis, does not represent a pure mode II test. The resulting (excessive) friction leads to an overestimation of the interface toughness in the experiments. Several studies [72–74] also highlighted this problem due to friction when the ENF test is used to determine the mode II delamination resistance. However, a position for which the mode I component is zero and consequently a pure mode II loading is obtained can be identified in the new loading geometry. This position is given by:

$$\xi = \frac{4\beta}{\alpha + 4\beta}. \quad (2.6)$$

## 2.2.2 Design of the test apparatus

The new configuration, shown in the previous section, consists of a mechanism with several moving parts and hinges. The use of conventional hinges commonly introduces hysteresis in the force measurements because of the non-negligible frictional dissipation during rotation at these hinges, particularly in a miniaturized setup. To avoid this hysteresis in the test apparatus, specially designed elastic hinges were used. Fig. 2.5 shows an FE model of the elastic hinge used in the present setup in a deformed state. Parameters defining the geometry are also shown in the figure, as well as a safety element that is used to limit the rotation angle  $\phi$  of the hinge to the maximum achievable rotation,  $\phi_m$ , to prevent permanent deformations in the central bridge of the hinge.  $\phi_m$  is determined by the material properties, for a given geom-

etry of the hinge. A Ti-6Al-4V alloy was used for the current setup because of its favorable combination of yield strength and Young's modulus. Further details about the design of such elastic hinges can be found in [75]. In total, the setup contains 8 elastic hinges, each with dimensions of  $r = 2.5$  mm,  $h = 50$   $\mu$ m,  $g = 0.3$  mm and  $t = 2$  mm and a maximum rotation  $\phi = 5.2^\circ$ , allowing for an axial load of 20 N, which was verified through FE simulations.

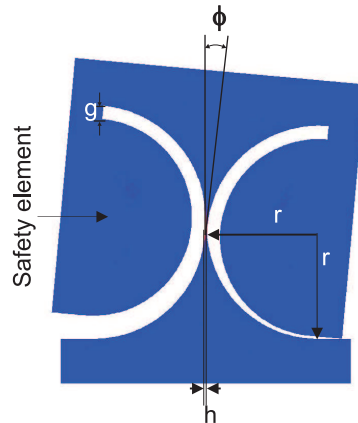


**Figure 2.5:** Finite element model of the elastic hinge used in the current setup in a deformed state. Parameters defining the geometry ( $r$ : radius,  $h$ : width of the bridge and  $g$ : width of the safety groove) are also shown.

The main parts of the device are depicted in Fig. 2.6. The 'Main Loading Mechanism', MLM, is connected to the 'Position bar' with the so called 'Mode selector'. To change the applied mode angle, the Mode selector can be placed at various discrete positions on the MLM using dovetail connectors. The arrow on the 'position bar' indicates the fixed direction and position of the externally applied force. Two 'dovetail connectors' attached on both sides of the sample are used to attach the sample to the MLM and the support hinge. The support hinge connects the sample to the real world leaving only one rotational degree of freedom. Figure 2.7 shows a picture of the whole setup placed inside a micro tensile stage. The range of sample dimensions which can fit in the MMMB device are (length  $\times$  width  $\times$  height) :  $35 \times 1-7.5 \times 0.5-6$  mm. Other elements in the setup design include (i) an adjustment mechanism to adapt the setup to a certain sample height (part 9 and 11 in Fig. 2.7), (ii) a screw mechanism (part 10 in Fig. 2.7) to adjust the alignment of the sample, and (iii) different details to overcome out-of-plane deflections in the device and to avoid friction between the moving parts and the rigid bottom plate. The latter is achieved by two flexible pins positioned in vertical direction, which support the system and increase its stability.

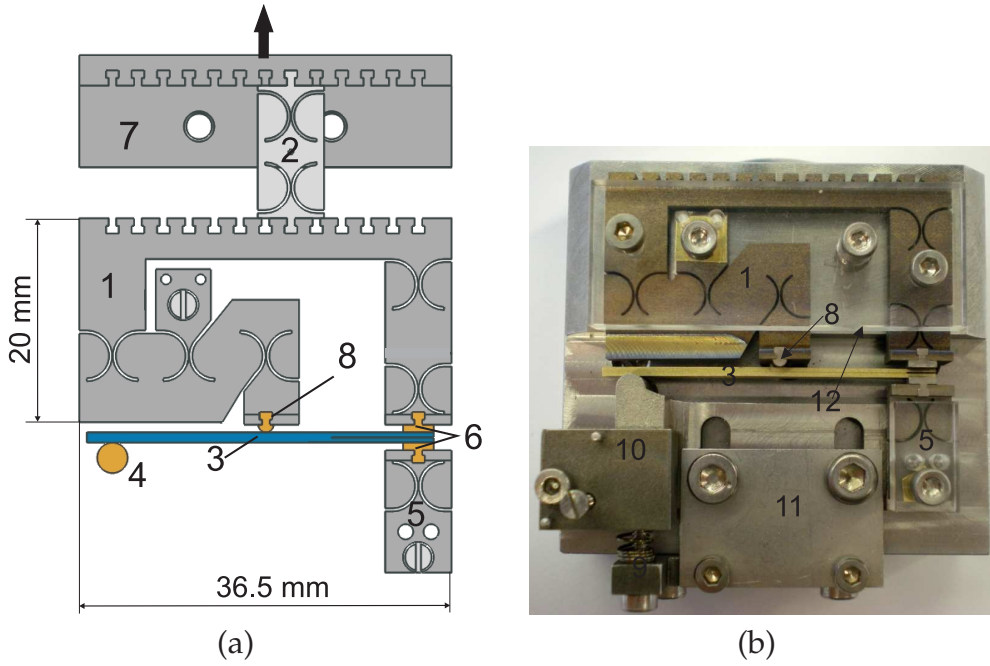


**Figure 2.6:** (a) Design of the new MMMB device and (b) picture of the real device: 1: Main Loading Mechanism (MLM), 2: Mode selector, 3: Sample, 4: Support, 5: Support hinge, 6: Dovetail connector, 7: Position bar, 8: Loading tip, 9: Setscrew for sample height, 10: Setscrew for alignment, 11: Sample height adjuster, 12: Protective plate.

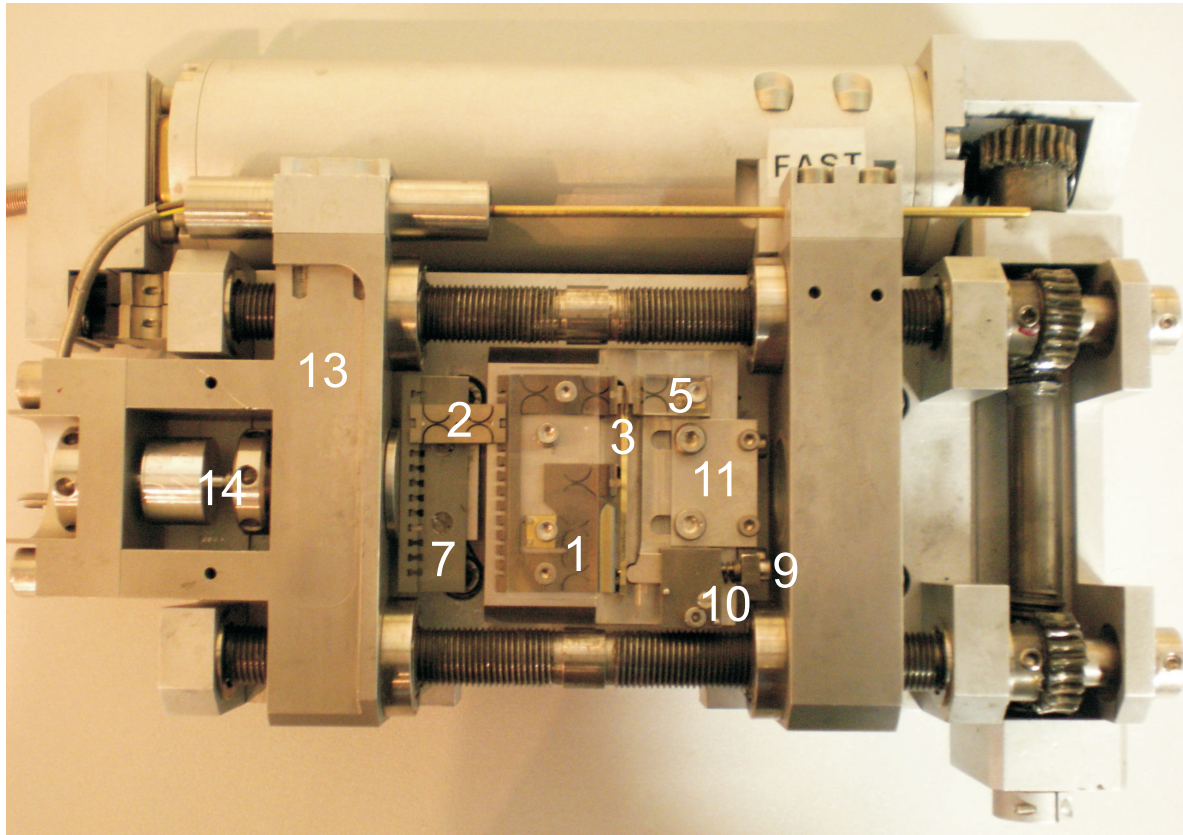
### 2.2.3 Finite element analysis

The MMMB setup with a mounted homogeneous bilayer sample has been modeled in a finite element program (MSC.Marc/Mentat), see Fig. 2.8. In total, the sample is described with 32,856 eight-node quadrilateral elements and the MLM is modeled with 52,196 four-node quadrilateral elements. A predefined crack was present in the bilayer sample, with a special crack tip mesh which has a rosette shape with transition elements and quarter-point elements. Frictionless contact conditions were used between the two surfaces of the cracked region of the specimen. The material properties used for the sample and the MLM are given in Table 2.1. Simulations were performed by assuming plane strain conditions and linear elastic material behavior.

To assess the behavior of the setup over a complete range of mode mixities, simulations were performed by applying the load ( $P_{\text{MMMB}}$ ) at different load application positions ( $\xi$  ranging from 0 to 1) for a specimen with various fixed crack lengths. Mode angles,  $\psi$ , were calculated from the stress profiles ahead of the crack tip using,

$$\psi = \arctan \left( \frac{\sigma_{12}}{\sigma_{22}} \right)_{\delta}, \quad (2.7)$$

where  $\sigma_{22}$  is the normal stress,  $\sigma_{12}$  is the shear stress and  $\delta$  is a characteristic distance from the crack tip along the interface. This distance needs to be tuned in case of

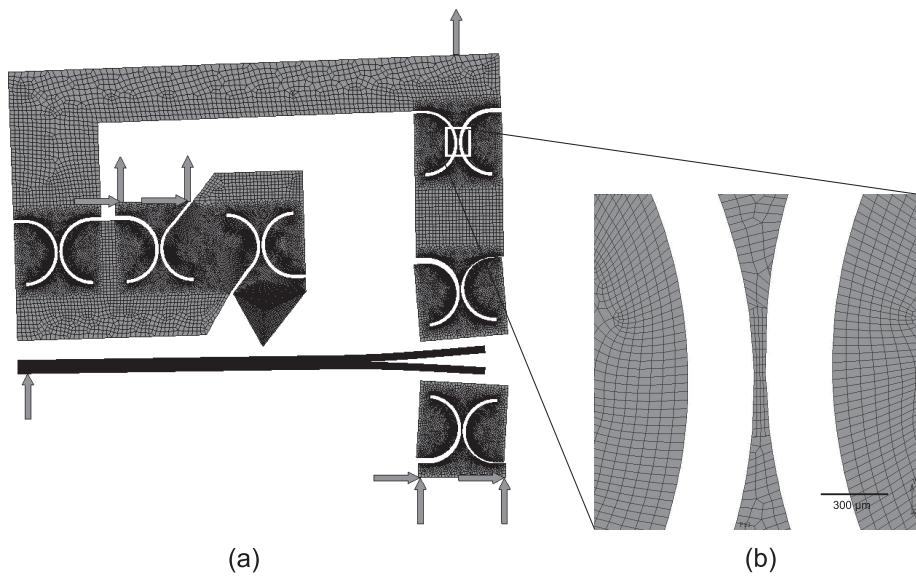


**Figure 2.7:** MMMB device, mounted in a micro tensile stage, with: 1: Main Loading Mechanism (MLM), 2: Mode selector, 3: Sample, 5: Support hinge, 7: Position bar, 9: Setscrew for sample height, 10: Setscrew for alignment, 11: Sample height adjuster, 13: Micro tensile stage, 14: Load cell.

interfaces between dissimilar materials [77], because of the existence of a complex stress state at those interfaces. In case of homogeneous bilayer samples,  $\delta$  can be any arbitrary value away from the plastic zone at the crack tip, and therefore  $\delta = 50 \mu\text{m}$  was chosen in the present analysis [35, 61, 77]. The mode angles, calculated from the simulation results of a specimen with a 6 mm pre-crack length at  $400 \mu\text{m}$  displacement applied to the main loading mechanism (MLM displacement), are shown as a function of loading position  $\xi$  in Fig. 2.9a. This figure shows that the new MMMB setup permits to access the complete range of mode mixities from  $0^\circ$  to  $90^\circ$  mode angle by changing the loading position  $\xi$  from 0 to 0.8, respectively. The mode angle is about  $90^\circ$  for all positions in the range  $\xi = 0.8 - 1$ . As shown in the previous section, pure mode II loading is obtained with a loading position  $\xi = \frac{4\beta}{\alpha+4\beta}$ , which, in the present setup, equals  $\xi = 0.8$ . When the load is applied at positions  $\xi \geq 0.8$ , an additional compressive mode I component exists (Eq. 2.2) in addition to the pure mode II component acting at the crack tip. The presence of a compressive mode I component acting on the extremity of the specimen does not significantly influence the mode angle obtained from the stress field ahead of the crack tip. Note, however,

**Table 2.1:** Material properties of loading mechanism and sample.

	Brass (sample) <sup>a</sup>	Ti-6Al-4V (MLM) <sup>b</sup>
Young's modulus (GPa)	112	113.8
Poisson's ratio	0.346	0.342
Yield stress (MPa)	204	880

<sup>a</sup>Determined from uni-axial tensile experiments<sup>b</sup>[76]**Figure 2.8:** (a) FE model of the setup and sample with boundary conditions and (b) Magnified view of an elastic hinge (indicated with a rectangle in (a)).

that delamination experiments performed at those positions are not completely representative for pure mode II conditions, since the friction induced at the fractured interface may influence the delamination behavior. This also applies to conventional ENF tests, which are widely used as a mode II delamination test. Implications of these differences are discussed in the results and discussion section.

The FE model was also used to evaluate the influence of the applied MLM displacement and the crack length on the mode angle. In Fig. 2.9b, the mode angle is shown as a function of MLM displacement for three different loading positions for a specimen with a 6 mm long pre-crack. It can be observed that the mode angle stays almost constant with a maximum difference of  $4^\circ$  between the minimum and maximum values of the three considered load cases for position  $\xi = 0.75$ . Figure 2.9c shows the mode angle as a function of the crack length for the same three loading positions at  $400 \mu\text{m}$  displacement. The mode angle stays nearly constant for different crack lengths with a maximum difference of  $2^\circ$  between the extreme values for position

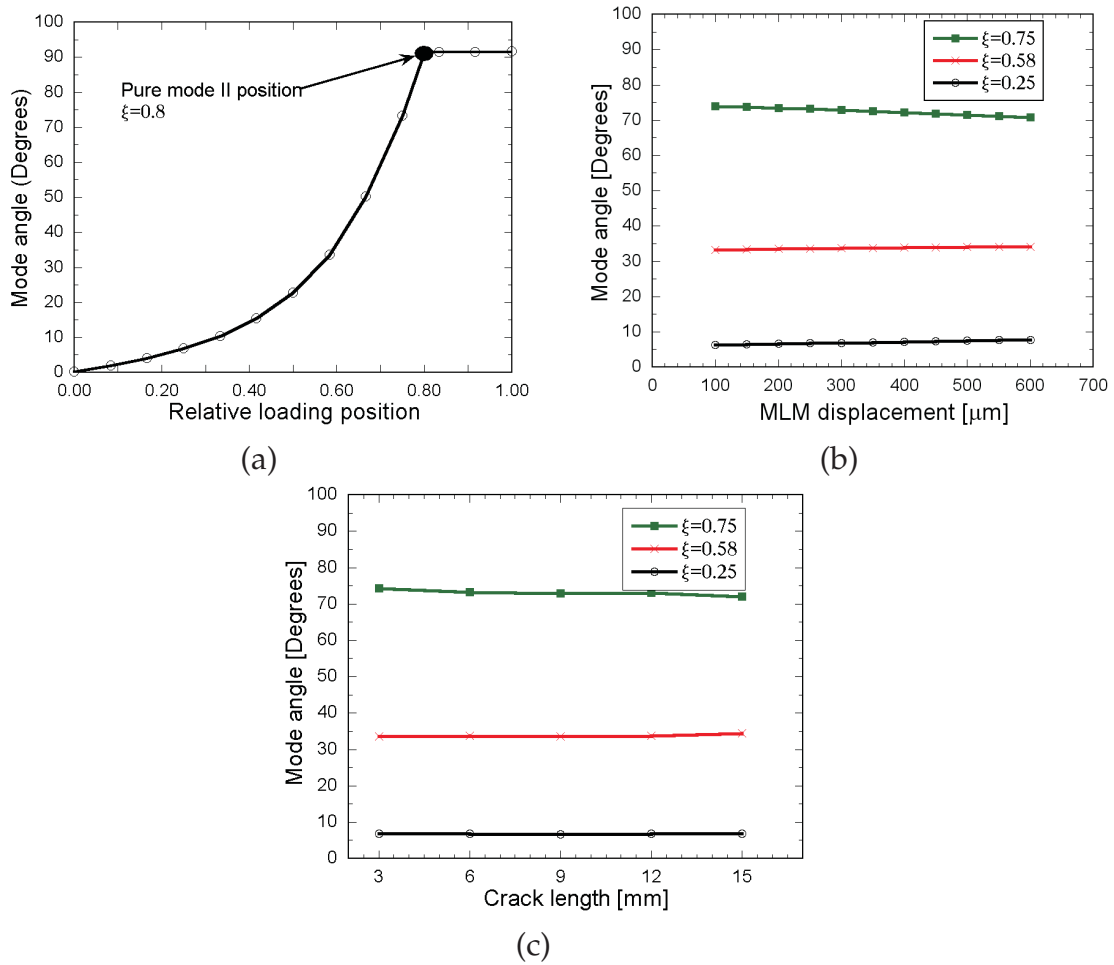


**Figure 2.9:** Mode angle obtained by FEM analysis as a function of (a) relative loading position ( $\xi$ ) for a crack length of 6 mm at 400  $\mu\text{m}$  MLM displacement, (b) displacement applied to the MLM for three loading positions for a 6 mm crack length specimen, and (c) crack length for three loading positions at 400  $\mu\text{m}$  MLM displacement. A bilayer sample of 35 mm length, 5 mm width and 0.5 mm thickness for each layer is modeled with material parameters of brass as given in Table 2.1.

$\xi = 0.75$ . This is also in agreement with the analysis reported in [78], where it is noted that the change in mode angle with increasing crack length is negligible for symmetric homogeneous bilayer samples. In case of bilayer samples with different materials and thicknesses, the mode angle stays (nearly) constant when the ratio of crack length to the layer thickness is at least 6. For the present case this ratio is larger than 12. These simulations confirm that the new MMMB setup provides access to the complete range of mode angles whereby the mode angle does not change significantly with the applied displacement and/or evolving crack length.

## 2.3 Validation

The performance of the MMMB device is assessed in order to determine the influence of potential inaccuracies that may result from the geometry, machine compliance, or other possible factors like clearance at connectors. Specially designed test samples (shown in Fig. 2.10) have been used to this purpose. These are homogeneous, single layer brass samples (i.e. without an interface and no propagating crack), with a well defined notch, having an opening width of  $30\ \mu\text{m}$ , representing an existing crack of a fixed length. The thickness of these samples is 1 mm. Figure 2.10 shows end portions of two different types of these test samples. The specimen shown in Fig. 2.10a is designed for mode I and mixed mode loading, and the specimen shown in Fig. 2.10b is designed for mode II loading with a vertical elastic beam at the end of the notch (see fig. 2.10c). This special design is used in order to prevent contact between two arms of the notched portion in mode II tests ( $\xi = 0.8 - 1$ ) where compressive mode I component is present.

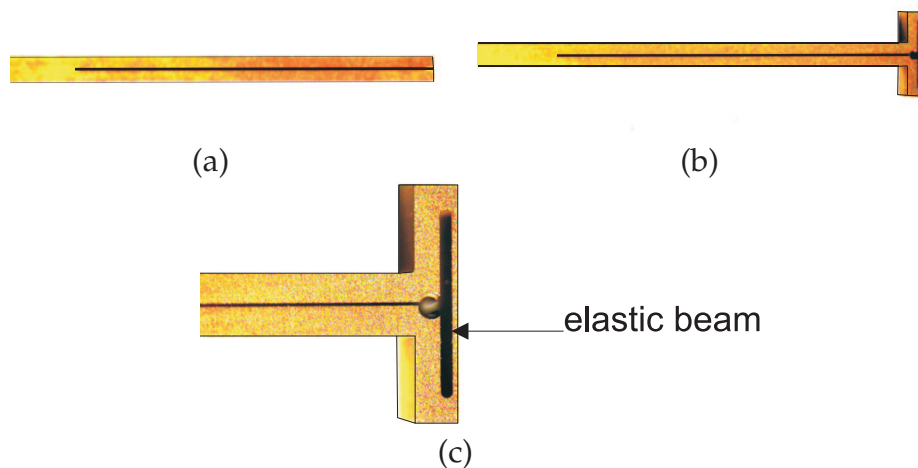


**Figure 2.10:** End parts of (a) mode I/ mixed mode test sample and (b) mode II test sample. (c) Detailed image of the elastic beam of the mode II test sample. All the samples are made of brass (see Table 2.1 for material properties) with dimensions (length x width x thickness) of 35 mm x 5 mm x 1 mm.

Test samples with 5 different notch lengths (3, 6, 9, 12 and 15 mm) were used to check the performance of the setup as a function of the notch length. Figure 2.11 shows the results of these five samples loaded at  $\xi = 0.5$ . A small amount of hysteresis was identified as the result of some clearance in the dovetail connectors. The relative hysteresis, defined as the dissipated energy during a loading-unloading cycle, relative to the energy supplied during loading was calculated for all crack lengths and different loading positions. The maximum relative hysteresis was found to be 4% with a mean value of 3% for all positions between  $\xi = 0 - 0.8$ . Comparison with digital image correlation (DIC) results confirmed that the hysteresis indeed originates



from a minor clearance in the dovetail connectors. Even though the amount of hysteresis is limited, and not considered further in this paper, this will be improved in a future new connector design.

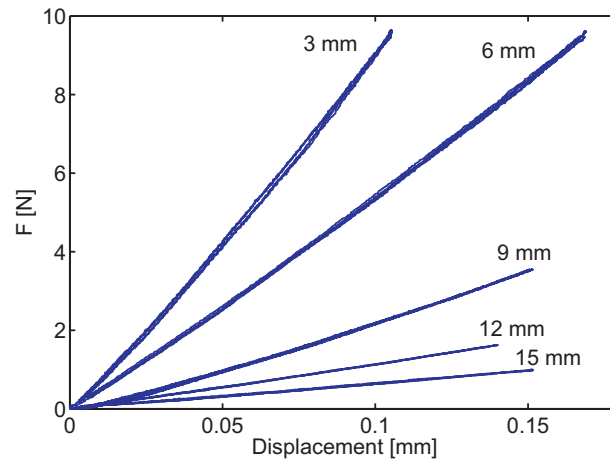


**Figure 2.11:** Load-displacement results of the test samples shown in Fig. 2.10 for loading-unloading cycles with  $\xi = 0.5$  for five crack lengths. The numbers indicate the crack length.

## 2.4 Experimental results and discussion

*In-situ* experiments with the new setup were conducted in a scanning electron microscope and under an optical stereo microscope at high magnifications. A batch of bilayer samples, consisting of two 0.3 mm thick spring steel layers glued together with an Araldite 2020 glue with a thickness of  $\sim 5 \mu\text{m}$  was used in the experiments. At the end of each sample, a pre-crack of 3 mm length was introduced with electro discharge machining. All the samples were heat treated at  $80^\circ\text{C}$  for 3 days to make the glue brittle and to fine tune the resulting glue strength. On the basis of these experiments, the interface properties of the custom made interface structure were characterized over a complete range of mode mixities, thereby demonstrating the practical functionality of the setup. Before the experiment, samples were fine polished on one side (perpendicular to the plane of the interface) to visualize the interface at high magnifications. Small markers with a regular spacing of approximately  $500 \mu\text{m}$  were introduced on the polished side with a sharp knife. These markers were used as a reference for tracking the position of the crack tip, since the crack tip moves out of the field of view of the microscope during the experiment. The dovetail connectors were attached on both sides of the samples with a strong glue at the pre-cracked end, after which the samples were carefully mounted into the setup.

Before actual loading of the specimen, each sample was loaded at position  $\xi = 0$  until the initiation of a sharp pre-crack was observed with a microscope. Finally, the position selector was reinserted at the appropriate position to carry out a delamination experiment at the desired mode angle. Actual loading was applied at a displacement rate of  $3 \mu\text{m/s}$  and load and cross-head displacement values were recorded with the built in load cell (20N) and linear variable differential transformer (LVDT) respectively. During the test, the sample was unloaded and reloaded at regular intervals. At each load reversal, images of the crack tip were recorded at a magnification of 250x. These images were used to determine the crack length corresponding to the load reversals in the post processing analysis.

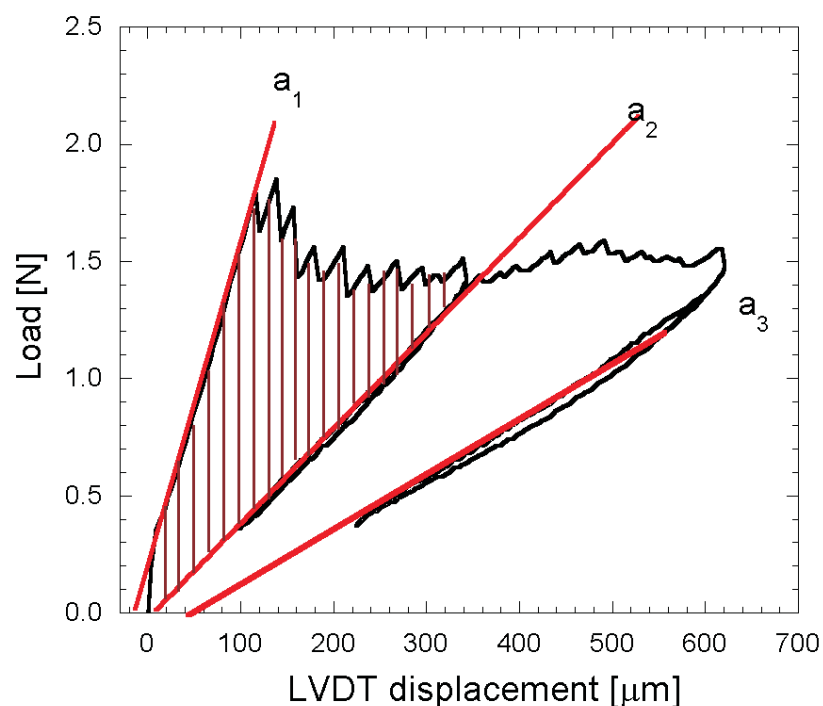


**Figure 2.12:** Load-displacement response of a bilayer steel sample (glue interface) tested at position  $\xi = 0$ . The dimensions (length  $\times$  width  $\times$  thickness/each layer) of the sample are 35 mm  $\times$  3 mm  $\times$  0.3 mm. The measured crack lengths at each load reversal are:  $a_1 = 4.40$  mm,  $a_2 = 6.25$  mm and  $a_3 = 7.86$  mm. The stiffness lines and crack lengths are used to calculate the CERR.

Figure 2.12 shows the load-displacement result of an *in-situ* experiment conducted under a stereo microscope, where the sample is loaded at position  $\xi = 0$ . Initially, at the beginning of the experiment, the load increases rapidly with the displacement until the pre-crack starts propagating further. During this stage, the load remains approximately constant with small discontinuities with increasing displacement. Through real-time optical and scanning electron microscopic visualization, it

is observed that the interface is delaminating in a discrete fashion. The observed serrated behavior is attributed to the discrete crack growth caused by non-uniformity of the adhesion strength over the interface area. This is confirmed by the microscopic observation which shows that, sometimes, the crack front jumps from one interface to the other. Apart from that, Fig. 2.12 also shows a small amount of hysteresis during each unloading-loading cycle.

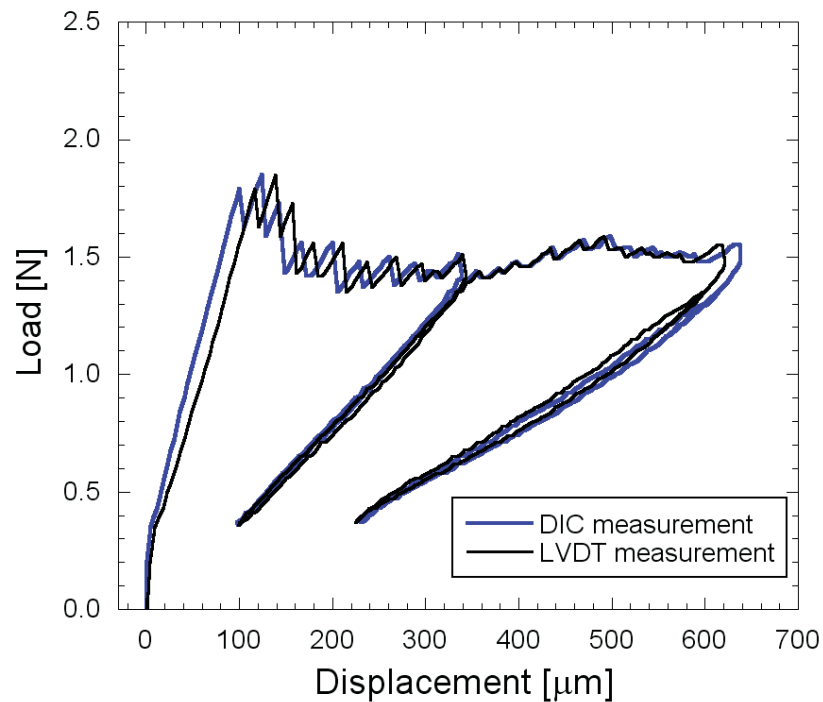


**Figure 2.13:** Comparison of the raw load-displacement curves based on LVDT and DIC displacements. Samples specifications are the same as given in Fig. 2.12.

In order to further verify that the observed (serrated and hysteresis) behavior originates from the interface and not from the setup, a separate displacement measurement is done using a digital image correlation (DIC) technique [79]. Vertical opening displacements are measured by tracking the center points of the dovetail connectors on both sides of the sample, from a series of pictures taken during the delamination test, with the image correlation software Aramis. Comparison of LVDT and DIC based displacements, shown in Fig. 2.13, reveals an adequate agreement between these two measurements. An important observation is that the DIC measurement also shows the small hysteresis observed during the unloading-loading cycle with the LVDT measurement. This indicates that the hysteresis observed originates from the interface behavior and that this effect is indeed captured by the new setup. A relatively small clearance ( $15 \mu\text{m}$ ) in the dovetail connectors explains the small deviation between both measurements, particularly in the initial portions of the curves.

From the above discussion, it can be concluded that, (i) the new MMMB setup accurately captures the behavior of the interface and (ii) small deviations are present in the measured displacement due to some of clearance in the dovetail connections, which will have only a minor influence on the measured interface toughness.

Pictures taken during the load reversals were used to determine the crack lengths at each load reversal. There can be a deviation in the crack length measured at the (visible) surface (at the side of the sample) from the crack length at the middle, e.g. in case of a curved delamination front. This deviation depends mainly on the fracture process and thus on the specific interface being tested, whereas the sub-micron resolution of the SEM images is clearly not the limiting factor. However, the applied approach of calculation of the CERR from the energy equilibrium conditions requires only an increase in crack length between two consecutive load reversals in the delamination test. Hence, for the case of constant process zone and thus constant delamination front (curvature) only the uncertainty in the measurement of increase of crack length is important. For the present case (where delamination tests performed in SEM) a value of  $\approx 2 \mu\text{m}$  was identified.

Stiffness lines were fitted to the loading curves as shown in Fig. 2.12. The critical energy release rate of the interface was calculated from the area between the successive stiffness lines (the hashed region in Fig. 2.12), divided by the delaminated area corresponding to an increase of the crack length from position  $a_1$  to  $a_2$ . The resulting CERR values are shown as a function of the mode angle, as determined from FE simulations, in Fig. 2.14. From this figure, it is clear that the CERR increases with increasing mode angle (towards position  $\xi = 1$ ). It is noted that the CERR reported in this study represents the macroscopic interfacial fracture energy, which may include significant contributions from other dissipative mechanisms like plasticity in the layers (at the immediate vicinity of the interface) and the interface itself apart from the intrinsic fracture energy. This is particularly the case when a ductile layer is present in the composite stack [80, 81]. Any plasticity contribution due to permanent deformation of the sample structure to the CERR should be removed. In the present study, sample layers are made of spring steel for the specific reason to avoid any structural plasticity. Another important observation from this figure is that a large difference exists between the CERR values measured at  $\xi = 0.83$  and at  $\xi = 1$ . The position  $\xi = 0.83$  is close to pure mode II loading, and has a negligible compressive loading at the interface, whereas for the  $\xi = 1$  position (which resembles an ENF test), a compressive load is applied at the cracked portion of the two layers. The presence of this compressive load between the cracked layers leads to frictional dissipation causing an overestimation of the CERR values [72]. This result also indicates that to measure mode II delamination CERR, one needs to apply a pure mode II loading instead of a conventional ENF loading.

*In-situ* measurements performed in the SEM allowed to (i) visualize the delamination mechanism at the interface and (ii) identify the precise crack tip location. In Fig. 2.15, an interface with the crack growing from the right, is shown. Small pre-cracks of 50 - 100  $\mu\text{m}$  appear in front of the crack tip before the actual crack evolution (Fig. 2.15a).

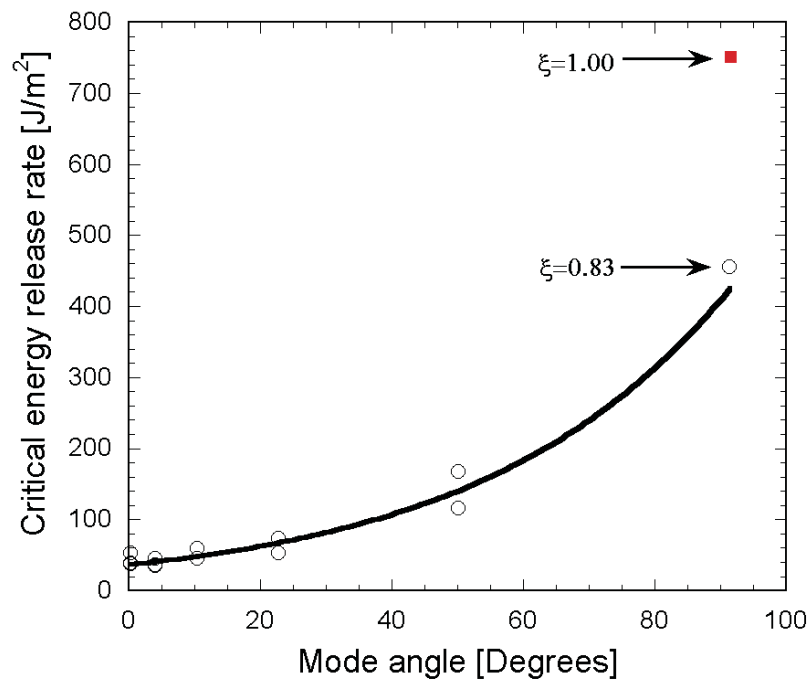


**Figure 2.14:** CERR plotted as a function of (nominal) mode angle. At 90° mode angle the CERR measured for position  $\xi = 0.83$  is much lower than for position  $\xi = 1$ . Mode angles corresponding to a given loading position  $\xi$  are obtained using LEFM simulations (see Fig. 2.9(a)).

These small pre-cracks grow and interconnect, resulting in the propagation of the main crack (Fig. 2.15b).

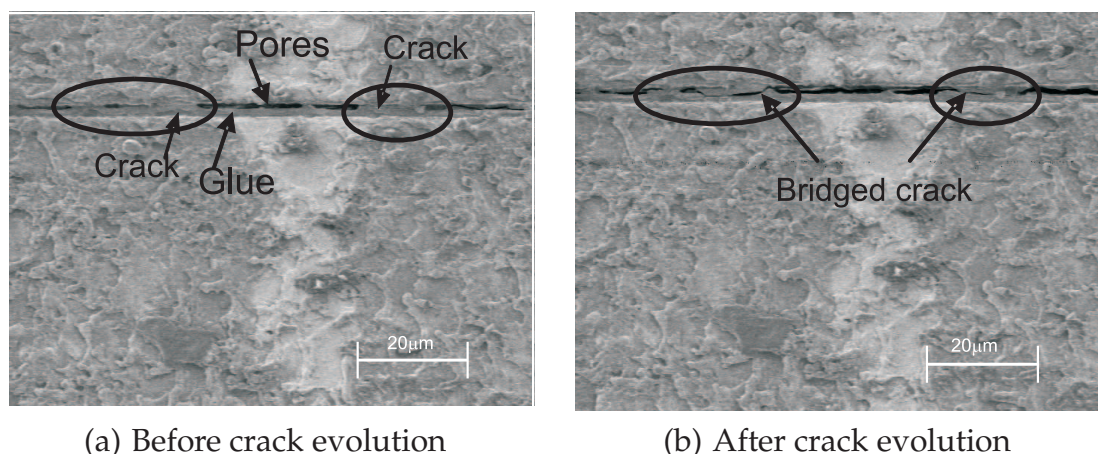


**Figure 2.15:** SEM micrographs showing the mechanism of delamination: bridging of the small cracks into a main crack

From the *in-situ* measurements, the position of the "crack tip" was determined with

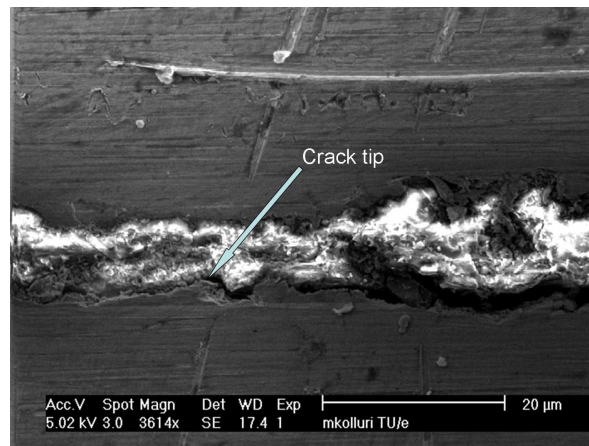


**Figure 2.16:** SEM micrograph showing the precise crack tip location

an accuracy of  $\sim 5 \mu\text{m}$ , see Fig. 2.16. In principle, this allows to extract the CERR more accurately than with conventional MMB setups. One remaining difficulty is tracking the crack tip as the delamination proceeds. This can be overcome by using special markers and interrupting the test to bring the crack tip location back into focus.

## 2.5 Conclusion

A new miniature setup capable of applying a mixed mode bending load to a bi-layer delamination sample with a pre-crack was successfully introduced. The new setup can be used for *in-situ* delamination tests in advanced microscopic systems (e.g. SEM). The setup was designed with elastic hinges to overcome hysteresis due to friction. Comparison of the load-displacement diagrams from LVDT and DIC measurements showed that the present setup can accurately capture the interface behavior. An analysis of the setup proved the capability of the new setup to achieve a full range of mode mixities, with a nearly constant mode angle as a function of the crack length and crack opening displacement. The analysis also revealed that the conventional ENF test is not a true representation of a mode II delamination. The present setup can also apply a pure mode II loading (different from ENF loading) to obtain representative CERR values. The CERR measured for an ENF test is considerably higher than for a pure mode II loading, which was attributed to frictional dissipation between the two cracked surfaces. Finally, an *in-situ* test done in a SEM showed a high-resolution observation of the delamination mechanism. In addition, these *in-situ* tests allow for a more precise determination of the location of the crack tip.



## CHAPTER THREE

# An improved miniature mixed mode delamination setup for *in-situ* microscopic interface failure analyses<sup>1</sup>

---

### Abstract

Precise characterization of interface delamination in miniature interface structures is an ongoing challenge with the advent of miniaturization and multi-functionality in the electronics industry. Accurate numerical prediction of the interface behavior is necessary to minimize delamination failures. Successful prediction requires (i) accurate determination of the interface properties like the critical energy release rate, CERR, over the full range of mode mixities and (ii) simultaneous *in-situ* microscopic visualization of the delamination mechanism. These requirements were recently addressed by the development of the miniature mixed mode bending (MMMB) setup [Kolluri et al., Int. J. Frac. 2009]. In this article an improved MMMB setup is presented, which overcomes the main limitations of the original design. Specifically, the improved design (i) can access a significantly larger range of interface systems due to its increased limits of maximum accessible load and stroke in all mode mixities, (ii) has significantly higher accuracy in load-displacement measurement due to its reduced clearance at the connectors, which is particularly relevant for miniature samples, and (iii) has a high reproducibility due to a newly added setup alignment tool. The measurement concept is validated on (industrially relevant) copper

---

<sup>1</sup>Reproduced from: M. Kolluri, J.P.M. Hoefnagels, J.A.W. van Dommelen, M.G.D. Geers, An improved miniature mixed mode delamination setup for *in-situ* microscopic interface failure analyses, *Journal of Physics D: Applied Physics*, 44, 1-13, (2011).



lead frame-molding compound epoxy (CuLF-MCE) interface structures. The load-displacement curves and corresponding CERR values obtained from experiments over the full range of mode mixities are discussed in relation to the delamination mechanism observed during real-time *in-situ* visualization. Specifically, the measured increase of the CERR towards mode II is related to a more discrete or jerky crack growth behavior observed in the mode II dominant tests. Finally, the potential of the methodology for interface parameter characterization is illustrated.

### 3.1 Introduction

Interfacial delamination is a major concern in the micro-electronics industry (see, e.g. [3, 4] and Fig. 3.1(a,b)) due to the high density integration of dissimilar materials into a single so-called 'System in Package (SiP)', driven by ever-increasing demands for miniaturization and multi-functionality. Delamination occurs mainly due to significant thermal stresses generated at these interfaces during thermal cycling, triggered by the mismatch of the coefficient of thermal expansion (CTE) and the Poisson's ratio of the adherend layers. As a prime example, during encapsulation of SiPs with molding compound epoxy (MCE), interfaces between MCE and outer layers of the SiP are often susceptible to delamination (in particular lead frame-MCE and die-MCE interfaces, shown as dashed lines in Fig. 3.1(c)). Specifically, delamination of copper lead frame (CuLF)-MCE interfaces attracted significant attention from researchers [2, 25, 82–86]. Yet the behavior of this interface over the full range of mode mixities and the underlying delamination mechanism are still not well understood. One of the reasons for this is that under certain loading configurations interface delamination occurs in concurrence with plasticity in the bulk layers, which prevents accurate determination of representative Critical Energy Release Rate (CERR) values. Accurate prediction of the interface behavior in SiP manufacturing and exploitation is necessary to minimize these delamination failures and to improve design rules accordingly. Successful prediction of interfacial failure using available interface models [58, 59, 87], is only possible with the input of accurate and detailed measurements of the interface behavior obtained from well defined delamination experiments. To this end, this article presents a new improved Miniature Mixed Mode Bending (MMMB) delamination setup capable of measuring CERR values under simultaneous *in-situ* observation under the scanning electron microscope (SEM) or optical microscope. As an illustrative example, this setup is validated on measurements of the CERR of the CuLF-MCE interface for the full range of mode mixities.

It is well documented in the literature that interface fracture toughness is not a unique material property but depends on the entire stress field ahead of the crack tip (i.e. loading mode) [22, 35, 36, 38, 77, 88, 89]. A complete description of an interface necessitates its characterization over the complete range of mode angles from mode I to mode II. Figure 3.2 shows the loading configurations typically used for testing under mode I (double cantilever beam (DCB) test, Fig. 3.2(a)) and mode II (end notch flexure (ENF) test, Fig. 3.2(b)). In contrast, Figure 3.2(c) shows the mixed mode

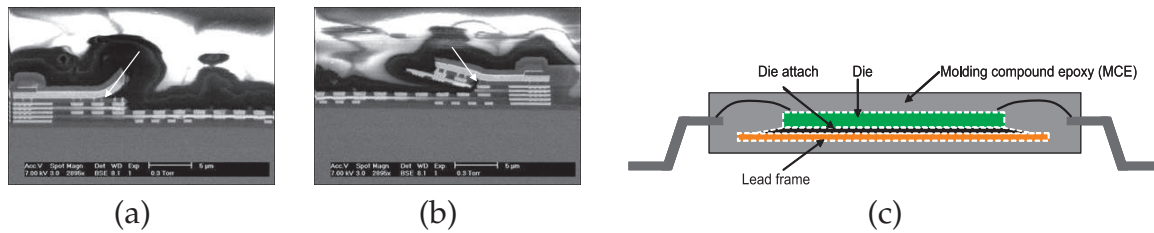


**Figure 3.1:** (a,b) SEM micrographs (arrows) showing delamination between copper metal lines and dielectric material in back end structures (Courtesy of NXP Semiconductors). (c) Schematic of the lead frame package molded in a molding compound epoxy. All the interfaces which are prone to delamination are marked as dashed lines.

bending test, which is capable of testing the full range of mode mixities. Besides controlling interface delamination under a well-defined mode angle in a single loading configuration, it is highly beneficial if the experimental methodology is able to carry out accurate *in-situ* delamination tests of miniature samples under optical and scanning electron microscopes. This enables to precisely identify the crack tip position and to understand the active delamination mechanism in addition to the CERR measurements. Due to the small forces involved with miniature samples, such a setup should not entail undesirable and non-negligible dissipative contributions due to friction and clearance in the moving parts of the setup that prohibit accurate force measurement. Furthermore, non-linearities resulting from the geometry of the setup and from the self weight of the parts of the setup should be avoided.

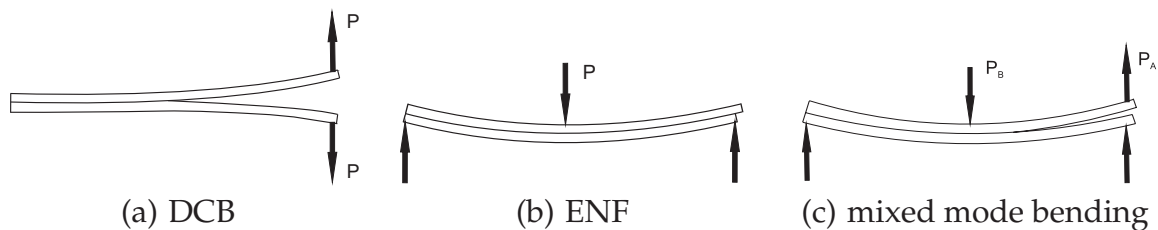


**Figure 3.2:** Sketch of different loading configurations for interface delamination; (a) double cantilever beam (DCB) test; (b) end notch flexure (ENF) test; and (c) mixed mode bending test.

A number of experimental setups, which can carry out mixed mode delamination tests [21–25, 86, 90], have been proposed in the literature. The setup of Reeder and Crews [21] is well known [22, 25, 91, 92] and can access a large range of mode mixities, however, excluding pure mode I and mode II. Hence, separate DCB tests and ENF tests are required to fulfill the interface characterization over the complete range of mode mixities [25]. Despite being suitable for mixed mode testing, none of the above mentioned setups are directly suitable for *in-situ* testing of miniature samples due to (i) their size being too large to handle miniature samples and to fit in a SEM chamber, (ii) their inability to keep the direction of load application horizontal, which

is required to enable the use of standard microscopes to trace the crack tip movement and to visualize the delamination mechanism during *in-situ* testing, and (iii) the presence of friction resulting from moving hinges and parasitic non-linearities (e.g. through the self weight of the setup acting on the sample), which is especially a problem when testing miniature samples. To overcome these constraints, a re-designed miniature mixed mode bending (MMMB) setup was recently introduced by Kolluri et al. [93].

Proof of principle measurements on glued interfaces [93] indeed demonstrated that the MMMB setup was successful in carrying out CERR measurements over the full range of mode mixities, under simultaneous *in-situ* microscopic visualization of the delamination mechanism. The remaining limitations of the setup proposed in [93] are (i) the maximum applied load (too limited) and (ii) maximum applied displacement (too small), (iii) instrumental hysteresis that required an elaborate digital image correlation procedure to correct for, and (iv) high operator skill to compensate lack of setup robustness and ease-of-use. Particularly, the first two limitations prevent testing of the industrially-relevant CuLF-MCE interfaces. This paper presents an improved miniature mixed mode bending delamination setup that overcomes the above-mentioned limitations, enabling a study on CuLF-MCE samples. First, a brief overview of the original MMMB design is given with its advantages and limitations. Next, the various improvements to the MMMB design are presented, and the design of the improved MMMB setup is confronted with the original MMMB setup. The functionality of the improved setup is demonstrated with tests on specially designed validation samples. Measurement accuracy and reproducibility are addressed by repeated tests on validation samples. Finally, the improved MMMB is used to study delamination in (preplated) CuLF-MCE samples over full range of mode mixities, and under *in-situ* SEM visualization of the delamination mechanism.

## 3.2 Brief review of the original MMMB setup

In this section, the main details of the loading configuration of the original MMMB design are reviewed [93]. The mixed mode bending loading configuration shown in figure 3.2(c) was adopted because of its ability to apply different mixed mode loading conditions and the fact that it is standardized (ASTM D6671-01, 2001, [71]), and widely accepted for interface delamination characterization. Figure 3.3 (left) shows the design of the original MMMB device to achieve the required mixed mode bending loading. The setup consists of several moving parts and special elastic hinges for frictionless rotation. The loads transferred to the sample, depicted in Fig. 3.3, can be written as:

$$P_A = P_{\text{MMMB}}(1 - \xi) \quad (3.1a)$$

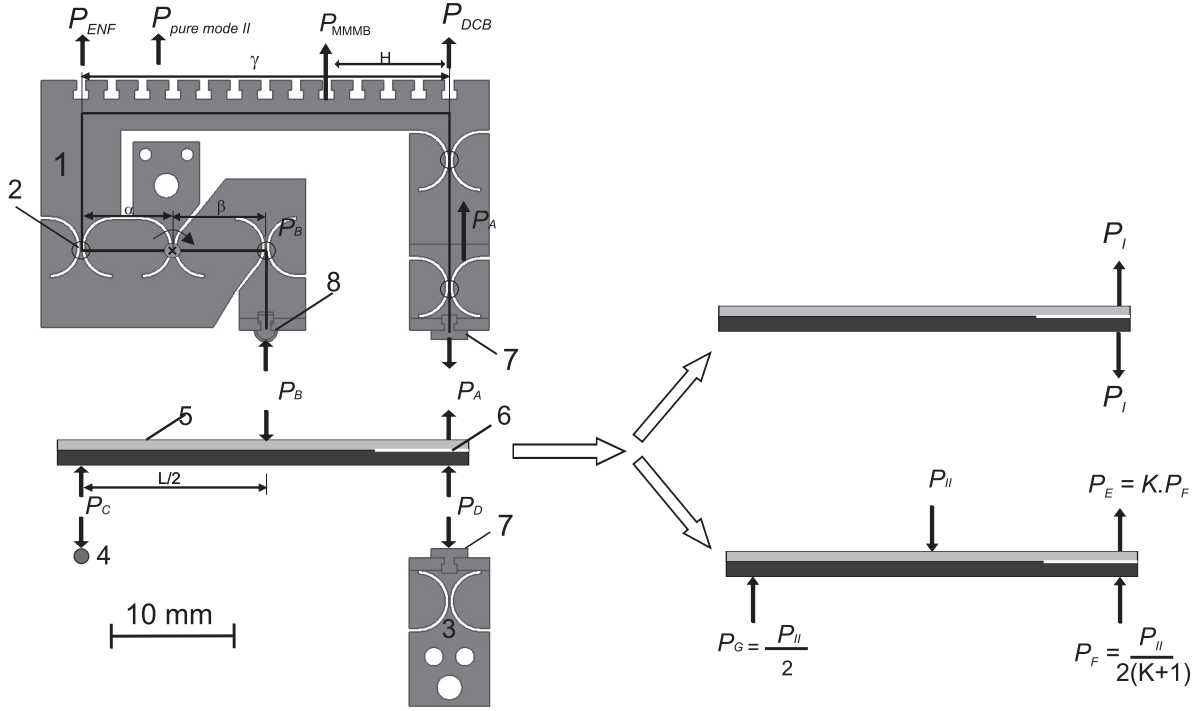


**Figure 3.3:** Design of the original MMMB device with: (1) the main loading mechanism (MLM) with (2) elastic hinges, (3) the bottom support hinge, (4) the left support, (5) the bilayer sample with (6) precrack, (7) the dovetail connector, and (8) loading tip. Also shown is the schematic representation of the load distribution under mixed mode bending, with the loads on the sample (shown on the left) and the decomposition of these loads into mode I and pure mode II components (shown on the right).

$$P_B = P_{\text{MMMB}} \frac{\alpha}{\beta} \xi \quad (3.1b)$$

$$P_C = \frac{P_B}{2} \quad (3.1c)$$

$$P_D = -P_A + \frac{P_B}{2}, \quad (3.1d)$$

where,  $\xi = \frac{H}{\gamma}$  is a dimensionless shape parameter that represents the relative position of the applied load.  $H$  is the corresponding absolute position of the applied mixed mode load  $P_{\text{MMMB}}$  and  $\alpha, \beta, \gamma$  are the characteristic dimensions of the loading mechanism (indicated in Fig. 3.3). Variation in the mode mixities is obtained by changing  $\xi$  over 13 discrete positions from 0 (DCB) to 1 (ENF).

The load on the sample can be decomposed in its pure mode I and pure mode II components,  $P_I$  and  $P_{II}$ , respectively, which are defined by the load configurations depicted in the top and bottom right hand side of figure 3.3. Pure mode II loading is defined as the case for which the separating parts of the cracked specimen

deform with the same curvature, resulting in a zero mode I component at the interface. The corresponding expressions for these mode I and mode II components in a bilayer sample with the same materials and equal layer thickness were presented previously [93]. Here, a more generalized form of these expressions for a bilayer sample with dissimilar materials and unequal layer thicknesses is presented. Details of the derivations are given in the appendix.

$$P_I = P_{\text{MMMB}} \left( 1 - \xi - \frac{K\alpha}{2\beta(1+K)}\xi \right), \quad (3.2)$$

$$P_{II} = P_{\text{MMMB}} \frac{\alpha}{\beta} \xi, \quad (3.3)$$

where  $K = \frac{P_E}{P_F}$  is a constant determined by the geometry and material properties of the two adherend dissimilar layers, which is equal to  $K = \frac{E_t I_t}{E_b I_b}$  under the assumption of linear beam theory, with  $E_i$  and  $I_i$  the Young's modulus and moment of inertia for the top and bottom layers respectively. It is clear from the Eqs. 3.2 and 3.3 that for  $\xi = 0$ , the applied loading corresponds to mode I (DCB) loading ( $P_I = P_A = P_{\text{MMMB}}$  and  $P_{II} = 0$ ). For  $\xi = 1$ , the applied load corresponds to the conventional ENF loading ( $P_{II} = P_B$  and  $P_I = -P_{\text{MMMB}} \frac{K\alpha}{2\beta(1+K)}$ ), where the presence of a negative mode I component leads to complications in the measurement of the mode II fracture toughness because of the compressive stress resulting in friction between the two delaminated crack surfaces. For instance, results published by Kolluri et al. [93] showed a large difference in the CERR values obtained between pure mode II and ENF tests for glued interface samples. However, for any given bilayer sample, there is a position at which the mode I component is zero at the interface and consequently a pure mode II loading is obtained. This pure mode II loading position can be identified in this loading geometry by (see appendix)

$$\xi_{II} = \frac{2(1+K)\beta}{K\alpha + 2(1+K)\beta}. \quad (3.4)$$

The pure mode II position is  $\xi = 0.8$  for the case of a homogeneous bilayer sample with equal thickness of the bulk layers and a setup with  $\alpha = \beta$ .

### 3.2.1 Advantages of the MMBB setup

The following reported advantages of the original MMBB setup are recalled: (i) delamination can be tested over the full range of mode mixities, (ii) precise force measurement for small samples during delamination, (iii) *in-situ* testing under optical or electron microscope is possible which enables identification of the precise crack tip position and delamination mechanisms, and (iv) frictionless pure mode II test for accurate mode II fracture toughness determination. The functionality of the MMBB setup was demonstrated by *in-situ* delamination characterization of custom made glued interface structures [93].

### 3.2.2 Limitations - Motivation for an improved design

Even though the original MMMB setup was successful in carrying out *in-situ* tests on miniature structures, some limitations persist. First of all, the setup is limited in maximum force (20N) and displacement (depending on the mode mixity) necessary to achieve delamination particularly in mode II and mode II dominant tests. As reported in [93], the clearance in the dovetail connectors may still lead to hysteresis in loading-unloading cycles in the MMMB setup. Using image analysis of the displacements of the dovetail connectors, the influence of the hysteresis could be corrected (only) for mode I tests. Therefore, relatively high error margins may still be expected for mixed mode and mode II measurements. Additionally, some of the hinges in this design are unfavorably loaded in compression, which can lead to hinge failure due to buckling. Finally, the elastic hinges used in the design are fragile, and mounting and un-mounting of the sample demands special care. An improved version of the MMMB device is therefore designed and this design is analyzed, and validated on the CuLF-MCE specimens, as addressed in the next sections.

## 3.3 Improved Miniature Mixed Mode Bending setup

The design of the new improved MMMB focused on various fundamental improvements to the original MMMB setup in order to increase its maximum applicable load and stroke limits, to reduce undesirable clearances and to make the setup more robust. Improvements in the design are made by geometry optimization, performed at two structural levels to increase the maximum allowable displacement in the MMMB device. First, the total geometry of the improved MMMB was optimized for maximum global displacement using a finite element beam model of the setup. Next, the geometry of the elastic flexure hinge was optimized to provide more rotation in the critical hinges of the setup. The robustness of the setup was improved by several other modifications to the design including (i) a reversal of all compressive hinges (4 and 5) in the MLM to tensile hinges, (ii) increase in the thickness of the total device, and (iii) incorporation of additional tools for guiding, aligning and securing.

### 3.3.1 Optimization of the elastic hinge positions

A simple finite element beam model representing the MMMB device shown in figure 3.4 was used to optimize the geometry of the MMMB device. All the sections of the setup and samples are modeled as simple 2-node beam elements in MSC.Marc. In this model, elastic hinges connecting the beam elements are modeled with nodal ties (with rotation around z-axis being the only untied degrees of freedom) and rotational springs (to incorporate the elastic rotational stiffness and simulate the maximum rotational angle of the elastic hinges), as shown in Fig 3.4. The hinges in the model are numbered and represented with black circles. A beam model was used because

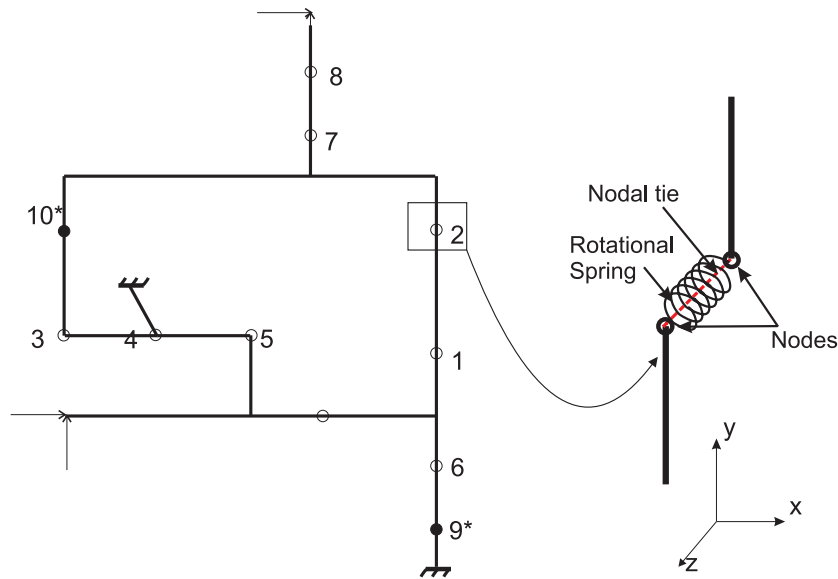


**Figure 3.4:** FE beam model of the MMMB setup with new additional hinges. An asterisk '\*' indicates the newly added elastic hinges (9 and 10). Details of the nodal ties and hinges are also shown.

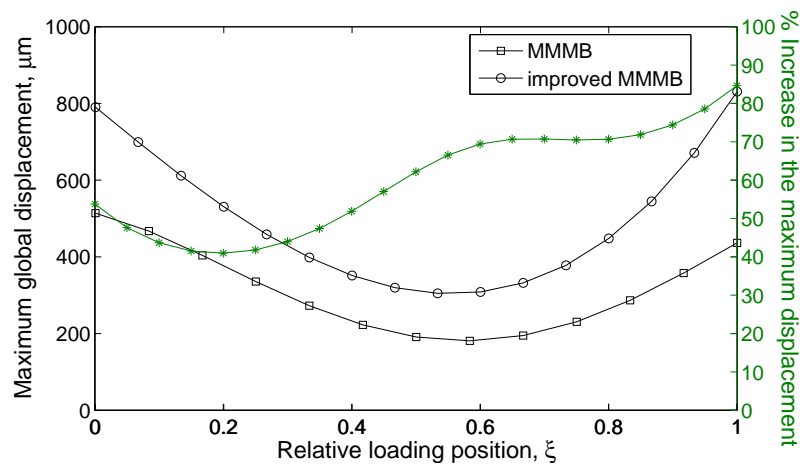


**Figure 3.5:** Comparison of the maximum global displacement between the original and improved MMMB configurations, obtained from FE beam simulations performed on a homogeneous bilayer sample with a fixed crack length of 6 mm.

it allows for fast analysis and updates of the position of the hinges and insertion of new hinges. Simulations were performed at all loading positions from  $\xi = 0$  to  $\xi = 1$  to identify the maximum global displacement at each position and the corresponding critical hinge, i.e. the hinge that reaches its maximum rotation first and therefore limits the maximum global displacement. Hinge 1 appeared to be the critical one in

most loading conditions, while mixed mode loading positions close to pure mode II were identified as the critical positions where the global displacements are minimal (Fig. 3.5). To improve the maximum displacements, two new hinges, one at the right bottom (hinge 9) and one at the left top corner (hinge 10) are inserted in the new design to reduce rotation of critical hinge 1. Figure 3.6 shows the schematic comparison between the old and new geometries at the same global displacement for a mixed mode test. It is clear from the figure that adding the extra hinges (9, 10) significantly reduces the rotation at hinge 1 (at the expense of increased rotation at hinge 6), which increases the maximum global displacement. From the beam simulations, it became also obvious that more space between hinges 1 and 2 decreases the rotation at hinge 1. In addition, optimization (to maximize distance between hinge 1 and 2) was performed such that the setup uses all the space available ( $73 \times 47 \times 29$  mm) in the micro-tensile stage (Kammrath & Weiss GmbH) which is sufficiently small to fit in a scanning electron microscope (SEM) vacuum chamber.

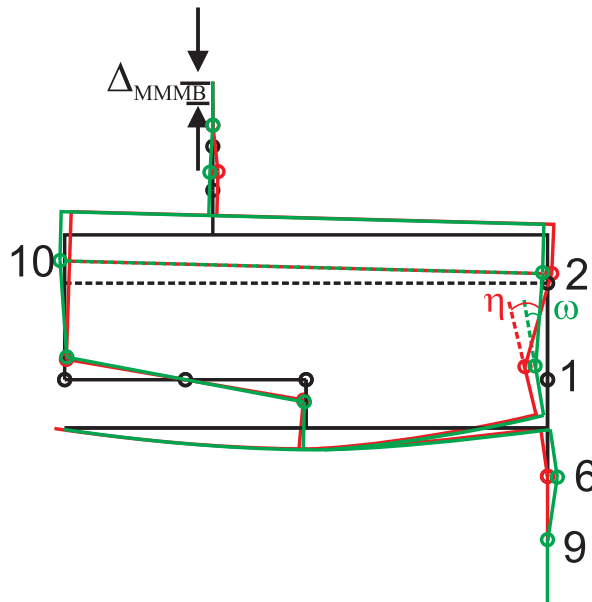


**Figure 3.6:** Schematic comparison between the old (red) and new (green) geometries loaded to the same global displacement for a mixed mode test, showing how the introduction of new hinges (9, 10) significantly reduces rotation ( $\omega < \eta$ ) at the critical hinge (no. 1).

### 3.3.2 Optimization of the hinge geometry

After the above-mentioned optimization of the hinge positions, it was concluded that (depending on the loading position) the rotations in hinges 1 or 6 limit the maximum global displacement of the device. Hence, a special elliptic hinge design, which is op-



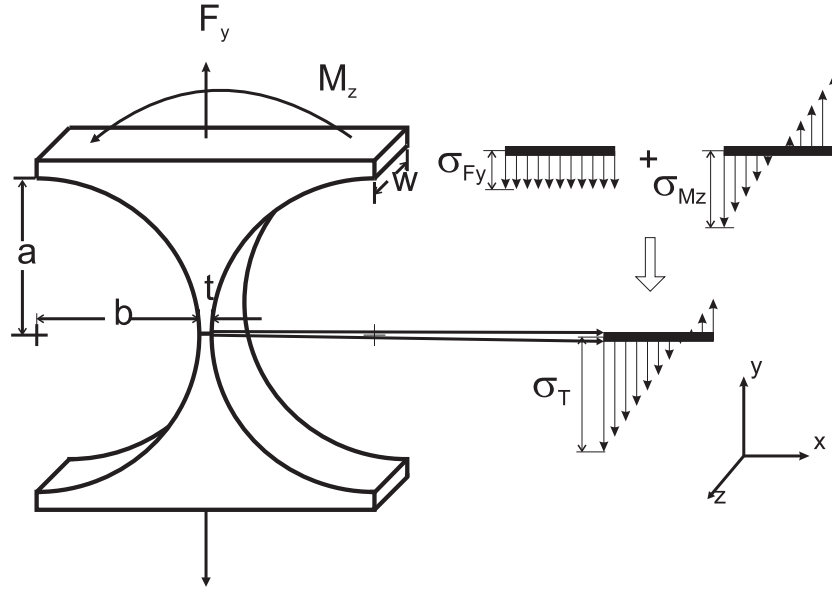


**Figure 3.7:** Elliptical flexure hinge with geometrical parameters. The stress distributions across the thickness at  $t$  due to the applied moment and the axial force are also shown.

timized for an increased maximum rotation, is used to replace the previous circular hinges in these critical locations. The other hinges were kept circular because they more accurately preserve the center of rotation than elliptical hinges [94, 95]. Figure 3.7 shows the parameters representing the geometry of the hinge. The maximum rotation of a hinge is determined by the geometry parameters ( $b/a$  ratio) that define the profile of the hinge, width  $w$  and the thickness  $t$  at the thinnest region of the elastic hinge. The thinnest hinge region with thickness  $t$  carries the bending stress,  $\sigma_{M_z}$ , and normal stress,  $\sigma_{F_y}$ , that can be applied to the hinge. Optimization of this thickness is done using the closed form compliance equation derived by Smith et al., [75] for elliptic hinges:

$$M_z = \frac{\theta_z E w t^3}{24 a \gamma}, \quad (3.5)$$

where  $\gamma$  is a lengthy function of  $b$  and  $t$ . The maximum total stress ( $\sigma_T$ ), which is at the surface, is the sum of the stress contribution from the applied moment around the  $z$ -axis ( $\sigma_{M_z} = K_t \frac{M_z t}{2 I_{zz}}$ , where  $K_t$  the stress concentration factor is a function of  $a$  and  $t$ , and where  $I_{zz}$  is the moment of inertia at  $t$ ) and the applied normal stress along the  $x$ -axis ( $\sigma_{F_y} = \frac{F_y}{t w}$ ). For a hinge in an elastic state,  $\sigma_T$  should remain below the yield strength  $\sigma_Y$  of the material, reduced with a safety factor  $\zeta$ , i.e.

$$\sigma_{M_z} + \sigma_{F_y} \leq \frac{\sigma_Y}{1 + \zeta}. \quad (3.6)$$

The maximum rotation of the hinge can be retrieved by rearranging equations (3.5) and (3.6) as,

$$\theta_z = \left[ \frac{\sigma_Y}{1 + \zeta} - \frac{F_y}{tw} \right] \frac{48aI_{zz}}{K_t E w t^4} \gamma(b, t). \quad (3.7)$$

$\theta_z$  in equation (3.7) can be treated as the objective function to maximize, leading to an optimal geometry of the hinge ( $t$ ,  $w$ ,  $a$  and  $b$ ). From Eq. 3.7, it is obvious that  $\theta_z$  increases monotonically with increasing hinge length,  $a$ , however, this is counteracted by a decrease in the precision of the rotation. Hence, the hinge profile ( $\frac{b}{a} = 0.8626$ ) suggested by Chen et al., [94] for optimal hinge performance with respect to maximum rotation at minimal stress concentration and maximum precision of rotation was used here. In addition, the width  $w$  was increased (from 2 mm in the original setup) to 6 mm in order to increase the allowable maximum axial force  $F_y$  from 20 N to 50 N. The other constraint is  $b \leq 3.25$  mm which is limited by the available space in the tensile stage. Using  $b = 3.25$  mm,  $\theta_z$  is plotted as a function of the thickness for an elliptic hinge in Fig. 3.8. A maximum rotation angle  $\theta_{zmax}$  of  $8.62^\circ$  is found (without any safety factor) for  $t = 28 \mu\text{m}$  as shown in Fig. 3.8. With a safety factor of  $\zeta = 0.2$ , the maximum rotation angle is reduced to  $\theta_{zmax} = 6.56^\circ$  for  $t = 34 \mu\text{m}$ . Based on the limited sensitivity to  $t$  around the maximum (Fig. 3.8), a value of  $t = 50 \mu\text{m}$  was adopted for the final design to avoid the region of high sensitivity of  $\theta_{zmax}$  to possible machining inaccuracies for small thicknesses. This slightly reduces the maximum rotation angle to  $6.27^\circ$ . In all, the maximum rotation has improved with 32% compared to the hinges in the original design, using the same safety factor. Moreover, the extent of the profile of the hinge on one side was reduced to the minimum distance ( $y = \frac{x}{2}$ ) without influencing the maximum rotation of the hinge [95], in order to maximize the distance between hinge 1 and 2 (Fig. 3.4).

### 3.3.3 Final improved MMMB design

Incorporating the above mentioned modifications, FE beam simulations were performed with the improved MMMB design to check its performance. The maximum global displacement was plotted as a function of the relative loading position in Fig. 3.5, which is improved by more than 60% for the critical loading positions close to pure mode II. Then, the improved MMMB device was manufactured by electrical discharge machining of the Ti-6Al-4V alloy plate. The final design of the improved MMMB device in comparison with the original MMMB device is shown in Fig. 3.9. All the important changes are highlighted and numbered. It is also noted that the improved design has 16 mode selector positions, instead of 13, in order to more accurately select the mode angle in the experiment. The main parts of the improved MMMB setup mounted in the micro-tensile stage are depicted in Fig. 3.10. Besides the above mentioned improvements in maximum load and displacement, also the remaining nonlinearities and robustness were further addressed, which is discussed next.

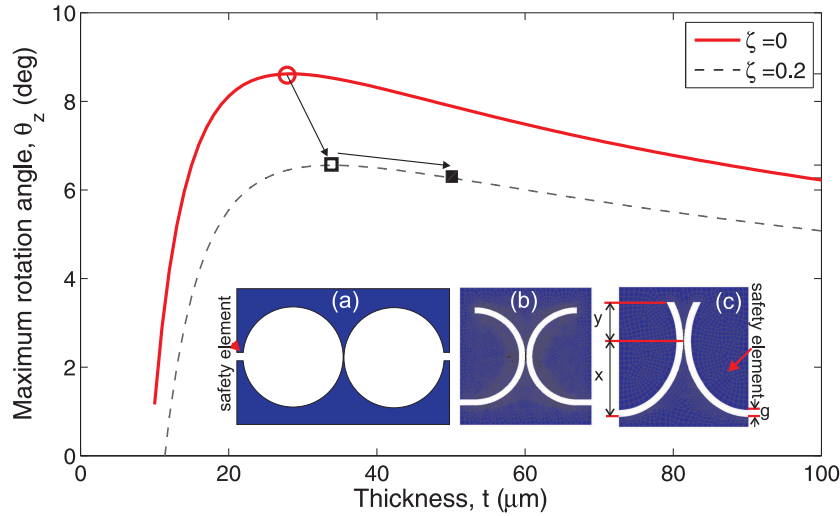


**Figure 3.8:** Maximum rotational angle  $\theta_z$  as a function of the thickness  $t$  of the hinge for  $w = 6$  mm,  $b = 3.25$  mm and  $\frac{b}{a} = 0.8626$ . Inset: (a) a conventional elastic hinge, (b) the circular hinge used in the original MMMB setup and (c) the new elliptic hinge design with a reduced profile on one side. The safety element closes the safety groove,  $g$ , once the hinge rotates to the maximum allowable rotational angle.

### 3.3.4 Clearance and Robustness of the setup

As was reported in [93], the clearance in the dovetail connectors resulted in hysteresis in the load displacement curves during loading-unloading tests in the original MMMB setup. The hysteresis can only be corrected for in mode I tests by tracking the connector clearance using a digital image correlation technique [96], a correction that is not possible in mixed mode and mode II measurements. To overcome this problem, new tapered dovetail connectors with wedge locking tools were manufactured as shown in Fig. 3.10b. With these tapered dovetails, mounting of the sample becomes easy and requires a relatively small force (in contrast to the original setup) which avoids any deformation of the hinges in the setup. After mounting the sample into the setup, the wedge tools are inserted to lock the dovetails without any clearance.

Since the elastic hinges used in the design are fragile, any damage of the hinge due to small forces during insertion and removal of the sample and the wedge locking tools and during actual loading should be avoided. Hence the following features have been adapted.

1. The thickness of the device is increased from 2 to 6 mm
2. The hinges at the mid loading position (hinge no. 4 and 5) are designed to be under tension to avoid any buckling of the hinges due to compressive loading in mode II dominated tests.

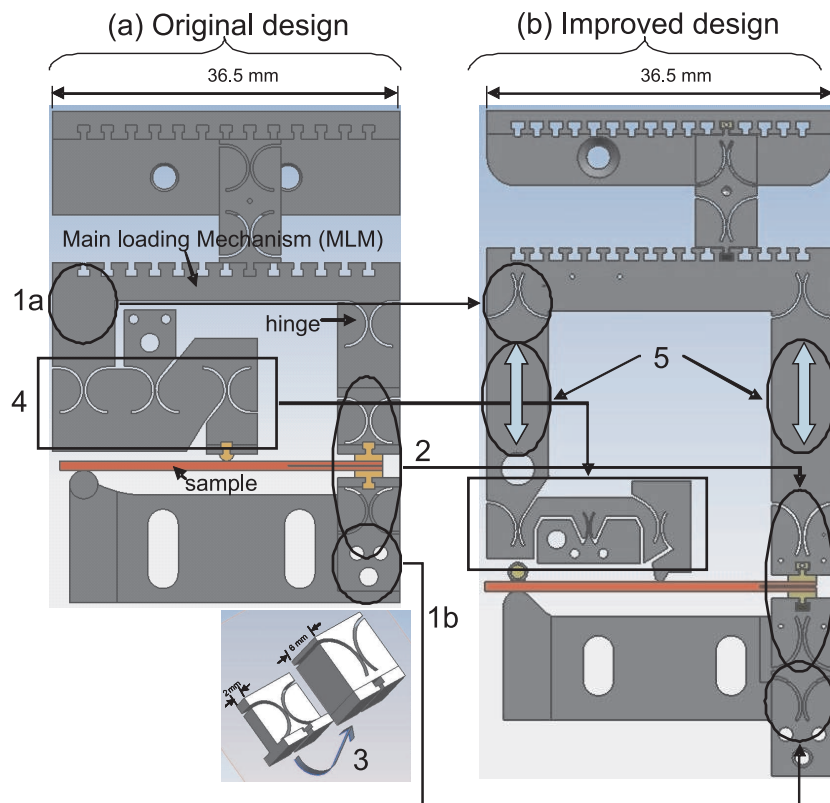


**Figure 3.9:** Design of (a) the original and (b) the improved MMBB setup. Improvements are highlighted and numbered: (1) introduction of new hinges, (2) replacement of the critical hinges with elliptical hinges for increased rotation, (3) optimization of hinge geometry and increased robustness, (4) redesign of compressive hinges to tensile loading, and (5) increased length of the MLM.

3. A separate bottom hinge shown in Fig. 3.10 (as 2b) is used when the load at this hinge is compressive ( $P_D < 0$ ) to avoid an unstable bottom hinge configuration.
4. Several components including guiding pins (to prevent in-plane motion) as well as a top and (movable) bottom supporting plate (to prevent out of plane motion) were introduced to provide mechanical isolation of the hinges and highly accurate alignment of the MLM during sample insertion and removal.

All these features significantly increase the robustness of the setup. Additionally, using these locking tools, the interface to be tested will also be protected from any external loads during the mounting process. In conclusion, the new robust setup increases the precision of the experimental load-displacement measurement by minimizing the risk for handling errors.

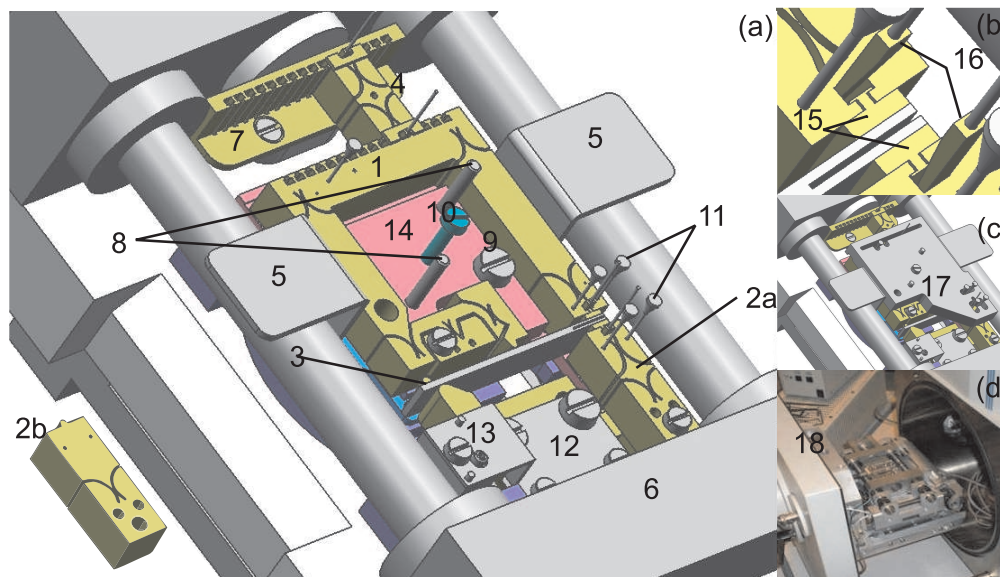


**Figure 3.10:** (a) the improved MMMB setup mounted in the micro-tensile stage: (1) main loading mechanism, (2a,2b) bottom hinges, (3) sample, (4) position selector, (5) handling plate, (6) micro-tensile stage, (7) position bar, (8) guiding rods, (9) set screw, (10) screw lock, (11) alignment pins, (12) sample height adjuster, (13) alignment screw, (14) bottom plate. (b): (15) new tapered dovetail connectors and, (16) wedge locking tools that remove any clearance in the connectors. (c): (17) top supporting plate (to lock the device during insertion and removal of the wedges) and (d): improved MMMB setup mounted in (18) SEM chamber.

## 3.4 Analysis of the new improved MMMB setup

### 3.4.1 Validation and accuracy assessment

The performance of the improved MMMB setup is evaluated using specially designed validation samples to assess the influence from inaccuracies in the manufactured geometry, machine compliance, or other factors such as clearance at the connectors. These samples are homogeneous single layer brass samples (i.e. without an interface and hence no propagating crack) with a well-defined notch, having an opening width of  $30\ \mu\text{m}$ , representing an existing crack of fixed length. The thickness of these samples is 1 mm. The inset in Fig. 3.11a shows the extremity with the notch in one of the test samples. Test samples with 5 different notch lengths (3, 6, 9, 12 and 15 mm) were used to check the performance of the setup. Tests were performed at all loading positions from mode I to pure mode II ( $\xi = 0 - 0.8$ ). Figure 3.11a shows the results of these tests performed on the 12 mm notch sample. The hysteresis observed in these tests is negligibly small, confirming the efficacy of the new wedge-locking dovetails with minimal clearance at the connectors (Fig. 3.10b). The relative hysteresis, defined as the dissipated energy during a loading-unloading cycle, relative to

the energy supplied during loading was calculated for all crack lengths and different loading positions. The maximum relative hysteresis was found to be 2% for pure mode II and the mean value is 1% for all loading positions. This is at least a factor of 2 smaller compared to the original design [93], even without the need for an elaborate digital image correlation correction procedure. To assess the precision of the complete experimental procedure, repeated tests were performed at one loading position by unmounting the sample after each test and remounting it for the next test. Because of the increased robustness and the new alignment tools, consistent results can be obtained (Fig. 3.11b). Specifically, the error in the stiffness was less than 0.7% which demonstrates the achieved precision of the new design.

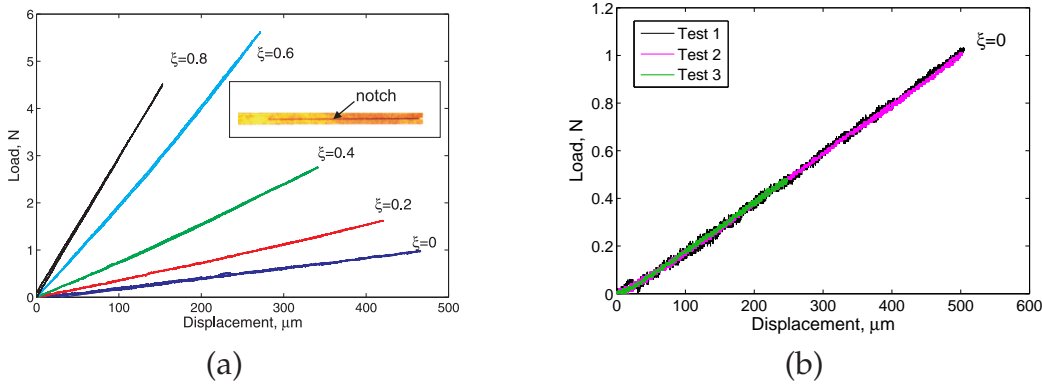


**Figure 3.11:** (a) Load-displacement results for loading-unloading cycles with the 12 mm validation sample at different loading positions (indicated by  $\xi$ ). The inset shows the notched extremity of a validation sample used for mode I to pure mode II tests  $\xi = 0 - 0.8$ . (b) Results of complete experimental repetition of 3 validation tests performed at  $\xi = 0$ . An error of less than 0.7% in stiffness was observed.

### 3.4.2 Finite Element Analysis

To determine the mode angle at the interface for different relative loading positions, finite element (FEM) simulations were performed for all loading positions using the beam model of the setup and an elastic material model of the CuLF-MCE sample. A fixed length of the precrack was modeled with a special rosette shape crack tip mesh. The mode angle,  $\psi$ , is defined by the orientation of the stress field. Because of the oscillating stress field in the dissimilar material interface (CuLF-MCE interface) [35],  $\psi$  is defined at a certain reference length,  $\delta$ :

$$\psi = \arctan \left( \frac{\sigma_{12}}{\sigma_{22}} \right)_{\delta}, \quad (3.8)$$

where  $\sigma_{22}$  is the normal stress,  $\sigma_{12}$  is the shear stress. The plastic process zone size is a common choice for the reference length  $\delta$  [35, 77] as it is the only intrinsic length scale in the system. The size of this process zone can be defined by the point where the linear elastic stress field equals the yield stress of the weakest of the two materials [35], which is  $\sim 5 \mu\text{m}$  in case of the CuLF-MCE samples. The mode angles calculated from the FEM simulations are plotted as a function of loading position in Fig. 3.12. The figure also shows this relation for a homogeneous bilayer sample with equal thickness of the bulk layers. These calculations demonstrate that the setup probes interface delamination over the complete range of mode angles for both homogeneous and dissimilar bilayer samples. Additionally, a strong feature of the MMMB concept is that the mode angle stays constant within a few degrees for different crack lengths and MLM displacements, as was shown in Fig. 2.9 for a homogeneous bilayer sample. A constant mode angle is in agreement with the analysis reported in [78]. There, it was shown that the mode angle always stays constant with increasing crack length for a homogeneous bilayer sample, however, in case of heterogeneous bilayer samples, the ratio of the crack length to the thickness of the layer ( $a/t$ ) should be sufficiently large to obtain a constant mode angle. The required value of this ratio depends on the material properties of both layers. For the case of CuLF-MCE system this ratio should be at least 6, whereas a value of  $\geq 12$  is used in the current analysis. It is also worth mentioning that FEM simulations taking into account the actual geometry of the setup, showed that at a maximum load of 50N, the displacement resulting from the compliance of the MMMB setup can be neglected with respect to the measured global displacement.

## 3.5 Study of coated copper lead frame - molding compound epoxy (CuLF-MCE)

### 3.5.1 Experimental procedure

*In-situ* experiments with the improved MMMB setup were conducted in a scanning electron microscope and under an optical stereo microscope at high magnifications. A batch of bilayer samples (manufactured at Philips Applied Technologies), consisting of 0.2 mm thick preplated (Au-Pd-Ni) copper lead frame and 0.5 mm thick molding compound epoxy, was tested in these experiments. The samples were prepared by heating the lead frame to 180°C for 2.5 minutes followed by high pressure hot injection molding of the molding compound epoxy. Afterwards, the samples were laser cut to the required dimensions (35 × 5 mm). After the molding, the samples received a post mold cure for 4 hours at 175°C. At the end of each sample, a well defined 6 mm long pre-crack was created by sliding a thin knife edge between the two layers using a home-built device. Prior to the experiment, samples were fine polished on one side (perpendicular to the plane of the interface) to visualize the interface at high magnifications. The dovetail connectors were attached on both sides

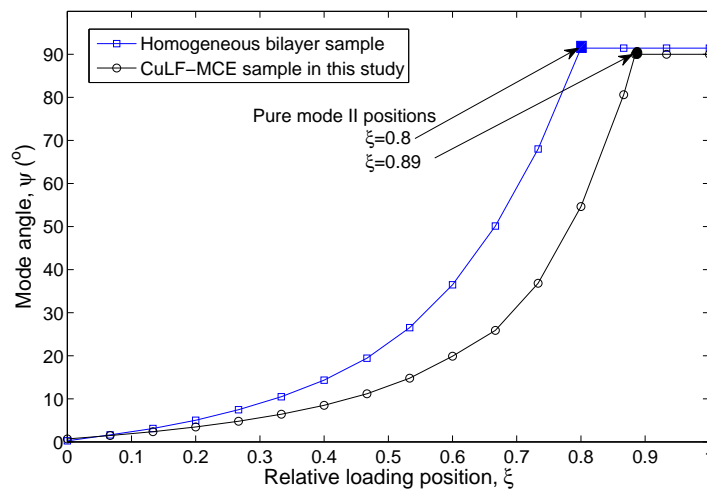


**Figure 3.12:** Mode angle obtained by FEM analysis as a function of relative loading position ( $\xi$ ) for (i) a homogeneous equal thickness bilayer sample (see Fig. 2.9 for material properties and dimensions) and (ii) the CuLF-MCE sample used in this study ( $t_{CuLF} = 0.2$  mm,  $t_{MCE} = 0.5$  mm,  $E_{CuLF} = 120$  GPa and  $E_{MCE} = 30$  GPa, where  $t$  is thickness and  $E$  is Young's modulus), with a crack length of 6 mm at 200  $\mu$ m MLM displacement.

of the samples with a stiff glue at the pre-cracked end, after which the samples were carefully mounted into the setup, by applying the robust sample insertion procedure with locked elastic hinges, as explained in section 3.3.4. Finally, the position selector was reinserted at the appropriate position to carry out a delamination experiment at the desired mode angle. During the test, the sample was unloaded and reloaded at regular intervals. At each load reversal, images of the crack tip were recorded at a magnification of 250x. These images were used to determine the crack length corresponding to the load reversals in the post processing analysis. On the basis of these experiments, the interface properties of the preplated CuLF-MCE interface structure were characterized over a complete range of mode mixities, thereby demonstrating the strengths of the setup.

### 3.5.2 Results and discussion

Figure 3.13 shows the load-displacement plots of the *in-situ* experiments conducted under a stereo microscope, at mode I ( $\xi = 0$ ) and mixed mode loading positions ( $\xi = 0.4, 0.67$  and 0.8). Initially, in all mode mixities, the load increases linearly with increasing displacement until the onset of crack initiation. Subsequently, a gradual drop in the load is observed with further displacement due to crack propagation. It is observed that the maximum at the onset of crack initiation in the first loading-



unloading cycle is less pronounced compared to the sharp maximum observed in the subsequent cycles, as highlighted in red in Fig. 3.13 for the mode I curve. This smooth behavior in the first cycle is attributed to the gradual development of a sharp microscopic crack tip and stable crack front normal to the crack propagation direction. Hence, before the actual delamination experiment at certain mode mixity, each sample was first loaded in mode I (position  $\xi = 0$ ), until the initiation of a sharp stable crack front was established. This first mode I cycle was ignored for the calculation of the CERR and is also not shown for the mixed mode experiments in Fig. 3.13.

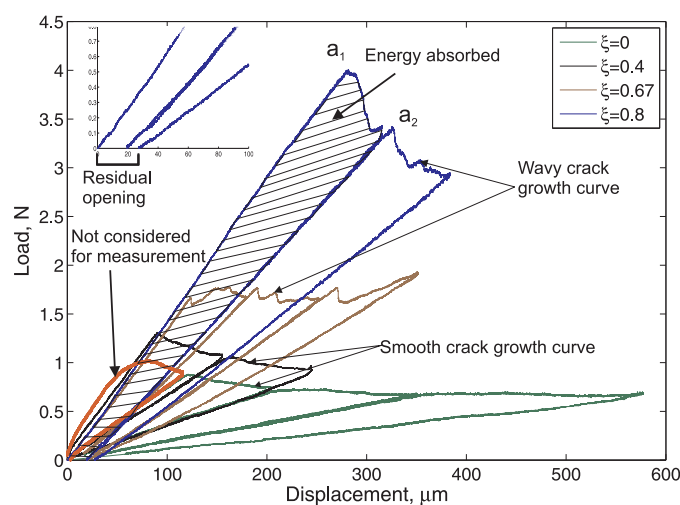


**Figure 3.13:** Comparison of load-displacement plots of a mode I ( $\xi = 0$ ) and mixed mode ( $\xi = 0.4, 0.67, 0.8$ ) experiments conducted on CuLF-MCE samples. The inset shows a magnification around the origin of the  $\xi = 0.8$  curve illustrating the residual opening after unloading to zero load.

The critical energy release rate of the interface was calculated from the area between the successive loading-unloading stiffness lines (e.g. the hashed region in Fig. 3.13), divided by the delaminated area corresponding to an increase of the crack length from position  $a_1$  to  $a_2$ . A strong feature of the (improved) MMB setup is that it allows highly accurate determination of the increase in crack tip position under the SEM, therefore, there is no need to use approximate analytical formula or numerical tools for the crack length prediction to calculate the CERR values. The resulting CERR values are shown in Fig. 3.14 as a function of the mode angle (the latter is determined from FE simulations). Note that the CERR represents the macroscopic interfacial fracture energy (measured from the global load-displacement response), which includes contributions from all dissipative mechanisms within the process zone associated with fracture, include damage and plasticity in the interface and in the adjoining layers in the immediate vicinity of the interface, but also (stick-slip) friction

of the delaminated interface. Separate from the plasticity mechanisms within the fracture process zone, plastic dissipation can occur due to permanent deformation of the sample structure (structural plasticity) during delamination. This structural plasticity is particularly dominant when a ductile layer is present in the composite stack [80, 81]. For instance, the inset in Fig. 3.13 shows a zoom around the origin of the load-displacement plot for  $\xi = 0.8$ , revealing a residual opening after complete unloading indicating possible structural plasticity contributions to the measured CERR. These structural plasticity contributions to the total energy dissipated during delamination need to be separated for accurate CERR calculation. Identification and separation of the structural plastic contributions to the total energy spent is required for the calculation of CERR. This requires a dedicated numerical-experimental methodology which is beyond the scope of this work and is the focus of Chapter 5. For the present work, the maximum contribution to the measured CERR value due to structural plasticity has been estimated from Fig. 3.13 by assuming a full damage unloading behavior to the origin. A maximum deviation of 6% about the mean CERR value was observed in mode II dominant test at  $\xi = 0.89$ , while a negligible influence was observed in mode I or mode I dominant mixed mode tests.

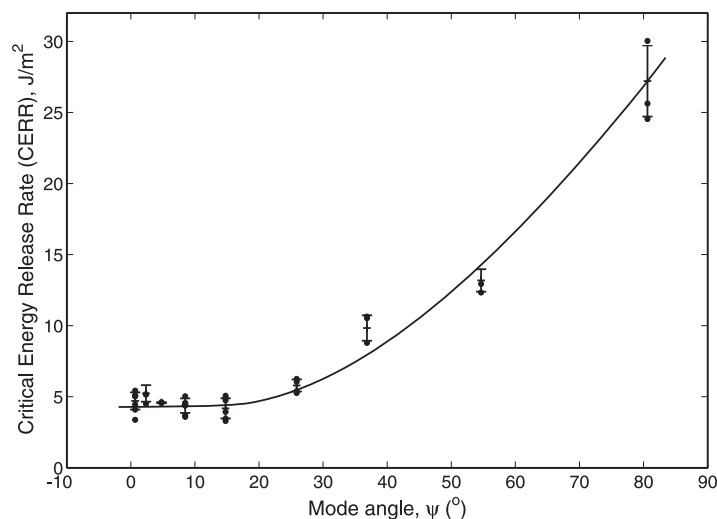


**Figure 3.14:** Critical energy release rate with standard deviation bandwidth as a function of (nominal) mode angle. Nominal mode angles are obtained from Fig. 3.12, where the relation between the relative loading position and the mode angle was established.

Besides the energy absorbed between two successive loading-unloading cycles, other important details are visible in Fig. 3.13. The first important observation is that the hysteresis of the setup, which can be measured from the unloading-reloading curves is negligible in all of the tests (even better than Fig. 3.11(a)). It is also clear that the curves (during crack growth) are smooth for mode I dominant tests (at  $\xi = 0$  and 0.4)

compared to the wavy curves in mode II dominant tests ( $\xi = 0.67, 0.8$ ). This difference in behavior can be attributed to the roughness of the bonded surfaces (which is  $\sim 1 \mu\text{m}$  RMS for the copper layer before molding) at the interface. Locally, the micro-scale roughness can lead to local shearing of and/or sliding between roughness asperities causing additional frictional dissipation which leads to an increased macroscopic interface fracture energy. In both cases, apart from the bulk layers that need to store more energy, a local crack opening displacement on the order of the roughness or size of the asperities is necessary for the crack to grow. In shear dominant tests (e.g. pure mode II), where the crack opening in normal direction is constrained, individual asperities will need to shear for the crack to grow. Therefore, either frictional sliding or local shearing can explain the discrete crack growth with its resulting characteristic wavy behavior for mode II dominant curves. To substantiate this hypothesis, *in-situ* delamination tests under SEM at high magnifications (under low vacuum mode) were carried out, confirming that the crack grows smoothly in mode I dominant tests ( $\xi = 0-0.53$ ), compared to more discrete or jerky crack growth in mode II dominant tests ( $\xi = 0.53-1$ ). This is also consistent with the trend in the CERR in Fig. 3.14, where a CERR of  $\sim 4.5 \text{ J/m}^2$  that is constant within experimental uncertainty was observed until  $\psi \approx 15^\circ$  (i.e.  $\xi = 0-0.53$ ), followed by a sharp increase with increasing mode angle towards position  $\xi = 1$ . To minimize the uncertainty in CERR measurement due to the jerky crack growth (resulting from stick slip behavior), the crack length increase between two consecutive unloads were kept sufficiently large in mode II dominant tests.

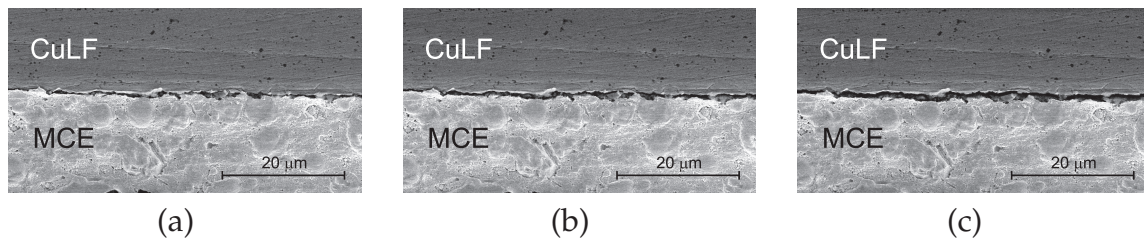


**Figure 3.15:** SEM micrographs showing the evolution of crack (from a-c) in the process zone during a mode I ( $\xi = 0$ ) delamination experiment. The crack is growing from the right to left.

In addition to the CERR measurements, real-time microscopic visualization allowed extraction of additional information at the delamination front to trace the formation and propagation of the crack in detail, providing valuable input for understanding of the fracture mechanism and for predictive simulations of the delamination in these interfaces. Specifically, the microscopic images allow for the following measurements.

1. The precise crack tip position can be determined within an accuracy of  $5 \mu\text{m}$ .
2. The delamination mechanism can be visualized at the interface. Figure 3.15 shows the evolution of the crack in the process zone. A brittle cleavage type of

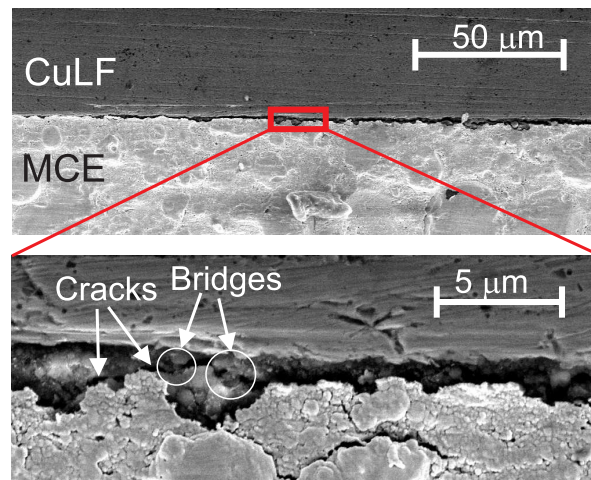


**Figure 3.16:** SEM micrograph showing small cracks and a limited number of bridges at the interfaces (for a mode I experiment).

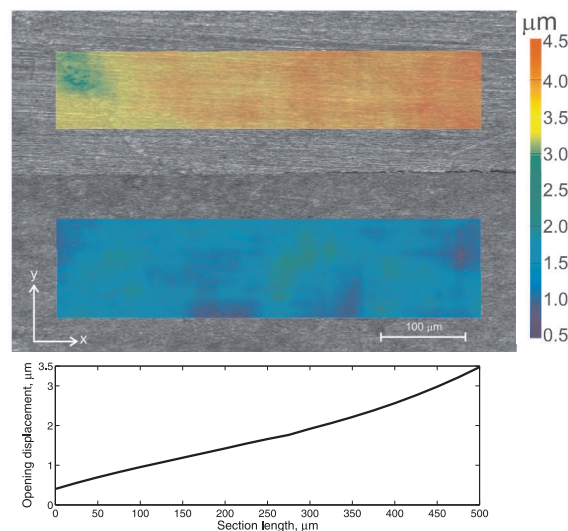


**Figure 3.17:** SEM micrograph with a DIC overlay of the y-displacement at a certain opening. Opening displacement as a function of section length is shown in the graph below.

failure was observed as the dominant mechanism indicating the brittle nature of the interface. At high magnifications, some bridges were observed as shown in Fig. 3.16.

3. The displacement field during delamination can be mapped using a digital image correlation (DIC) technique. As a first demonstration of resolving local strain fields, a DIC generated y-displacement field around the crack tip is

shown in Fig. 3.17. By measuring the evolution of the full profile of the crack opening during initiation of the delamination crack, important local information such as the elongation of the interface (glue) layer at the crack tip, and the rotation of the loading point can be extracted, which can be used in combination with the measured applied load and the sample width to calculate the full interface traction-separation law using the approach proposed by Andersson et al. [97].

## 3.6 Conclusions

An improved miniature mixed mode bending setup capable of *in-situ* delamination testing in advanced microscope systems (e.g. scanning electron microscope) has been proposed, designed, manufactured and tested. Improvements in the present design are: (i) optimal number and location of the hinges, (ii) optimal elastic hinge geometries for increased maximum rotation and (iii) minimized clearance at the connectors and increasing robustness of the setup with additional guiding and alignment tools. It was demonstrated that the improved setup exhibits

1. a wider application range to more interface systems because of its significant increase of the maximum accessible load and stroke in all mode mixities,
2. good accuracy in measuring the load-displacement response, as demonstrated from experiments on validation samples, confirming the significantly reduced hysteresis,
3. excellent experimental reproducibility characteristics due to the newly added alignment tools.

The improved setup was used for testing industrially relevant CuLF-MCE samples in the full range of mode mixities. Unloading-reloading tests performed at different mode mixities were used to calculate the CERR. In addition to the CERR measurements, real-time microscopic visualization allowed the identification of the difference in the crack growth behavior between different mode mixity tests. At small mode angles ( $\psi < 15^\circ$ ) relatively smooth crack growth behavior was observed resulting in a constant CERR value of  $\sim 4.5 \text{ J/m}^2$ . At mode angles greater than  $15^\circ$ , however, a jerky crack growth was observed with a serrated load-displacement response, which suggest its direct correlation with the observed increase in CERR with increasing mode angle from  $15^\circ$  to  $90^\circ$ . In-situ visualization also allowed to determine the precise position of the crack tip, and the crack opening displacement using DIC technique, as well as a qualitative assessment of the active delamination mechanism at the interface. A brittle cleavage failure type was observed for the investigated CuLF-MCE samples, while at high magnifications, some crack bridges were also observed.

## Appendix

Expressions for the mode I (Eq. 3.2), mode II (Eq. 3.3) and relative loading position for pure mode II (Eq. 3.4) are derived here. From Fig. 3.3, the force and moment balances directly yields Eq. 3.3,

$$P_{II} = P_B = P_{\text{MMMB}} \frac{\alpha}{\beta} \xi. \quad (3.3)$$

Other balance equations are,

$$P_A = P_I + P_E \quad (3.9)$$

$$P_E + P_F = \frac{P_{II}}{2}. \quad (3.10)$$

Combining  $K = \frac{P_E}{P_F}$  with Eq. 3.10 gives,

$$P_F = \frac{P_{II}}{2(1+K)} \quad (3.11)$$

$$P_E = K \frac{P_{II}}{2(1+K)}. \quad (3.12)$$

Substituting Eqs. 3.1a and 3.12 in Eq. 3.9, results in,

$$P_I = P_{\text{MMMB}}(1 - \xi) - K \frac{P_{II}}{2(1+K)}. \quad (3.13)$$

Furthermore, substituting Eq. 3.3 in Eq. 3.13 yields,

$$P_I = P_{\text{MMMB}} \left( 1 - \xi - \frac{K\alpha}{2\beta(1+K)} \xi \right), \quad (3.2)$$

which is the equation for mode I component (Eq. 3.2). For pure mode II loading, substituting  $P_I = 0$  in Eq. 3.2 and solving for  $\xi$  yields Eq. 3.4:

$$\xi_{II} = \frac{2(1+K)\beta}{K\alpha + 2(1+K)\beta}. \quad (3.4)$$



## CHAPTER FOUR

# Modeling and characterization of irreversible mixed mode interface delamination using a cohesive zone with combined damage and plasticity<sup>1</sup>

---

### Abstract

Delamination is often identified as an important failure mechanism in structures with high interface density, such as modern microelectronic systems and advanced composite materials. Delamination tests performed on different interface structures reveal complex failure mechanisms (crack bridging, grain bridging, fibre pull out, micro-void coalescence, fibrillation, crack meandering, etc.) in the fracture process zone that lead to an irreversible unloading response of the interface, ranging from full damage to full plasticity. Modeling such an unloading interface behavior is important in applications, such as crack branching and crack propagation at multiple interfaces, where the local unloading of the interface occurs during global loading of the structure. Therefore, this article presents an irreversible combined plasticity-damage unloading model, which can be used to extend the existing cohesive zone (loading) models with an unloading description that is suitable for modeling the unloading response resulting from fracture processes within the process zone. The presented model is able to model the change in unloading response as a function of mode mixity with coupling between different loading modes. As a demonstration, the improved Xu-Needleman cohesive zone law has been extended with the com-

---

<sup>1</sup>*Reproduced from:* M. Kolluri, J.P.M. Hoefnagels, J.A.W. van Dommelen, M.G.D. Geers, Modeling and characterization of irreversible mixed mode interface delamination using a cohesive zone with combined damage and plasticity, to be submitted.



bined damage-plasticity unloading formulation, and numerical simulations with this extended model performed on a glue interface system were found to mimic the observed behavior in delamination experiments, illustrating the applicability and relevance of the presented model. In addition, a procedure to extract the model parameters is presented and illustrated for the glue interface system.

## 4.1 Introduction

Interface delamination is often identified as the prominent failure mechanism in modern interface structures ranging from micro-electronic packages [3, 4], advanced aerospace composite structures [6, 7] to the adhesive joints in honeycomb sandwich structures [9], wind turbine blades [10], and for structural bonding of car body shells [98]. Primary causes of delamination failure include: high thermal mismatch stresses generated at the interface due to high density integration of dissimilar materials in electronic packages, poor adhesion characteristics between matrix and fiber in composite materials, and failure of glue in structures involving adhesive joints. Depending upon the interface type and loading state, different delamination failure modes varying from brittle de-adhesion, crack bridging to ductile yielding can be observed. Moreover, structures with a high interface density often fail by crack branching and delamination at multiple interfaces where local unloading at the interfaces can also occur while the structure is being loaded globally. Predictive finite element models are often used to minimize these failures during the design and optimization of these products. For successful prediction, a good interface model which can simulate both the loading (i.e. increasing separation) and unloading (i.e. decreasing separation) behavior of the interface is necessary. Cohesive zone models have been widely used in the literature [45, 46, 49, 51, 54, 57, 99–101] to model the constitutive loading behavior of the interface during delamination. Moreover, in addition to the loading behavior, a proper unloading description in a cohesive zone model is required for applications where interface unloading is important (e.g. crack branching and delamination at multiple interfaces etc). Without such an unloading description the irreversible unloading response that result from various fracture mechanisms (e.g. damage and plasticity) within the fracture process zone (FPZ) at the interface can not be simulated.

There are several studies in the literature [3, 59, 102–106], where the unloading behavior of the interface is modeled by extending the standard cohesive zone models with a pure damage description or a complete plasticity description of the interface. However, it is often difficult to model the unloading response with an a priori assumption of a pure damage or pure plasticity behavior because, in practice, the unloading of an interface can be more complex depending on the various dissipative fracture mechanisms within the FPZ (e.g. de-adhesion, cleavage failure, crack bridging, grain bridging, fibre pull out, micro-void coalescence, fibrillation, crack meandering). Based on the particular mechanism involved, the unloading can be categorized as damage (dominant) unloading, plasticity (dominant) unloading

or combined damage-plasticity unloading. For example, a brittle cleavage type of failure leads to damage unloading, where the elastic stiffness of the material is reduced by damage leaving zero separation upon complete unloading. On the other hand, pure ductile failure resulting from a micro-void coalescence mechanism leads to plastic unloading, where the material deforms plastically, allowing only elastic recovery upon unloading with the initial stiffness. Often a mechanism that causes both damage and permanent deformation of the interface (e.g. crack bridging) or a combination of different types of mechanisms can be present, leading to a more complex combined damage-plasticity type of unloading response. This can be illustrated with load-displacement curves (shown in Fig. 4.1) of the *in-situ* mixed-mode delamination growth (loading-delamination-unloading) experiments performed on two extreme types of (industrially relevant) interface systems: (i) a copper lead frame-molding compound epoxy (CuLF-MCE) interface representing a very brittle interface and (ii) an adhesive joint of two spring steel layers (glue interface) representing a more compliant interface. The sample geometry and loading conditions are given in Fig. 4.2 and material properties of the adherent structural layers of the two interface samples are the same as given in Fig. 3.12. The full details of the experiments have been reported in Refs. [93, 107]. From these unloading experiments, it can be seen that an interface can exhibit a linear unloading, either with a negligible retained opening after complete unloading indicating damage dominant mechanisms in the FPZ (as shown in Figs. 4.1(c)(i) and 4.1(a)(i)), or with significant retained opening (as shown in Figs. 4.1(c)(ii), 4.1(a)(ii) and 4.1(b)(i,ii)) indicating the presence of plasticity or combined damage-plasticity mechanisms within the FPZ assuming there is no plastic deformation in the sample structure. A combination of interface damage and plasticity is also commonly seen in the literature. For instance, Biel and Stigh [105] reported that both damage and plasticity accumulated at the crack tip influence the evaluated fracture properties. Modeling such a broad range of irreversible behaviors requires a cohesive zone model that is extended with an unloading description that can simulate the interface behavior ranging from full damage to combined damage-plasticity to full plasticity. Moreover, the measured Critical Energy Release Rate (CERR) varies strongly with loading mode [35, 77, 88] as also shown for both interface systems in Fig. 4.1(d). Therefore, the unloading model should allow for a change in unloading response as a function of mode mixity.

Since, there exist several physically motivated cohesive zone laws [45, 46, 49, 51, 54, 57] that are derived for a particular type of interface failure, in the current paper the aim is only to provide a suitable unloading model description that can be used to extend the behavior of existing cohesive zone (loading) laws with irreversible unloading. The model description should be such that the unloading response can be adapted to experimentally observed damage-plasticity behavior with a minimum number of model parameters such that they can be characterized from dedicated delamination experiments.

In conclusion, accurate description of the (range of) irreversible phenomena observed in delamination experiments calls for a generic unloading description that can be used to extend existing cohesive zone (loading) descriptions to simulate un-

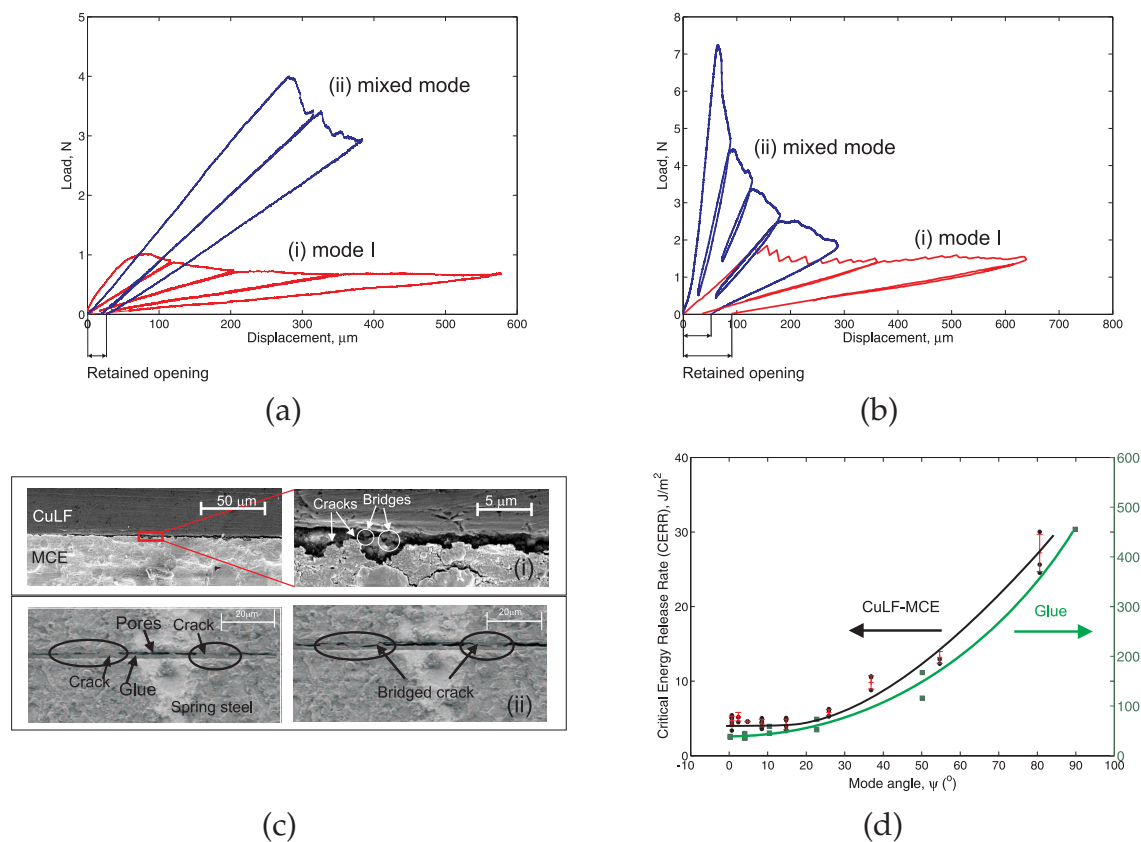


**Figure 4.1:** Results from delamination experiments on CuLF-MCE and glue interface samples [93, 107]. (a) load-displacement plots from delamination tests of the CuLF-MCE interface under (i) mode I and (ii) mixed mode loading (at 55° mode angle); (b) load-displacement plots of the glue interface under (i) mode I and (ii) mixed mode loading (at 23° mode angle); (c) SEM micrographs showing the delamination mechanism of (i) brittle de-adhesion with small bridging at the CuLF-MCE interface and (ii) large scale bridging associated with plasticity at the glue interface; and (d) the Critical Energy Release Rate versus mode angle, illustrating the strong dependency of the CERR on the mode angle.

loading behavior ranging from full damage to a combination of damage and plasticity to full plasticity under coupled mixed mode loading conditions. This article will provide such an experimentally motivated interface model as well as a methodology to determine the model parameters, as illustrated for delamination experiments on the above mentioned glue interface system.

The article is organized as follows. First, a new combined damage-plasticity model for irreversible unloading-reloading of a cohesive zone is described. Then, various interface cohesive zone models commonly used in the literature are briefly reviewed to select a model that is capable of simulating interface loading over the full range mode mixities with a coupling between different loading modes. As a demonstration, the improved Xu-Needleman cohesive zone (CZ) law is selected and ex-

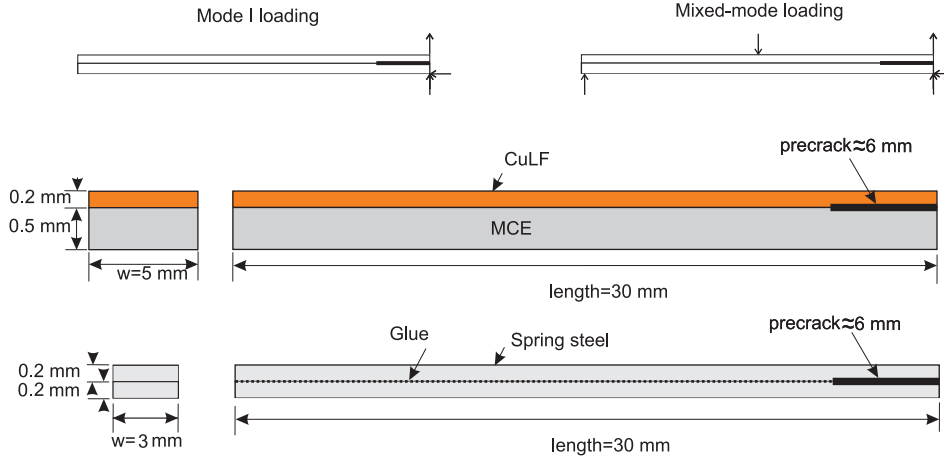


**Figure 4.2:** Geometry and the applied boundary conditions of the CuLF-MCE and glue interface samples.

tended with the combined damage-plasticity formulation to incorporate irreversible unloading-reloading behavior. Thereafter, various simulations are performed to illustrate the applicability of the new unloading model to simulate the observed irreversible behavior in experiments. Finally, a procedure for parameter characterization is given, after which conclusions are presented.

## 4.2 Irreversible unloading-reloading: a combined damage-plasticity description

A new combined damage-plasticity description for modeling the irreversible unloading-reloading behavior of a cohesive zone is presented in this section. For clarification, the two extreme cases of full damage and full plasticity are presented first before discussing the formulation for the combined damage-plasticity model. The combined damage-plasticity model (described below) can be generally employed to extend existing mixed mode cohesive zone laws (with or without coupling between different loading modes) that describe only the loading of the interface, with an irreversible unloading-reloading behavior. The normal and tangential traction-separation relations describing the loading behavior of a mixed mode cohesive zone law with coupling can be expressed in general by,

$$T_n = T_n(F_n(\Delta_n), F_t^c(\Delta_t)), \tag{4.1}$$

$$T_t = T_t(F_t(\Delta_t), F_n^c(\Delta_n)), \tag{4.2}$$

where  $\Delta_n$  and  $\Delta_t$  represent the separations in normal and tangential directions, respectively. Functions  $F_n(\Delta_n)$  and  $F_t(\Delta_t)$  describe the particular shape (e.g. bilinear, polynomial or exponential) of the traction-separation law and  $F_t^c(\Delta_t)$  and  $F_n^c(\Delta_n)$  are

functions that introduce coupling between two loading modes. For a given type of the cohesive zone, each of these functions are characterized by a set of characteristic parameters that determine the shape of the traction-separation law. For example, in case of an exponential cohesive zone law,  $\phi$ , and  $\delta$  represent the work of separation, and critical separation, respectively, with subscripts  $n$  and  $t$  indicating the normal and tangential directions as shown in Fig. 4.3.

In the following, Eqs. 4.1 and 4.2 will be extended with irreversible behavior upon unloading and reloading in the presence of coupling between different loading modes. The cross coupling terms (i.e.  $F_t^c(\Delta_t)$  in Eq. 4.1 and  $F_n^c(\Delta_n)$  in Eq. 4.2) vanish in case there is no coupling between different loading modes.

### 4.2.1 Damage formulation

In this section, a full damage description for the irreversible unloading-reloading of a cohesive zone is presented. In this formulation, the unloading stiffness corresponds to the secant stiffness of the chosen traction-separation curve as shown by line  $oq$  in Fig. 4.3(a) and 4.3(b).

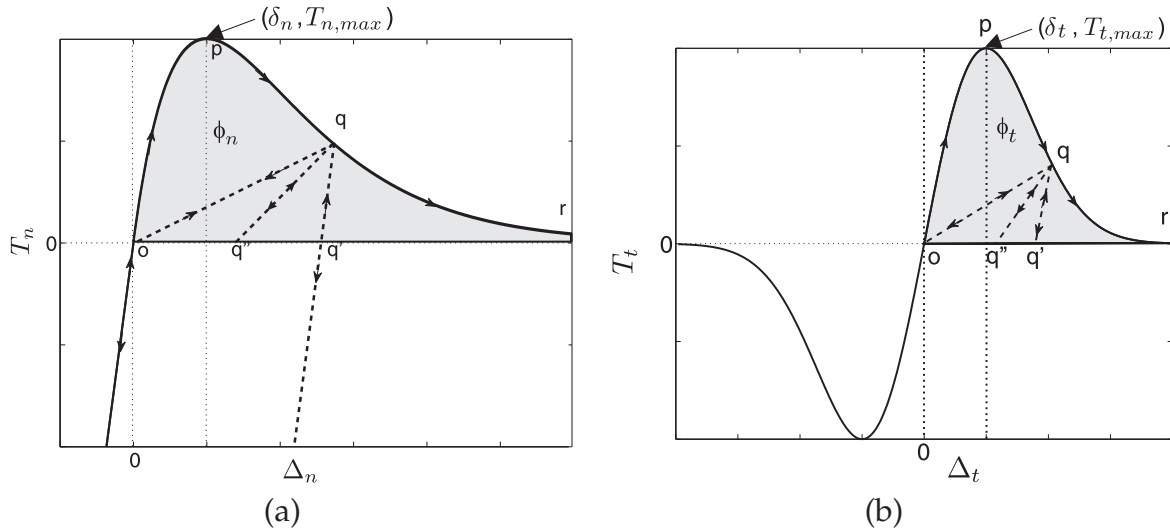


**Figure 4.3:** The unloading-reloading behavior for the full damage ( $oq$ ), full plasticity ( $qq'$ ) and combined damage-plasticity ( $qq''$ ) description are schematically depicted in an arbitrarily chosen (a) exponential normal traction-separation law (Eq. 4.31) and (b) exponential tangential traction-separation law (Eq. 4.35) that describe interface loading behavior.

The initial stiffness of the cohesive zone in normal and tangential directions is given by,

$$K_n^o = \left[ \frac{\partial T_n}{\partial \Delta_n} \right]_{\Delta_n=0, \Delta_t=0}, \quad (4.3)$$

$$K_t^o = \left[ \frac{\partial T_t}{\partial \Delta_t} \right]_{\Delta_t=0, \Delta_n=0}. \quad (4.4)$$

Upon loading, both the normal and tangential stiffness degrade with both normal and tangential openings. Hence, by introducing a damage parameter and a coupling term for cross degradation, the traction-separation equation for normal traction (Eq. 4.1) can be redefined as:

$$T_n = K_n^o(1 - d_n H(\Delta_n))(1 - d_{c,t} H(\Delta_n))\Delta_n, \quad (4.5)$$

where  $d_n$  is the damage due to normal opening and  $d_{c,t}$  is the cross degradation of the normal traction due to coupled tangential opening.  $H(\Delta_n)$  is the Heaviside function as given by:

$$H(\Delta_n) = \begin{cases} 0, & \Delta_n < 0, \\ 1, & \Delta_n \geq 0, \end{cases} \quad (4.6)$$

The damage parameters  $d_n$  and  $d_{c,t}$  present in Eq. 4.5 can be expressed as:

$$d_n = d_n(\Delta_{n,max}); \quad d_{c,t} = d_{c,t}(\Delta_{t,max}). \quad (4.7)$$

Herein,  $\Delta_{n,max}$  and  $\Delta_{t,max}$  are history variables indicating, respectively, the absolute maximum opening sustained sofar in normal and tangential directions. Similarly, for tangential loading, Eq. 4.2 can be written as,

$$T_t = K_t^o(1 - d_t)(1 - d_{c,n})\Delta_t, \quad (4.8)$$

where  $d_t$  is the damage due to tangential opening and  $d_{c,n}$  is the cross degradation of the tangential traction due to coupled normal opening as given in the following equations:

$$d_t = d_t(\Delta_{t,max}); \quad d_{c,n} = d_{c,n}(\Delta_{n,max}). \quad (4.9)$$

Damage growth with normal opening occurs if the following conditions are satisfied:

$$f_n = \Delta_n - \Delta_{n,max} = 0 \quad \text{and} \quad \dot{f}_n = 0. \quad (4.10)$$

The damage loading function  $f_n$  and the history parameter  $\Delta_{n,max}$  satisfy the following Kuhn-Tucker conditions:

$$f_n \dot{\Delta}_{n,max} = 0; \quad f_n \leq 0; \quad \dot{\Delta}_{n,max} \geq 0. \quad (4.11)$$

When  $f_n = 0$  and  $\dot{\Delta}_n > 0$  the damage,  $d_n$ , and the cross degradation,  $d_{c,n}$ , increase according to  $\dot{\Delta}_{n,max} = \dot{\Delta}_n$ . Similarly, the criterion for damage growth with the tangential opening is given by:

$$f_t = |\Delta_t| - \Delta_{t,max} = 0 \quad \text{and} \quad \dot{f}_t = 0, \quad (4.12)$$

where also  $f_t$  and  $\Delta_{t,max}$  satisfy the Kuhn-Tucker conditions:

$$f_t \dot{\Delta}_{t,max} = 0; \quad f_t \leq 0; \quad \dot{\Delta}_{t,max} \geq 0. \quad (4.13)$$

The damage,  $d_t$ , and the cross degradation,  $d_{c,t}$ , increase according to  $\dot{\Delta}_{t,max} = |\dot{\Delta}_t|$  when  $f_t = 0$  and  $\dot{\Delta}_t \Delta_t \geq 0$ .

## 4.2.2 Plasticity formulation

### Normal yielding

When the cohesive zone deforms fully plastically, unloading occurs with the initial stiffness of the traction-separation curve, leaving a remaining permanent opening  $\Delta_{n,p}$  at zero traction. The total normal separation is the sum of an elastic contribution and a plastic contribution, i.e.  $\Delta_n = \Delta_{n,e} + \Delta_{n,p}$ . The yield traction for normal separation is given by the following equation:

$$T_{n,y} = F_n(\Delta_{n,eff})(1 - d_{c,t}), \quad (4.14)$$

where  $\Delta_{n,eff}$  is a history variable corresponding to the effective maximum opening sustained sofar in normal direction as defined further on (in Eq. 4.19), and  $d_{c,t}$  is the cross degradation term (due to coupling) as given in Eq. 4.7. The initial yield traction is zero and the plasticity begins only with the onset of positive normal loading. The normal traction is then given by:

$$T_n = K_{nn}^e \Delta_{n,e}, \quad (4.15)$$

where,  $K_{nn}^e = K_n^o [1 - d_{c,t} H(\Delta_{n,e})]$  represents the elastic stiffness of the normal cohesive zone after cross degradation due to tangential opening.  $H(\Delta_{n,e})$  is the Heaviside function as given by:

$$H(\Delta_{n,e}) = \begin{cases} 0, & \Delta_{n,e} < 0, \\ 1, & \Delta_{n,e} \geq 0, \end{cases} \quad (4.16)$$

indicating no degradation of the compressive stiffness due to the coupling term ( $d_{c,t}$ ), see Fig. 4.4(a). The yield condition for normal loading is then:

$$f_{n,y} = T_n - T_{n,y} = 0, \quad \text{and} \quad \dot{f}_{n,y} = 0, \quad (4.17)$$

satisfying the following Kuhn-Tucker conditions:

$$f_{n,y} \dot{\Delta}_{n,eff} = 0; \quad f_{n,y} \leq 0; \quad \dot{\Delta}_{n,eff} \geq 0. \quad (4.18)$$

Next,  $\Delta_{n,eff}$  is defined by the following logical statements:

$$\begin{aligned} (f_{n,y} = 0) \wedge (\dot{\Delta}_n > 0) &\Rightarrow \dot{\Delta}_{n,eff} = \dot{\Delta}_n; \\ (f_{n,y} < 0) \vee (\dot{\Delta}_n \leq 0) &\Rightarrow \dot{\Delta}_{n,eff} = 0. \end{aligned} \quad (4.19)$$

Since this is a coupled formulation, degradation of the normal traction due to tangential opening is incorporated. The criterion for cross degradation of the normal traction (due to coupling) with tangential opening (as shown in Fig. 4.4(a)) is given by Eqs. 4.12 and 4.13.

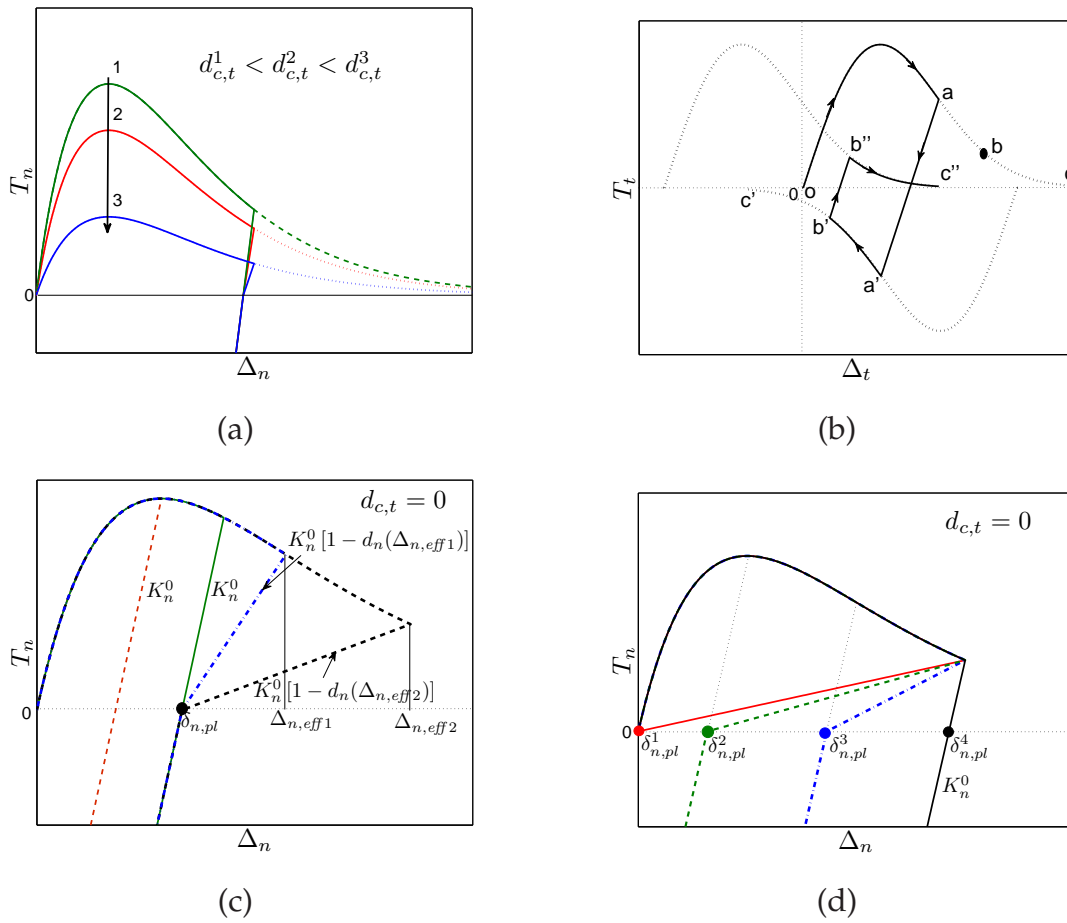


**Figure 4.4:** (a) Influence of the coupled damage ( $d_{c,t}$ ) term on the normal traction-separation law with fully plastic unloading. (b) The yielding behavior of the tangential traction-separation law when the loading direction is reversed (at a and b'). The equivalent curve oabc shows the response when the CZ is loaded monotonically in one direction. (c) The unloading behavior of the new combined plasticity-damage CZ in normal opening above and below the plastic limit ( $\delta_{n,pl}$ ). (d) The influence of  $\delta_{n,pl}$  on the unloading behavior of the new combined plasticity-damage CZ in normal opening.



### Tangential yielding

Similar as for normal yielding, the total tangential separation is written as  $\Delta_t = \Delta_{t,e} + \Delta_{t,p}$  and the yield traction for tangential separation is:

$$T_{t,y} = F_t(\Delta_{t,eff})(1 - d_{c,n}), \quad (4.20)$$

where  $\Delta_{t,eff}$  represents the effective maximum opening sustained so far in tangential direction, as defined further on, in Eq. 4.24. Similar to normal yielding, the initial yield traction is zero, but plasticity sets in with the onset of loading in both positive and negative shear directions, as shown in Fig. 4.4(b). The tangential traction is given by

$$T_t = K_{tt}^e \Delta_{t,e}, \quad (4.21)$$

where  $K_{tt}^e = K_t^o(1 - d_{c,n})$  represents the elastic stiffness of the cohesive zone after cross degradation due to normal opening. Note that in contrast to the normal traction, the tangential traction is affected by cross degradation due to the coupling term for both positive and negative separations. The coupling parameter  $d_{c,n}$  is defined in Eq. 4.9. The yield criterion differs from Eq. 4.17 because yielding can occur in both directions in shear (Fig. 4.4(b)):

$$f_{t,y} = |T_t| - T_{t,y} = 0, \quad \text{and} \quad \dot{f}_{t,y} = 0, \quad (4.22)$$

satisfying the following Kuhn-Tucker conditions:

$$f_{t,y} \dot{\Delta}_{t,eff} = 0; \quad f_{t,y} \leq 0; \quad \dot{\Delta}_{t,eff} \geq 0. \quad (4.23)$$

Next,  $\Delta_{t,eff}$  is defined by the following logical statements:

$$\begin{aligned} (f_{t,y} = 0) \wedge (\dot{\Delta}_t \Delta_{t,e} \geq 0) &\Rightarrow \dot{\Delta}_{t,eff} = |\dot{\Delta}_t|; \\ (f_{t,y} < 0) \vee (\dot{\Delta}_t \Delta_{t,e} < 0) &\Rightarrow \dot{\Delta}_{t,eff} = 0. \end{aligned} \quad (4.24)$$

The criterion for cross degradation of the tangential traction (due to coupling) with normal opening is defined by Eqs. 4.10 and 4.11.

### 4.2.3 Combined plasticity-damage formulation

As explained earlier, it is often observed in reality that the fracture process zone at the interface during delamination comprises a combination of damage and plasticity mechanisms leading to an unloading-reloading response that is in between full damage and full plasticity behavior as shown by line qq'' in Figs. 4.3(a) and 4.3(b). Therefore, in this section, a combined plasticity-damage formulation of the cohesive zone is given that is suitable to model the unloading response resulting from both damage and/ plasticity mechanisms as is observed in experiments (Section 4.1). To

be able to achieve this, both damage and plasticity accumulations are incorporated in a single cohesive zone by combining both the damage description of Section 4.2.1 and the plasticity description of Section 4.2.2 and by introducing a new parameter called the plastic limit ( $\delta_{pl}$ ) to vary the ratio of the plastic energy and the damage energy of separation. Correspondingly, Eqs. 4.15 and 4.21 of the fully plastic formulation are reformulated as:

$$T_n = K_n^o(1 - d_n H(\Delta_{n,e}))(1 - d_{c,t} H(\Delta_{n,e}))\Delta_{n,e}, \quad (4.25)$$

$$T_t = K_t^o(1 - d_t)(1 - d_{c,n})\Delta_{t,e}, \quad (4.26)$$

where  $H(\Delta_{n,e})$  is defined in Eq. 4.16 and,  $d_n$  and  $d_t$  are damage parameters that evolve with  $\Delta_{n,eff}$  and  $\Delta_{t,eff}$ , respectively, similar to  $\Delta_{n,max}$  and  $\Delta_{t,max}$  in Section 4.2.1, however, such that until the effective plastic opening reaches the plastic limit, the cohesive zone behaves fully elasto-plastic:

$$\Delta_{n,p,eff} \leq \delta_{n,pl} \quad \rightarrow \quad d_n = 0; \quad (4.27)$$

$$\Delta_{t,p,eff} \leq \delta_{t,pl} \quad \rightarrow \quad d_t = 0, \quad (4.28)$$

where  $\Delta_{n,p,eff} = \Delta_{n,p}$  and  $\Delta_{t,p,eff} = \int |\dot{\Delta}_{t,p}| dt$ , are the effective plastic opening in normal and shear direction, respectively, and  $\delta_{n,pl}$  and  $\delta_{t,pl}$  are the plastic limits in normal and tangential direction. The conditions for yielding are the same as in Section 4.2.2 for both normal and shear loadings. Similar to the plasticity formulation (Section 4.2.2), the conditions for cross degradation (due to coupling) with normal and tangential openings for the combined plasticity-damage formulation are given by Eqs. 4.10 and 4.11 and Eqs. 4.12 and 4.13, respectively. The behavior of this plasticity-damage formulation is most clearly represented in Fig. 4.4(c): once the effective maximum separation passes the critical limit ( $\Delta_{n,p,eff} > \delta_{n,pl}$ ,  $\Delta_{t,p,eff} > \delta_{t,pl}$ ), the plastically deformed cohesive zone damages with further separation because the damage parameters  $d_n$  and  $d_t$  are defined such that the plastic opening does not grow any further:

$$d_n = d_n(\Delta_{n,eff}, \delta_{n,pl}); \quad (4.29)$$

$$d_t = d_t(\Delta_{t,eff}, \delta_{t,pl}). \quad (4.30)$$

This combined plasticity-damage formulation gives the required freedom to describe a cohesive zone failing with partial damage and partial plasticity by adapting the ratio of the plastic energy and the total work of separation. That means, by choosing the plastic limit  $\delta_{pl}$  from zero to infinity, this ratio can be varied from zero to 1, i.e. the irreversible interface behavior can be varied from full damage unloading to a mixture of damage and plasticity to full plastic unloading (see Fig. 4.4(d)). Therefore, this new combined formulation gives clear added value by providing the required freedom to model the experimentally observed irreversible behavior with only two additional parameters  $\delta_{n,pl}$  and  $\delta_{t,pl}$  in addition to the characteristic parameters of the CZ law.

### 4.3 Selection of a basis CZ law

The goal of this section is to briefly explore the existing CZ models in the literature and to select the most suitable basis model which will be extended with the combined damage-plasticity formulation described in Section 4.2.

The cohesive zone concept has been first introduced by Barenblatt in 1959 [46, 108] to model cracks in brittle materials. In this approach, discontinuities are introduced to model cracks in a continuum material. Constitutive equations (referred to traction-separation laws) relating normal and tangential displacement jumps across the discontinuity with proper tractions define a cohesive zone model (CZM). Later, Dugdale in 1960 [45] used a similar concept to model the yielding of thin ideal elastic-plastic steel sheets containing slits. Afterwards, several cohesive zone models have been proposed in the literature to solve wide varieties of fracture problems. Some examples include the cohesive zone model introduced by Needleman [109, 110] for solving particle-matrix de-cohesion problems, by Rice and Wang [111] to model embrittlement of interfaces by solution segregation, by Tvergaard and Hutchinson [48] for debonding in whisker reinforced metal matrix composites, by Xu and Needleman [50] for void nucleation by inclusion de-bonding, by Camacho and Ortiz [52] for modeling impact damage in brittle materials, by Geubelle and Baylor [112] for impact-induced delamination in laminated composites, by Li et al. [57] for fracture of a fiber-reinforced polymer-matrix composites, and by Van den Bosch et al. [58] for delamination in polymer-metal interfaces. From these examples, it is clear that the concept of a CZ model is generic, however, the characteristics of the cohesive law should be motivated by the ability to capture the associated dissipative mechanisms during fracture or delamination as observed in experiments.

The above mentioned CZ models have different shapes of the traction-separation curves. According to the elementary functions used in CZ models, they can be classified as (1) multilinear, (2) polynomial, and (3) exponential. Traction-separation relations for interface loading in normal and tangential directions for the rigid linear [52], piecewise linear [55], polynomial [48], linear exponential [53], and exponential [50] cohesive zone laws are depicted Fig. 4.5. A common feature in all these laws (except for the rigid linear CZ law) is an initial hardening branch followed by a softening tail. The exact shape of the cohesive law is generally assumed to be inconsequential for the prediction of fracture involving small scale bridging phenomena. However, in cases where large scale bridging occurs, the shape plays an important role because the associated process zone size becomes comparable to the geometrical length scales in the problem. Still, the shape does not affect the calculations for crack propagation, for which the characteristic strength and toughness are the only important parameters [28, 57]. However, for the current purpose of finding an appropriate CZ loading model which serves as a basis to demonstrate the combined plasticity-damage unloading model, a generic model that can describe crack growth during delamination in brittle as well as ductile interfaces is needed. Moreover, such a model should allow for modeling delamination over the full range of mode mixities. To this end, the Xu-Needleman exponential CZ law seems most promising, because it has been

extensively used for the analysis of a wide variety of problems involving, e.g., debonding in adhesive joints [113], delamination by fibrillation in polymer coated steel [114], interface cracking in dissimilar bi-material interfaces [100], as well as failures in IC interconnects and solder joints [59, 115]. Additionally, for the few cases where the explicit traction-separation behavior of the adhesive layer has been measured directly [55, 105], the traction-separation behavior seems best described by this exponential cohesive law. The exponential cohesive law is also the most popular because of its automatic phenomenological description of contact under normal compression, while the continuity of tractions and their derivatives eases the computational implementation. Because of these reasons, for the present purpose, Xu-Needleman exponential cohesive zone model was selected as the best generic choice for the shape of the cohesive zone.

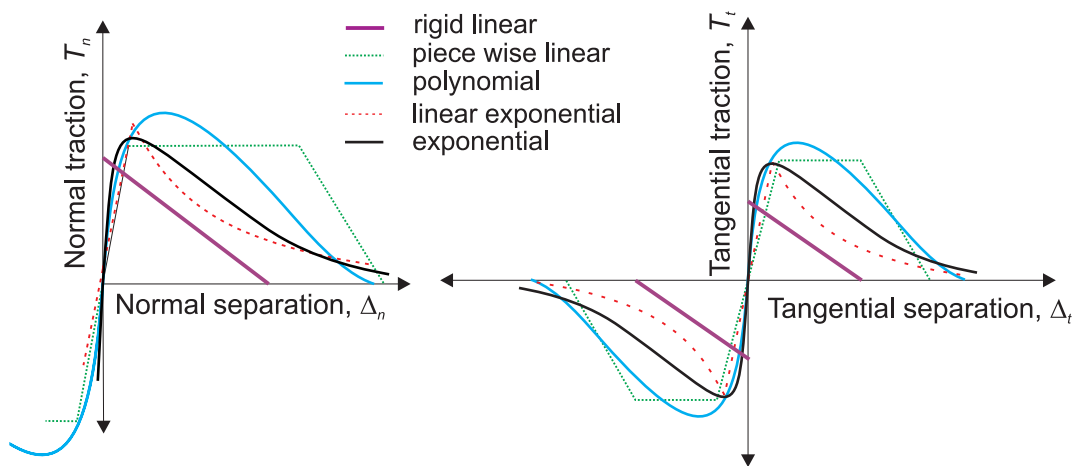


**Figure 4.5:** Schematic of the different cohesive zone laws for interface loading commonly used in the literature.

To accurately simulate mixed mode delamination for arbitrary loading paths, good coupling between the two loading modes is required. In many cohesive zone models, this coupling is achieved by using an effective opening displacement  $\lambda$  which is a function of normal and tangential openings, or by using coupling parameters. In the former approach, where  $\lambda$  is used, both normal and tangential tractions are described as a function of  $\lambda$  to incorporate degradation of normal traction due to tangential separation and vice versa. However, Zhang and Paulino [116], showed that coupling with  $\lambda$  leads to an identical work of separation for normal and tangential loadings which disqualifies its applicability to problems where the work of separation (or equivalently, CERR) varies (strongly) with mode angle, as shown, e.g., in Fig. 4.1(d). Alternatively, in Xu-Needleman [50] exponential cohesive law, coupling between the loading modes is achieved by two coupling parameters which relate the ratio between energy release rates of pure mode I and mode II loading and the corresponding displacements. However, it was shown by Van den Bosch et al. [58]

that this model shows unrealistic artifacts for mixed mode loading unless the energy release rates of modes I and mode II are again equal. Therefore, Van den Bosch et al. [58] proposed an improved version of the original Xu-Needleman exponential cohesive zone law which allows modeling of a realistic coupled mixed mode behavior (i.e. complete degradation of normal strength with an infinite separation only in tangential direction and vice versa) with different values for the mode I and mode II critical energy release rates.

This improved CZ law will be used for the present purpose as a basis for implementing the combined damage-plasticity unloading description proposed in Section 4.2 in order to (i) demonstrate the capability of the model to simulate unloading responses varying from full damage to full plasticity under mixed mode conditions with only two additional model parameters and (ii) describe the observed trends of retained opening after complete unloading in experimental results presented for the glue interface system in Fig. 4.1(b).

## 4.4 Extension of improved Xu-Needleman model with damage and plasticity

In this section, the improved Xu-Needleman model is extended with a description of the unloading-reloading behavior incorporating either damage, plasticity or a combination of damage and plasticity.

### 4.4.1 Exponential cohesive zone law proposed by Van den Bosch et al.

The improved Xu-Needleman exponential cohesive zone law for interface loading proposed by Van den Bosch et al. [58] is given by the following equations for normal and tangential tractions:

$$T_n = \frac{\phi_n}{\delta_n} \left( \frac{\Delta_n}{\delta_n} \right) \exp \left( -\frac{\Delta_n}{\delta_n} \right) \exp \left( -\frac{\Delta_t^2}{\delta_t^2} \right), \quad (4.31)$$

$$T_t = 2 \frac{\phi_t}{\delta_t} \left( \frac{\Delta_t}{\delta_t} \right) \exp \left( -\frac{\Delta_t^2}{\delta_t^2} \right) \exp \left( -\frac{\Delta_n}{\delta_n} \right) \left( 1 + \frac{\Delta_n}{\delta_n} \right), \quad (4.32)$$

where  $\phi$ ,  $\Delta$  and  $\delta$  represent the work of separation, separation, and critical separation, respectively, with subscripts  $n$  and  $t$  indicating the normal and tangential directions. A constant elastic stiffness ( $\phi_n/\delta_n^2$ ) is used to describe  $T_n$  in the compressive regime (i.e. when  $\Delta_n < 0$ ). The above traction-separation law is plotted in Fig. 4.6(a) for pure mode I ( $\Delta_t = 0$ ) and in Fig. 4.6(b) for mode II ( $\Delta_n = 0$ ) loading cases. From Fig. 4.6(b) it can be observed that the maximum tangential traction does not correspond to an opening of  $\delta_t$  giving rise to a non-physical definition of  $\delta_t$ . Therefore, Eq.

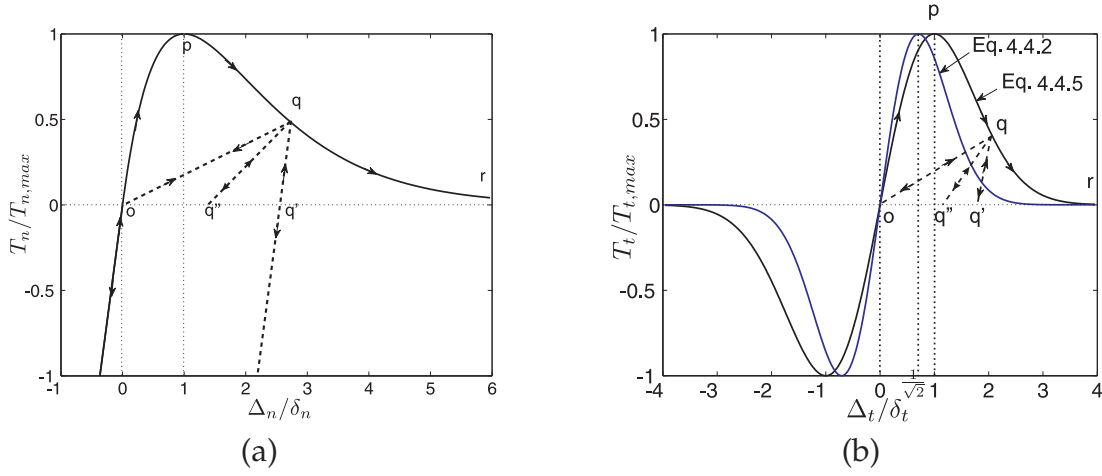


**Figure 4.6:** (a) Normal traction-separation law as given by Eq. 4.31. (b) Tangential traction-separation law as given by Eq. 4.32 and after reformulation as given by Eq. 4.35.

4.32 is reformulated such that the following equations are satisfied:

$$\left[ \frac{\partial T_t}{\partial \Delta_t} \right]_{\Delta_t=\delta_t} = 0, \quad \int_0^{\infty} T_t d\Delta_t = \phi_t. \quad (4.33)$$

Moreover, in order to maintain the original shape of the normal traction-separation curve, the coupling term in Eq. 4.31 is adapted as well. This yields the following corrected traction-separation equations for  $T_n$  and  $T_t$ :

$$T_n = \frac{\phi_n}{\delta_n} \left( \frac{\Delta_n}{\delta_n} \right) \exp \left( -\frac{\Delta_n}{\delta_n} \right) \exp \left( -\frac{\Delta_t^2}{2\delta_t^2} \right), \quad (4.34)$$

$$T_t = \frac{\phi_t}{\delta_t} \left( \frac{\Delta_t}{\delta_t} \right) \exp \left( -\frac{\Delta_t^2}{2\delta_t^2} \right) \exp \left( -\frac{\Delta_n}{\delta_n} \right) \left( 1 + \frac{\Delta_n}{\delta_n} \right). \quad (4.35)$$

Rewriting the traction-separation equations of improved Xu-Needleman CZ model (Eqs. 4.34 and 4.35) according to generalized form given Eqs. 4.1 and 4.2 yields:

$$T_n = F_n(\Delta_n)F_t^c(\Delta_t); \quad T_t = F_t(\Delta_t)F_n^c(\Delta_n), \quad (4.36)$$

where functions  $F_n$ ,  $F_t^c$ ,  $F_t$  and  $F_n^c$  can be expressed as below:

$$F_n(\Delta_n) = \frac{\phi_n}{\delta_n} \left( \frac{\Delta_n}{\delta_n} \right) \exp \left( -\frac{\Delta_n}{\delta_n} \right); \quad F_t^c(\Delta_t) = \exp \left( -\frac{\Delta_t^2}{2\delta_t^2} \right); \quad (4.37)$$

and

$$F_t(\Delta_t) = \frac{\phi_t}{\delta_t} \left( \frac{\Delta_t}{\delta_t} \right) \exp \left( -\frac{\Delta_t^2}{2\delta_t^2} \right); F_n^c(\Delta_n) = \exp \left( -\frac{\Delta_n}{\delta_n} \right) \left( 1 + \frac{\Delta_n}{\delta_n} \right). \quad (4.38)$$

In the following, Eqs. 4.34 and 4.35 will be used and extended with irreversible behavior upon unloading.

#### 4.4.2 Improved Xu-Needleman model with combined plasticity-damage unloading

##### Full damage

For full damage behavior of the improved Xu-Needleman CZ law, the damage parameters defined in Eq. 4.7 for the normal traction-separation law (Eq. 4.5) can be written as,

$$d_n = 1 - \exp \left( -\frac{\Delta_{n,max}}{\delta_n} \right); \quad d_{c,t} = 1 - \exp \left( -\frac{\Delta_{t,max}^2}{2\delta_t^2} \right). \quad (4.39)$$

Similarly, the damage parameters defined in Eq. 4.9 for the tangential traction-separation law (Eq. 4.8) are given by,

$$d_t = 1 - \exp \left( -\frac{\Delta_{t,max}^2}{2\delta_t^2} \right); \quad d_{c,n} = 1 - \exp \left( -\frac{\Delta_{n,max}}{\delta_n} \right) \left( 1 + \frac{\Delta_{n,max}}{\delta_n} \right). \quad (4.40)$$

The initial stiffness of the improved Xu-Needleman exponential cohesive zone in normal and tangential directions are obtained using Eqs. 4.3 and 4.4:

$$K_n^o = \frac{\phi_n}{\delta_n^2}, \quad (4.41)$$

$$K_t^o = \frac{\phi_t}{\delta_t^2}. \quad (4.42)$$

##### Full Plasticity

In the plasticity formulation of the improved Xu-Needleman exponential CZ law, the normal yield traction is given by:

$$T_{n,y} = \frac{\phi_n}{\delta_n} \left( \frac{\Delta_{n,eff}}{\delta_n} \right) \exp \left( -\frac{\Delta_{n,eff}}{\delta_n} \right) (1 - d_{c,t}), \quad (4.43)$$

whereas the initial normal stiffness  $K_{nn}^o$  present in the elastic normal stiffness  $K_{nn}^e$ , which is used to obtain the normal traction with Eq. 4.15, is given by Eq. 4.41.

Similar to normal yielding, the tangential yield traction can be written as:

$$T_{t,y} = \frac{\phi_t}{\delta_t} \left( \frac{\Delta_{t,eff}}{\delta_t} \right) \exp \left( -\frac{\Delta_{t,eff}^2}{2\delta_t^2} \right) (1 - d_{c,n}), \quad (4.44)$$

and the initial tangential stiffness  $K_{tt}^o$  present in the tangential elastic stiffness  $K_{tt}^e$ , which is used to obtain the tangential traction according to Eq. 4.21, is stated in Eq. 4.42.

### Combined plasticity-damage

The damage parameters  $d_n$  and  $d_t$  of the normal (Eq. 4.25) and tangential (4.26) traction-separation laws of the combined plasticity-damage formulation, respectively, for the improved Xu-Needleman exponential CZ law are:

$$d_n = 1 - \frac{\Delta_{n,eff} \exp \left( -\frac{\Delta_{n,eff}}{\delta_n} \right)}{\Delta_{n,eff} - \delta_{n,pl}}; \quad (4.45)$$

$$d_t = 1 - \frac{\Delta_{t,eff} \exp \left( -\frac{\Delta_{t,eff}^2}{2\delta_t^2} \right)}{\Delta_{t,eff} - \delta_{t,pl}}. \quad (4.46)$$

## 4.5 Model application: Computational case study

In this section, the usefulness of the proposed combined plasticity-damage unloading to simulate the experimentally observed global unloading-reloading behavior is illustrated. Subsequently, the influence of the model parameters on the global load-displacement response is discussed. To this end, delamination experiments at mode I and mixed mode loading are simulated by employing the improved Xu-Needleman exponential CZ law extended with the combined plasticity-damage unloading behavior. Purposefully, an interface system with no plasticity in the layers of the sample structure has been chosen because the separation of structural plasticity contributions to the total energy dissipation requires a dedicated numerical-experimental methodology which is beyond the scope of the current work and is discussed in the next Chapter. Therefore, the glue interface between two spring steel layers introduced in Section 4.1, has been chosen as a model system in this study because the spring steel layers show no structural plasticity. In this case, the effects of damage and plasticity mechanisms within the FPZ can directly be related to the unloading-reloading behavior of the global load-displacement response.

The model described in Section 4.4.2 was implemented in the software package MSC.Marc as an user element to model the required interface behavior. A return mapping solution procedure was employed for the case of the plasticity formulation. A 2D finite element model of the glue interface sample (with spring steel layers)



including the full geometry of the setup (see Fig. 4.7) has been made in order to simulate the boundary conditions applied in the experiment. Four-node quadrilateral elements were used to model the bulk layers of the sample and the full geometry of the setup. Simulations were performed by assuming a plane strain condition. A linear elastic material behavior (as given in Table 4.1) was used to model the spring steel layers and the experimental setup because the maximum stresses observed at the maximum applied load are well below the yield strength of the spring steel and the titanium alloy of the setup. Frictionless contact conditions were used between the two surfaces of the cracked regions of the specimen. The mesh was selectively refined at the interface such that about 100 interface elements are spanning along the length of the process zone to avoid convergence problems due to numerical instability and mesh size dependency of the final results.

**Table 4.1:** Material properties of the experimental setup and sample layers.

	Ti-6Al-4V (setup)	Spring steel (sample layers)
Young's modulus (GPa)	113.8	210
Poisson's ratio	0.342	0.33
Yield stress (MPa)	880	1100

Global load-displacement curves simulated for mode I and mixed mode loads<sup>1</sup> are shown in Fig. 4.8. The measured values of the CERR for mode I and mode II (Fig. 4.1(d)) are used for the parameters  $\phi_n$  and  $\phi_t$  in the simulations. The shapes of the simulated curves shown in Fig. 4.8 captured the observed trends in the experimental global load-displacement response depicted in Fig. 4.1(a) and 4.1(b). Mode I curves simulated at different  $\delta_{n,pl}$  are shown in Fig. 4.8(a). It is clear from this figure that in case of full damage behavior ( $\delta_{n,pl} = 0$ ), i.e. no retained opening after complete unloading, is observed after unloading to zero load, as expected. But in cases where  $\delta_{n,pl} \neq 0$ , some retained opening is seen after unloading to zero (global) load. Since in these simulations the spring steel layers are modeled as fully elastic, any resultant (global) retained opening after complete unloading is the result of a plastically/permanently deformed CZ. It is noted that the plastically deformed CZ retains all the plastic strain even after complete fracture of the interface which results in a wedge effect in the crack wake during unloading leading to a finite global retained opening after complete unloading. Therefore, the resultant permanent deformation of the interface after complete global unloading can be modeled by adapting the global retained opening (which can be measured experimentally) by changing the parameter  $\delta_{pl}$ . The resultant permanent deformation of the interface (assuming no structural plasticity) directly depends on the specific (microscopic) fracture mechanisms (e.g. de-adhesion, cleavage failure, crack bridging, grain bridging, fibre

---

<sup>1</sup>Pure mode II simulations are not shown because snap back events during delamination require a different solution procedure such as the arc length method, an extremely fine mesh, or a mesh with enhanced interface elements [117].

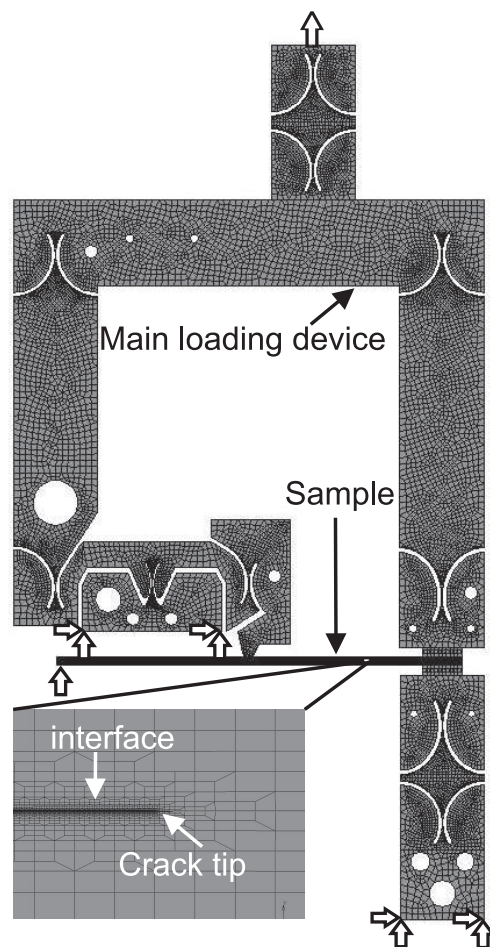


**Figure 4.7:** Finite element model of the full geometry of the miniature mixed mode bending setup [93, 107] with the sample and the applied boundary conditions. Details of mesh refinement at the interface are shown in the magnified view.

pull out, micro-void coalescence, fibrillation, crack meandering) within the FPZ. This means that the combined plasticity-damage unloading formulation is able to model the irreversible unloading behavior of the interface, originating from the fracture mechanisms within FPZ at the interface.

From Fig. 4.8(a) it can be seen that the larger part of this retained opening is observed in the first loading-unloading cycle when unloading after the maximum in the load. This is also a feature that was observed in experiments (e.g. Fig. 4.1(b)). The first loading-unloading cycle is different from the others because this cycle includes the crack initiation regime in which the process zone at the crack front develops, whereas in the subsequent cycles steady state crack growth occurs and the (fully developed) process zone remains in good approximation constant. For a plastically deforming interface, the initiation energy is much larger than that of a fully damaging interface (for example area  $OPQ > area OPO$ ). Since the parameter fracture toughness (or

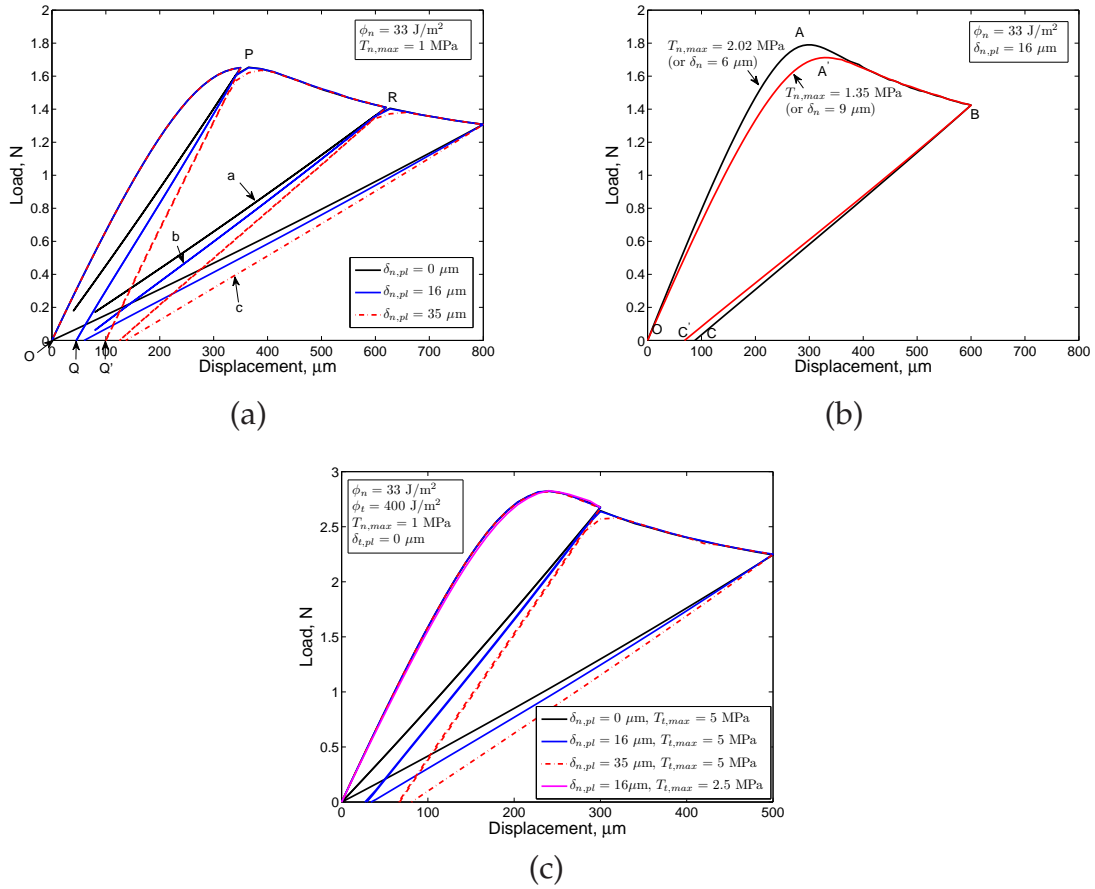


**Figure 4.8:** Global load-displacement response of mode I and mixed mode delamination simulations using the combined plasticity-damage cohesive zone interface model. (a) Influence of plastic limit on unloading-reloading behavior in mode I test. (b) Influence of  $T_{n,max}$  on the mode I response. (c) Results of mixed mode simulations (at a nominal mode angle of  $\psi = 20^\circ$  obtained from Fig. 3.12, where the relation between the relative loading position and the mode angle was established) for different  $\delta_{n,pl}$  and  $T_{t,max}$  values.

CERR) is defined as the energy needed to propagate an existing crack over a unit new surface area under the condition of stable crack growth, the measurement of CERR should exclude any energy that is spent for crack initiation. Hence, the first experimental loading-unloading cycle should be ignored for fracture toughness calculations in order to have an accurate measurement of the CERR values.

Figure 4.8(b) shows the influence of  $T_{n,max}$  (or equivalently  $\delta_n$ ) on the observed retained opening for a given value of  $\delta_{n,pl}$  for the mode I load-displacement curves. It is seen that the value of  $T_{n,max}$  not only influences the initial loading response but also affects the retained opening ( $C'$  versus  $C$ ) for a given value of  $\delta_{n,pl}$ .

Similar to the mode I case, the increase in retained opening during the first loading-unloading cycle in a mixed mode test (Fig. 4.8(c)) is larger than that during later

cycles due to crack initiation effects. The retained opening during the first cycle also increases with increasing  $\delta_{n,pl}$ . Variation of  $\delta_{t,pl}$  shows a negligible contribution to the observed retained opening in the mixed mode simulation and is therefore not shown in Fig. 4.8(c). This might be due to the continuation of degradation of shear traction during reversed loading (as shown in Fig. 4.4(b), during global unloading local degradation continues along path a'b' thereby further reducing the local tractions). Such an interface plasticity mechanism is also expected in reality for the case of friction between two contact surfaces, where local deformation of contact asperities during global unloading may cause local degradation of adhesion strength in the shear direction.

In all, it can be concluded that the proposed combined plasticity-damage description can be successfully used to extend an existing cohesive zone interface loading model with an irreversible loading-unloading behavior. This allows to model the (experimentally observed) unloading response resulting from the fracture mechanisms within the fracture process zone with only two additional parameters ( $\delta_{n,pl}$  and  $\delta_{t,pl}$ ).

## 4.6 Extraction of cohesive zone parameters

One of the important features of the new combined plasticity-damage unloading model is its simplicity. As already mentioned in previous sections, the proposed interface model not only can simulate the complex unloading-reloading behavior observed in experiments but also allows for the experimental characterization of these model parameters. A procedure to extract (all) the model parameters for the case of the improved Xu-Needleman exponential CZ law extended with the combined plasticity-damage unloading model is shown in this section.

One approach to determine the model parameters is to fit the simulated global load-displacement response to the experimental load-displacement curve. Although this approach may perhaps be sufficient to determine the plastic limit,  $\delta_{pl}$ , by matching the retained opening after unloading, Figs. 4.8(b) and 4.8(c) show that accurate determination of  $T_{n,max}$  (or  $\delta_n$ ) and especially  $T_{t,max}$  (or  $\delta_t$ ) from only the global load-displacement data is not possible. Hence, a detailed measurement of local data during delamination is necessary to gain information on the shape of the cohesive zone, or in the present case, to obtain the values of  $\delta_n$  and  $\delta_t$ .

Several local approaches that have been reported in the literature [97, 118] use the balance of energetic forces to extract the full cohesive zone law using the local data from a delamination experiment. Sørensen and Jacobsen's approach [118] allows a direct determination of mixed mode cohesive laws. However, this approach requires the delamination experiments to be carried out by loading with pure bending moments, a condition that is generally not satisfied for most delamination experiments presented in the literature. Therefore, their approach is not employed for the current study. Andersson and Stigh's approach [97] requires measurement of the applied force instead of bending moment, however, it is only suitable to determine

mode I cohesive zone parameters. Hence, in the current study, a hybrid approach is proposed to determine all model parameters of the mixed mode cohesive zone law. First, Andersson and Stigh's approach [97] is used to extract mode I parameters ( $\phi_n$  and  $T_{n,max}$  (or  $\delta_n$ )) of the glue interface system. Then, the mode II interface strength ( $T_{t,max}$ ) is determined using the fracture toughness values obtained from mixed mode tests performed at different mode angles spanning from mode I to mode II. Finally, the plastic limit can be determined from an analysis of strain field maps or crack opening displacement (COD) profiles obtained with digital image correlation (DIC).

#### 4.6.1 Mode I cohesive zone parameter determination

Andersson and Stigh's approach [97] to determine the full cohesive law from a mode I delamination test requires the following local information: the elongation in normal direction of the interface (glue) layer at the initial crack tip,  $\Delta_{n,exp}$ , and the rotation of the loading point,  $\theta$ . This information can be used in combination with the measured applied (force) load,  $F$ , and the sample width,  $B$ , to calculate the full interface traction-separation ( $T_{n,exp} - \Delta_{n,exp}$ ) relation using the following formula,

$$T_{n,exp} = \frac{2}{B} \frac{d(F\theta)}{d\Delta_{n,exp}}. \quad (4.47)$$

As a first step, Andersson and Stigh's approach was validated numerically by simulating a mode I delamination test (using the miniature mixed mode bending setup geometry [107], as shown in Fig. 4.7) employing a known interface cohesive model (in this case the exponential cohesive law) and by extracting the cohesive zone law with Andersson and Stigh's approach on the values of  $\Delta_{n,cracktip}$ ,  $\theta$  and  $F$  from simulations. A fair agreement between the input model and the measured cohesive law is observed, as shown in Fig. 4.9(a). Hence, this approach is used to extract the mode I parameters of the glue interface system. To this end, an *in-situ* delamination test was performed with the miniature mixed mode bending apparatus mounted in a micro-tensile stage. More details about the experimental methodology can be found in Refs. [93, 107]. The applied global load,  $F$ , is measured directly using the load cell in the micro-tensile stage. Images recorded during *in-situ* tests have been used for digital image correlation analysis to extract the crack opening displacement fields. The opening of the interface at the initial crack tip,  $\Delta_{n,exp}$ , and rotation of the loading point,  $\theta$ , have been obtained directly from the displacement field measured with DIC. A 5th order polynomial fit (with  $R^2 = 0.9996$ ) to the experimentally measured  $F\theta$  versus  $\Delta_{n,exp}$  data, as shown in the inset of Fig. 4.9(b), has been used to obtain the derivative,  $\frac{d(F\theta)}{d\Delta_{n,exp}}$ , in Eq. 4.47. Using this information, the traction-separation law is calculated and plotted in Fig. 4.9(b). The observed shape of the cohesive law matches well with the adopted (improved) exponential Xu-Needleman CZ law (Eq. 4.34). A fit of this CZ law to the measured cohesive law using  $\delta_n$  and  $\phi_n$  as fitting parameters is also plotted in Fig. 4.9(b). A value of  $\phi_n \approx 25 \text{ J/m}^2$  is obtained from this fit, which is in fair agreement with the value of  $\phi_n \approx 40 \text{ J/m}^2$  obtained from CERR values de-

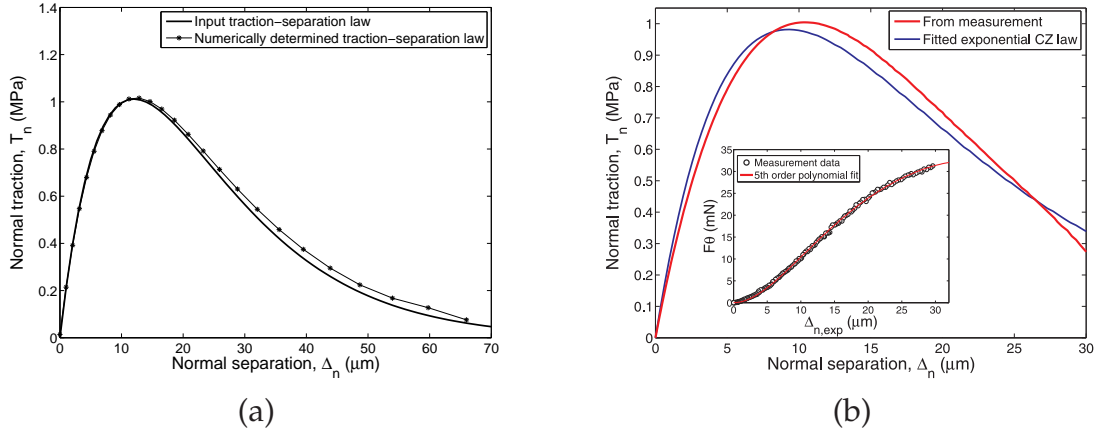


**Figure 4.9:** (a) Validation of Andersson and Stigh’s approach. The input traction-separation law used for simulating a mode I test is compared with the traction-separation law determined from the simulated result using Andersson and Stigh’s approach. (b) Mode I traction-separation law of the glue interface system experimentally determined using Andersson and Stigh’s approach (red line), shown together with the best-fit exponential CZ law (Eq. 4.34) using  $\delta_n$  and  $\phi_n$  as fitting parameters while taking  $\Delta_t = 0$  (blue line). The inset shows the experimental  $F\theta$  data as a function of opening of the interface at the crack tip,  $\Delta_{n,exp}$  fitted with a 5th order polynomial with an  $R^2$  value of 0.9996.

terminated from the global load-displacement curves (Fig. 4.1(d)), taking into account the uncertainties of both procedures. The measurement uncertainty in this (Andersson and Stigh’s) approach mainly originates from: (i) the error in identification of the initial crack tip position (where  $\Delta_{n,exp}$  is measured), (ii) the resolution of the DIC analysis in measuring the correct  $\Delta_{n,exp}$  and  $\theta$  values and (iii) the pre-strain of the initial crack tip (leading to partial damage). Estimation of the latter one is difficult and it can only be minimized by reducing the pre-loading of the crack tip during creation of the precrack. For the present case, a sub-micron resolution achieved in the DIC displacements (by using a special nano-particle tracking pattern) which gives an error of  $\sim 20\text{-}30\%$  in the final CERR value, assuming negligible error contributions from the force measurements and the fitting procedure ( $F\theta$  versus  $\Delta_{n,exp}$  in Fig. 4.9(b)). Additionally, uncertainty contributions from crack tip identification and pre-stressing of the crack tip need to be added. On the other hand, for the case of the CERR determination from the global load-displacement curve, uncertainties in the measurement of the increase in crack length, force and displacement contribute to the final uncertainty in the CERR, which is  $\sim 10\%$  for the present case. The fit to the experimentally obtained traction-separation curve in Fig. 4.9(b) also yields  $\delta_n \approx 9\ \mu\text{m}$ , from which  $T_{n,max} \approx 1\ \text{MPa}$  is obtained (with Eq. 4.34) which will be used in the determination of the mode II cohesive parameters, as discussed in the next section.

## 4.6.2 Mode II parameter determination

The mode II fracture toughness ( $\phi_t$ ) can be directly obtained from the mode II delamination test (Fig. 4.1(d)). Identification of the mode II interface strength ( $T_{t,max}$ ) is performed by using a known dependency of the fracture toughness (or CERR) with the mode angle. The fracture toughness values as a function of loading mode for the glue interface system (Fig. 4.1(d)) were used for this analysis. For the interface model currently used in this study, the total work of separation,  $\omega_{tot}$ , for the complete separation of the interface is given by:

$$\omega_{tot}(\psi) = \int_0^\infty T_n(\Delta_n, \Delta_t) d\Delta_n + \int_0^\infty T_t(\Delta_n, \Delta_t) d\Delta_t, \quad (4.48)$$

where,  $T_n(\Delta_n, \Delta_t)$  and  $T_t(\Delta_n, \Delta_t)$  are given by Eqs. 4.34 and 4.35 respectively, and the mode angle,  $\psi = \arctan\left(\frac{\Delta_t}{\Delta_n}\right)$ , is the separation angle with respect to the interface normal.  $\omega_{tot}$  is plotted in Fig. 4.10 as a function of constant mode angle,  $\psi$ , at different values of  $\gamma = \frac{T_{t,max}}{T_{n,max}}$ . The value of  $\gamma \approx 5$  is obtained by fitting Eq. 4.48 to the

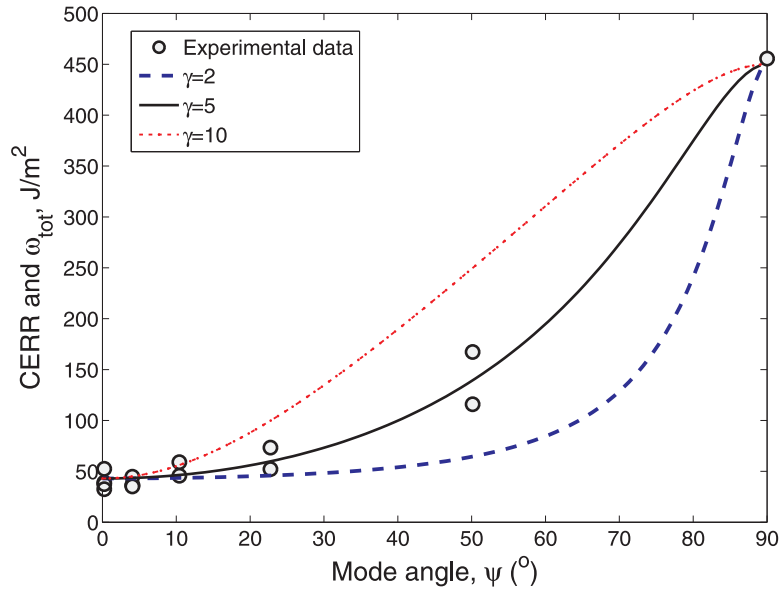


**Figure 4.10:** Experimentally measured critical energy release rate (from Fig. 4.1(d)) and the total work of separation of the cohesive zone model,  $\omega_{tot}$ , calculated using Eq. 4.48, as a function of the mode angle,  $\psi$  for different values of  $\gamma = \frac{T_{t,max}}{T_{n,max}}$ .

experimental fracture toughness versus mode angle results. With this information the value  $T_{t,max} \approx 5$  MPa can be directly obtained using the previously determined  $T_{n,max} \approx 1$  MPa for this specific interface. It is noted that in this approach the model results ( $\omega_{tot}$ ) for opening at a constant mode angle are compared with experimental

CERR results for which the nominal mode angle is determined based on FE simulations of the experiments, as shown in [93]. In order to identify a unique set of parameters in this approach, the mode angle needs to be constant with increase in crack length. This has been checked and a maximum change in the mode angle of  $\sim 5^\circ$  is identified for the present case in simulations of the experiment with a cohesive zone model.

### 4.6.3 Determination of the plastic limit

The plastic limit is the key parameter that determines the unloading response of the CZ from damage to plasticity (see Fig. 4.4(d)), while it also determines the shape of the opened interface after unloading. The value of the plastic limit may be obtained from a DIC analysis of unloading experiments. To this end, numerical mode I simulation of an unloading experiment will be used to determine how the plastic limit can be extracted from COD profiles. Figure 4.11(a) shows the unloading COD

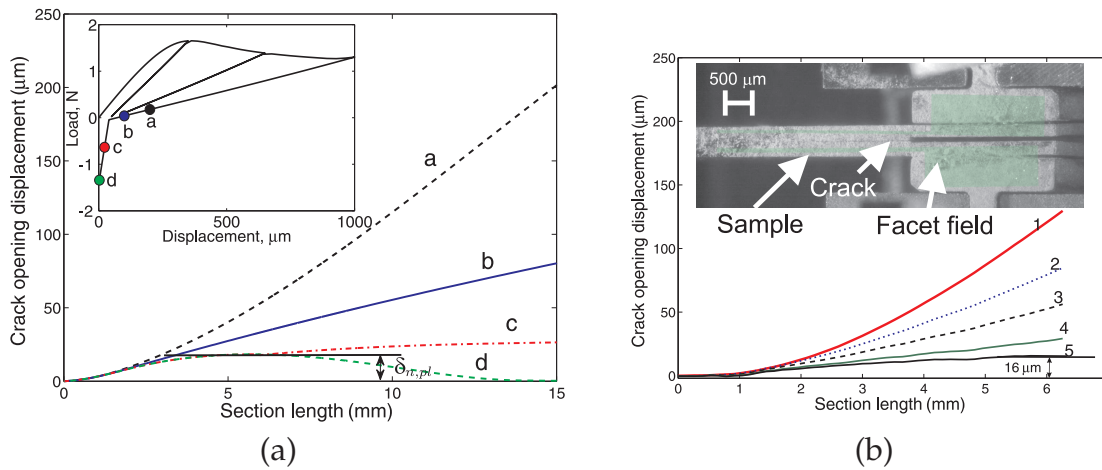


**Figure 4.11:** (a) Unloading crack opening displacement profiles obtained from a mode I simulation using  $\delta_{n,pl} = 16 \mu\text{m}$  as an input parameter. The inset shows the simulated load-displacement response where the corresponding global displacements of the COD profiles are marked (a,b,c and d). (b) Experimentally obtained unloading COD profiles close to zero load showing the plateau with a value of  $\delta_{n,pl} = 16 \mu\text{m}$ . The inset shows a micrograph of the edge of the sample (on the pre-cracked side) with the DIC facet overlay in green.

profiles obtained at different global displacements of a mode I simulation. After unloading just below zero load, a plateau in the COD profile can be seen (curve c) as shown in Fig. 4.11(a). Further unloading into the compressive regime leaves a retained opening in the COD profile which corresponds closely to the input value of the plastic limit,  $\delta_{n,pl}$ . This can be understood because reducing the separation locally below the plastic limit results in high local compressive stresses that prevent further



closure. It was identified that the value of the plastic limit determined in this way is independent of the crack length. Using this procedure, the normal plastic limit of the glue interface is determined experimentally. Figure 4.11(b) shows the measured COD profiles at different global displacements obtained from DIC of *in-situ* SEM images of a mode I delamination experiment. Note that the employed experimental setup does not allow to continue loading into the compressive regime of a mode I experiment during unloading. Hence, the experiment was stopped just below the zero load. Similar to the simulation results in Fig. 4.11(a), a plateau was observed in the measured COD at zero load (curve 5) as shown in Fig. 4.11(b). The retained opening displacement, corresponding to this plateau is obtained as the value of  $\delta_{n,pl}$  and was found to be  $\sim 16 \mu\text{m}$  for the glue interface. Although the global force-displacement response and the local traction are less sensitive to the value of  $\delta_{t,pl}$  (Section 4.5),  $\delta_{t,pl}$  may be obtained in a similar way as  $\delta_{n,pl}$ , by extracting from COD profiles or strain maps measured under mode II delamination.

Finally, the simulated load-displacement response at mode I loading with the parameters as determined in this section ( $\phi_n \approx 33 \text{ J/m}^2$  which is taken as the average of  $25 \text{ J/m}^2$  and  $40 \text{ J/m}^2$ ;  $T_{n,max} \approx 1 \text{ MPa}$ ; and  $\delta_{n,pl} \approx 16 \mu\text{m}$ ) was already shown as curve b in Fig 4.8(a). By comparing the simulated curve with the experimental mode I load-displacement graph shown in Fig. 4.1(b), it can be concluded that a fair agreement is observed between the two curves in the crack growth regime. The observed deviation in the crack growth regime can be due to measurement inaccuracies, statistical uncertainties, possible errors involved in CZ parameter extraction procedure and inaccuracies due to the choice of the CZ law. The prediction can certainly be improved by reducing the statistical uncertainty in the  $\phi_n$  and  $\phi_t$  measurements (with more experiments) to get more accurate CZ parameters. It is noted here, however, that the focus of this paper is not on exactly predicting the experimental load-displacement response, but on presenting a damage-plasticity unloading model and illustrating the capability of this model to simulate the experimentally measured unloading response. The relatively a small number of experiments presented here suffice for this purpose. Note also that the global retained opening observed after complete unloading (from  $\approx 600 \mu\text{m}$  opening displacement) is in good agreement between both cases taking into account the measurement uncertainties. The deviation seen in the initial portion of the measured experimental response can be attributed to several factors such as sharpness of the crack, any pre-loading experienced by the crack tip before actual loading, and unavoidable defects and inhomogeneities present at the interface. The presence of a finite plastic limit (of  $\sim 16 \mu\text{m}$ ) indicates that the fracture at the glue interface involves both damage and plasticity mechanisms, and, therefore, a combined plasticity-damage model indeed needed to model this behavior.

## 4.7 Conclusions

The presence of combined damage and plasticity mechanisms at the interface is commonly observed in delamination experiments. Therefore, an interface model that can

capture the irreversible unloading-reloading response is needed for predictive finite element models, e.g., to predict crack branching and crack propagation in multiple interfaces. To this end, this article introduced a new combined plasticity-damage unloading description that can be used to extend existing cohesive zone (loading) models with an irreversible unloading-reloading behavior suitable for mixed mode loading conditions. Important features of the proposed model include the ability to (i) extend (most of) the existing mixed-mode CZ models with and without coupling, and (ii) simulate irreversible behavior ranging from full damage to full plasticity while (iii) the model is relatively simple containing only two new parameters ( $\delta_{n,pl}$  and  $\delta_{t,pl}$ ) that can be determined experimentally. Case study simulations showed the capability of the model to simulate the trends in the experimentally observed unloading behavior that results from irreversible fracture mechanisms at the interface. Finally, it was shown that all the model parameters can be determined from dedicated *in-situ* delamination experiments combined with a digital image correlation analysis of crack opening displacement (COD) profiles. Specifically, a procedure to obtain the plastic limit(s) from COD profiles measured with DIC was developed by analyzing numerical simulations and successfully applied experimentally.



# A semi-analytical approach for the separation of interfacial toughness and structural plastic dissipation in a delamination experiment<sup>1</sup>

---

### Abstract

Interfacial delamination is a key reliability challenge in composites and micro-electronic systems due to (high density) integration of dissimilar materials. Predictive finite element models are generally used for the design of these materials and systems to minimize delamination failures. Successful quantitative predictions require the input of interface properties that have to be determined accurately from dedicated delamination experiments. Among all relevant interfacial properties, the interface fracture toughness is perhaps the key parameter which is usually determined from the area under the load-displacement curve. For this purpose, an interface delamination growth experiment with a constant process zone is commonly used, relying on the assumption that there is no permanent deformation in the layers of the sample structure. Much evidence in the literature exists confirming that plasticity often does occur in the sample structure, particularly, if the layers forming the sample structure are ductile and the interface is strong. The plastic dissipation in the sample structure should be adequately subtracted from the total steady state work of separation (during a delamination experiment) to obtain the true value of the interface fracture toughness (independent of the thickness of the two sample arms form-

---

<sup>1</sup>*Reproduced from:* M. Kolluri, J.P.M. Hoefnagels, J.A.W. van Dommelen, M.G.D. Geers, A semi-analytical approach for the separation of interfacial toughness and the structural plastic dissipation in a delamination experiment, to be submitted (2011).

ing the sample structure). Hence, a proper experimental analysis method is required that can separate structural plastic dissipation of sample layers, using standard experimental delamination set-ups. In contrast to existing approaches that require either complex numerical simulations or analytical solutions, this paper presents a semi-analytical and easy-to-implement approach that is applicable to most existing mode I experimental techniques that apply loads (instead of moments) to trigger delamination. The procedure does not require knowledge of the constitutive behavior of the adherent layers to separate structural plastic dissipation from interface fracture toughness. The proposed approach is numerically verified and experimentally assessed, where it is shown that applying this approach can lead to a correction of the interface fracture toughness of more than a factor of two, demonstrating the significance of correcting errors induced by plastic deformation of the structural arms of a sample during a delamination experiment.

## 5.1 Introduction

Interfacial delamination is a key reliability issue in (laminate) composites [6, 7, 119] and micro-electronic systems [3, 4], where (high density) integration of dissimilar materials is required to achieve superior mechanical, physical and functional properties. As a consequence, identification of interfaces which are prone to delamination is important for the design and optimization of these systems. Hence, predictive models that can accurately capture the failure mechanisms of the interfaces are required for adequate design of these products. These models rely on a detailed characterization of the interface properties with an understanding of failure mechanics from dedicated experiments. Among all relevant interface properties, the interface fracture toughness, representing the amount of energy per unit area that is absorbed by the interface upon fracture, is perhaps the key parameter for modeling these interfaces. In case of delamination between perfectly brittle materials, this fracture energy is approximately equal to the surface energy (that is needed for the creation of new surfaces). On the other hand, for interfaces between deformable materials, the formation of the new surfaces often also triggers dissipative mechanisms, such as damage and plasticity, in the adjoining materials in the immediate vicinity of the interface, identified as the fracture process zone as shown in Fig. 5.1. Therefore, the surface energy and the energy spent for the fracture processes within the fracture process zone together contribute to the interface fracture toughness. However, the measured value of the interface fracture toughness, which is the characteristic property of the interface, should be independent of the geometry of the adjoining material layers.

Traditionally, linear elastic fracture mechanics (LEFM) based techniques [22, 67, 89, 113, 120] are employed to experimentally characterize interface fracture toughness. In this approach, the determination of interface fracture toughness requires (i) the measurement of the critical load or moment at which the interface delaminates, starting from an initial precrack (with known length), (ii) the analytical energy release rate for the considered specimen geometry and loading configuration, derived from

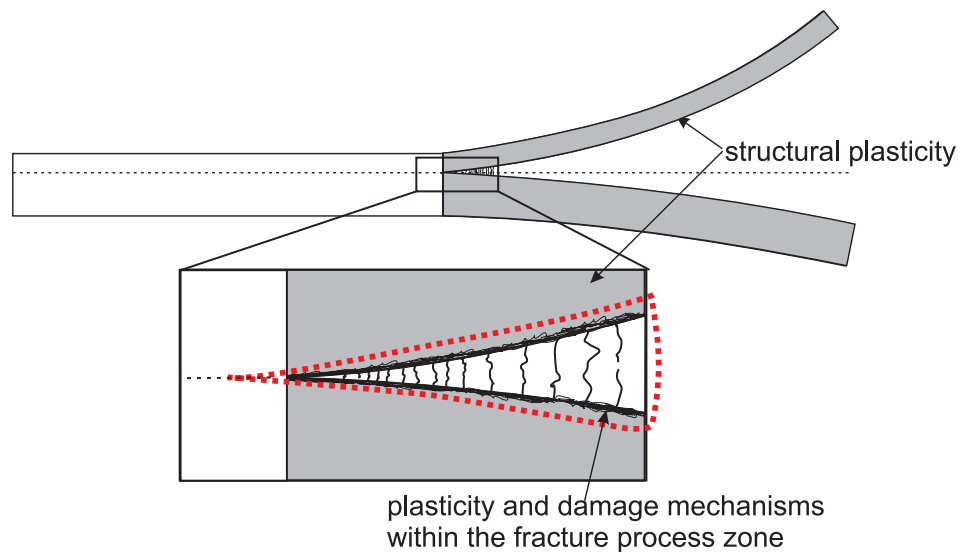


**Figure 5.1:** Schematic diagram of the fully unloaded interface sample illustrating the damage and plasticity mechanisms within the fracture process zone (dashed envelope) at the interface and permanent deformation in the structural layers of the sample (structural plasticity).

LEFM principles, and (iii) the material properties of the adherent layers. This class of experiments is widely used in the literature for interface fracture toughness analysis because of their standardization and relative ease to exploit experimental data. However, it is important to note the issues and the underlying assumptions that limit the applicability of this widely used approach for interface fracture toughness measurement:

- Experimental inaccuracies in the measurement of the critical load of delamination can be significantly influenced by the condition of the precrack.
- Obtaining closed form analytical solutions for the determination of the energy release rate, particularly by incorporating the influence of transverse shear load [78], is difficult for dissimilar material interface structures in mixed mode loading cases.
- This approach intrinsically assumes that the fracture process zone (involving irreversible mechanisms like damage, plasticity and fracture at the interface) is very small. The approach also assumes that the supplied energy to trigger delamination growth is stored elastically in the structure without any permanent deformation of the layers.

Delamination growth experiments [25, 93, 107] resolve some of the above mentioned difficulties and are able to characterize the interface fracture toughness of interface structures with any (small or large) size of the fracture process zone. In these experiments, the full load versus displacement response is recorded during initiation

and propagation of delamination starting from an initial precrack. A schematic load-displacement diagram illustrating the initiation and propagation regimes is shown in Fig. 5.2(a). Once the process zone is fully developed (i.e. after the crack initiation regime), the local crack opening geometry within the process zone remains constant with increasing crack length, and therefore, the developed process zone moves along the interface upon further loading (i.e. in the propagation regime). The interface fracture toughness is simply calculated from the energy needed to propagate a fully developed crack per unit of delaminated area, i.e. the energy spent in one loading-unloading cycle (hashed region in Fig. 5.2(a)), divided by the sample width,  $B$ , times the crack length increase (i.e.  $\Delta a = a_2 - a_1$ ). If the delamination setup allows for *in-situ* (microscopic) visualization of the crack propagation and thus accurate determination of the crack length increase for a constant crack opening geometry (e.g. [107, 121]), then only the measurement uncertainties in force, displacement, and crack length affect the measured interface fracture toughness without contributions of any model assumptions. Without *in-situ* visualization,  $a_2 - a_1$  can still be obtained either by *ex-situ* crack length examination before and after the loading-unloading cycle. However, this increases the measurement uncertainty as the crack length is measured in a closed position. Alternatively the structural stiffness,  $K$ , of the partly delaminated specimen can be related to a crack length  $a$  (whereby the structural stiffness is estimated from beam theory analysis or finite element simulations [25]). In all cases, though, the uncertainties involved with manufacturing of the precrack and the initial development of the process zone are avoided by ignoring the crack initiation regime of the load-displacement response.

Similar to LEFM approaches, delamination growth experiments intrinsically assume that the supplied energy to trigger delamination growth is stored elastically in the structure (e.g. the delaminating layers composing the specimen structure), without any permanent deformation of the sample layers. In such a situation, without any plasticity mechanisms within the fracture process zone of the interface, the unloading curve starting at a crack length  $a$  should return to the origin (along a straight line). This behavior is indeed often observed in experiments, e.g. curve 1 in Fig. 5.2(b), showing the load-displacement response measured from a mode I delamination experiment on a coated copper lead frame (CuLF)-molding compound epoxy (MCE) interface [107]. On the other hand, in the absence of permanent structural deformation, any retained opening after complete unloading should be the result of plasticity of the material within the fracture process zone during the separation of the two materials.

In reality, however, during the delamination experiment there can be permanent deformation of the sample structure (referred as structural plasticity, see Fig. 5.1) leading to an additional energy dissipation besides the energy spent for the actual delamination process (i.e. the sum of the surface energy and dissipated energy due to the damage and the plasticity mechanisms within fracture process zone) and resulting in an additional retained opening after complete unloading. That means that the observed retained opening in curve 2 of Fig. 5.2(b) (measured for a similar sample as for curve 1 but without interface coating) might originate from either plasticity mecha-

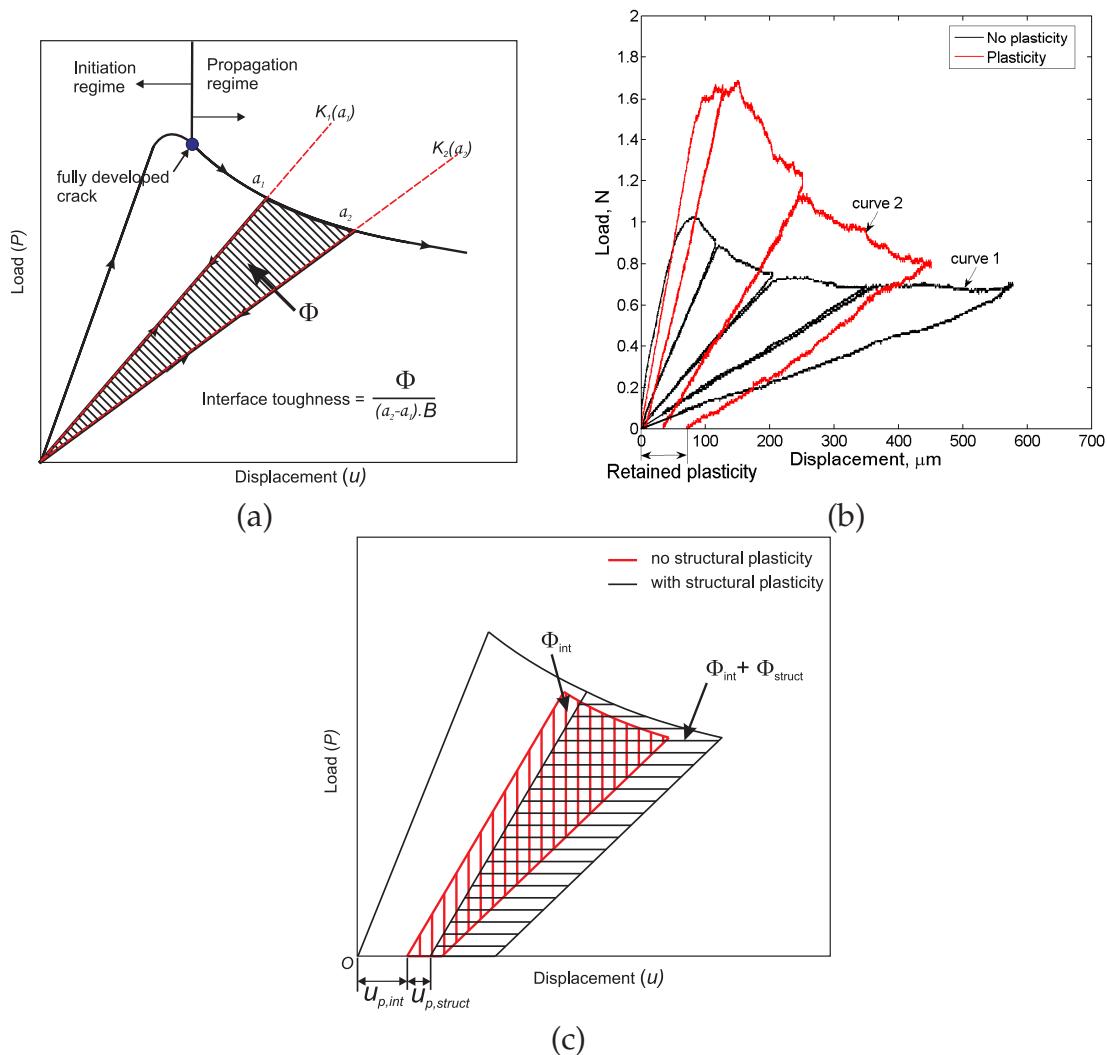


**Figure 5.2:** Illustration of delamination growth experiments. (a) Schematic plot illustrating how the interface fracture toughness is obtained either from the energy spent in one loading-delamination-unloading cycle (hashed area) with known increase in crack length or with estimated stiffness lines for chosen crack lengths. (b) Experimental load-displacement curves exhibiting no plasticity (curve 1) after unloading and significant (retained) plasticity (curve 2) after unloading [107]. (c) A schematic load-displacement response curve of an interface system that has plasticity mechanisms within the fracture process zone at the interface, and shows structural plasticity as well. Consequently, resultant retained opening is due to plasticity within the fracture process zone at the interface ( $u_{p,\text{int}}$ ) and due to the permanent deformation of the sample structure ( $u_{p,\text{struct}}$ ). The hashed regions indicate the total dissipated energy during one loading-delamination-unloading cycle in cases of with and without structural plasticity.



nisms within the fracture process zone at the interface or from structural plasticity of the sample layers or from both. Fig. 5.2(c) shows a schematic load-displacement response of an interface system that exhibits plasticity mechanisms within the fracture process zone at the interface, as well as structural plasticity. This figure illustrates the contributions of retained opening due to the plasticity within the fracture process zone at the interface ( $u_{p,int}$ ) and due to the permanent deformation of the sample structure ( $u_{p,struct}$ ) to the measured (total) retained opening. Only the interface fracture energy ( $\Phi_{int}$ ), which is the sum of the surface energy and the energy dissipated due to the damage and the plasticity mechanisms within the fracture process zone, should be part of the measured interface fracture toughness but not the energy that is plastically dissipated in the sample structure ( $\Phi_{struct}$ ). However, it is not known a priori whether both structural plastic dissipation and plastic dissipation within the fracture process zone are present. Therefore, the contribution of structural plasticity should be identified quantitatively and should be separated in order to obtain the correct value of interface fracture toughness.

In the literature, much emphasis was given to understand and separate the influence of structural plasticity on interface fracture toughness measurements. In the early nineties, 'first principle' predictions for mode I toughness of an interface between a homogeneous elastic-plastic solid were made by Tvergaard and Hutchinson [28]. A separation law was embedded to model the interface fracture, revealing an increase in mode I toughness due to plasticity in the sample structure. Similar studies [29–33] were performed to understand the influence of structural plasticity on the mode dependent fracture toughness of an interface between dissimilar elasto-plastic solids. All these studies predicted that plastic deformation outside of the fracture process zone leads to an increase in apparent fracture toughness. Later, Yang et al. [122] performed a numerical analysis of interface fracture in adhesively bonded beams failing with extensive plastic deformation using an embedded process zone model (EPZ) developed by Tvergaard and Hutchinson [28] and found the EPZ parameters to be independent of plasticity in the layers of the sample structure. Thouless et al. [123] presented an analytical solution for the fracture toughness of an adhesively bonded double-cantilever beam (DCB) that fails with extensive plastic deformation of the adherents. This solution is suitable for delamination experiments in which pure bending moments are applied to trigger delamination. In this analysis, the authors assumed a plastic constitutive law with power law hardening to describe the plasticity in the sample structure. All these efforts indeed indicate that the plastic dissipation in the sample structure should be separated from the total steady state work of separation (during a delamination experiment), to obtain the interface fracture toughness that is independent of the geometry of the adjoining material layers.

Most studies cited above are valuable to understand and evaluate the influence of structural plasticity on interface fracture toughness measurements, but they require either analytical solutions or numerical simulations with a representative plastic description of the adherent material layers. This does not enable a direct interpretation of data from delamination experiments to obtain the correct value of the interface fracture toughness. In contrast, the present paper presents a methodology that re-

quires neither an analytical solution or a numerical simulation nor the constitutive behavior of the adherents, to separate the energy dissipated due to permanent deformation of the sample structure from the total energy dissipated during crack growth for a mode I test. The proposed methodology is applicable to most of the existing delamination growth experiments that apply loads to trigger delamination, and it does not require *in-situ* visualization of the delamination process under a microscope.

The article is organized as follows. First, a semi-analytical approach is proposed to separate the contribution of structural plastic dissipation from the total energy spent during a delamination experiment. Then, the proposed approach is numerically verified by employing a finite element model with cohesive zone elements (at the interface). Finally, the proposed approach is experimentally assessed by characterizing the interface fracture toughness of industrially relevant copper lead frame-molding compound epoxy (CuLF-MCE) structures with different layer thicknesses.

## 5.2 Procedure to extract interface fracture toughness

In this section, the methodology for the separation of structural plastic dissipation from the measured total dissipated energy during a delamination experiment is presented, as well as the underlying assumptions. The key principle relies on the reconstruction of the fictitious force-displacement response (in the crack propagation regime) that would have been measured in the absence of structural plasticity, for which the interface fracture toughness can be determined directly (as explained in Fig. 5.2(b)). To be able to reconstruct this fictitious structural plasticity-free force-displacement curve, the following assumptions, which will be numerically verified in the next section, are made:

- (1) Plasticity in the sample structure has no influence on the structural (unloading) stiffness, for a given crack length, with or without plasticity within the fracture process zone at the interface.
- (2) For a given crack length, the critical global load required for a crack to grow with or without structural plasticity is the same (i.e. the load depends on the interface fracture resistance only).

### 5.2.1 Case 1: Structural plasticity, no plasticity in the fracture process zone at the interface

As already discussed in the previous section, the observed retained opening can originate from either plasticity mechanisms within the fracture process zone at the interface or from structural plasticity of the sample layers or from both. In the case of only structural plasticity, the procedure for reconstruction of the force-displacement that corresponds to the (fictitious) case without structural plasticity is relatively simple.

In Fig. 5.3, the black solid curve represents an experimentally measured load-displacement response during a loading-unloading experiment. Area  $ACDB$  represents the total energy ( $\Phi_{tot}$ ) dissipated during the crack growth of  $\Delta a = a_C - a_A$  between two consecutive unloadings. This total energy contains the interface fracture energy ( $\Phi_{int}$ ) and the structural plastic dissipation ( $\Phi_{struct}$ ). Using assumption 1, the unloading stiffness lines  $AB$  and  $CD$  can be translated horizontally towards the origin over the distance  $OB$  and  $OD$  (i.e.  $u_{p,struct,B}$  and  $u_{p,struct,D}$ ), respectively, in order to find the points  $A'(u_{A'}, P_A)$  and  $C'(u_{C'}, P_C)$  where  $u$  and  $P$  indicate the displacement and load, respectively. The points  $X'(u_{X'}, P_X)$  between  $A'$  and  $C'$  (the dashed curve in Fig. 5.3) can be reconstructed using the relation,  $u_{p,struct,X} = u_{p,struct,A} + \frac{u_{p,struct,C} - u_{p,struct,A}}{u_C - u_A}(u_X - u_A)$ , which represents a linear interpolation of  $u_{p,struct,X}$  between  $u_{p,struct,A}$  and  $u_{p,struct,C}$ . This results in the dashed curve, from which the interface fracture energy  $\Phi_{int}$  can be determined directly as it is equal to the area  $OA'C'$ . As explained above,  $\Phi_{int}$  divided by the increase in crack length  $\Delta a$  and the width of the sample,  $w$ , yields the interface fracture toughness. It is worth mentioning here that only  $\Delta a$  is needed (and not the absolute values of the crack lengths at the unloading points) to calculate the interface fracture toughness. This is important because identifying the exact crack tip, and finding exact crack length values for interface structures involving large process zones is cumbersome even with high magnification microscopic visualization of the delamination front. The exact crack length also depends on the definition of a crack tip. On the contrary, the value of  $\Delta a$  can be obtained relatively easily with high accuracy for a steady state moving process zone, e.g. by matching displacement fields obtained with digital image correlation (DIC).

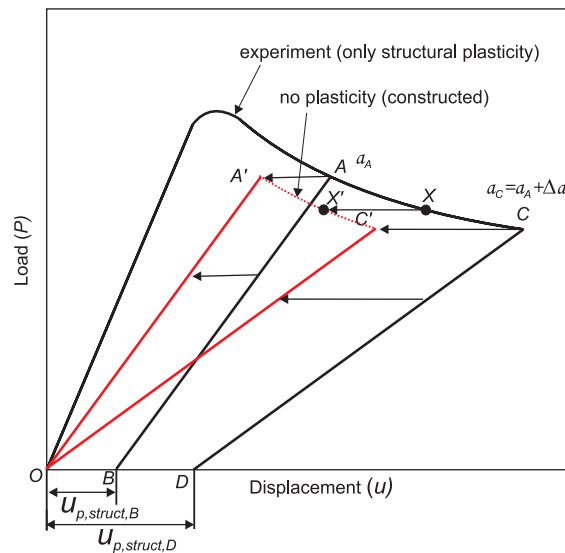


**Figure 5.3:** Schematic diagram illustrating the reconstruction of the virtual plasticity-free load-displacement response for a measurement in which only structural plasticity is present.

### 5.2.2 Case 2: Structural plasticity and plasticity within the fracture process zone at the interface

In case when both structural plasticity and plasticity within the fracture process zone at the interface, again, the total energy dissipated between two consecutive unloadings for the crack to grow by  $\Delta a$  (area  $ACDB$  in Fig. 5.4) contains the interface fracture energy ( $\Phi_{int}$ ) and the structural plastic work ( $\Phi_{struct}$ ). However, the total retained opening after complete unloading,  $u_p$ , is now the sum of the retained opening due to structural plasticity  $u_{p,struct}$  and the plasticity within the process zone  $u_{p,int}$ . In this case, the structure will exhibit a stiffer unloading response ( $CD$ ) compared to the case of only structural plasticity or no plasticity at all (Fig. 5.3). Therefore, the procedure for the separation of structural plastic dissipation and plasticity within the fracture process zone is less trivial because the measured stiffness lines can no longer be translated to the origin ( $O$ ) as done in the previous case.

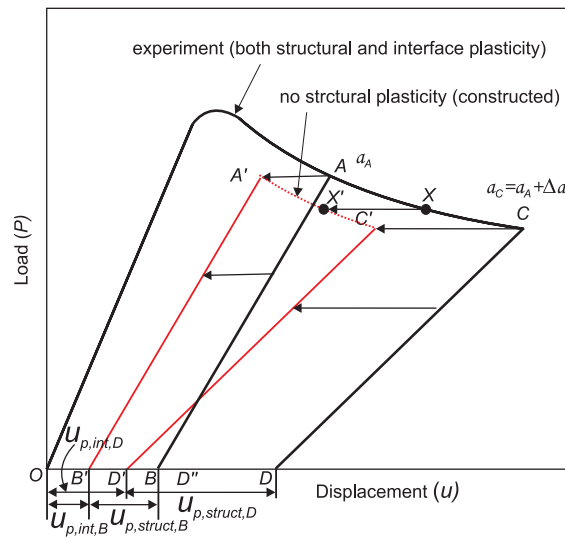


**Figure 5.4:** Schematic diagram illustrating the reconstruction of the virtual plasticity-free load-displacement response for a measurement in which both structural and interface plasticity are present.

To solve this problem, a semi-analytical approach, which relies only on experimental measurements, is proposed to separate the structural plastic dissipation  $\Phi_{struct}$  and the interface fracture energy  $\Phi_{int}$ . In this approach, first the individual contributions due to structural plasticity ( $u_{p,struct}$ ) and plasticity within the process zone at the interface ( $u_{p,int}$ ) to the total retained opening ( $u_p$ ) are identified for (at least) two unloading steps (explained below). Then, the experimental unloading stiffness lines are translated towards the origin by the corresponding retained opening due to structural plasticity,  $u_{p,struct}$  (yet to be determined). This allows to identify (in the propagation regime) the virtual force-displacement curve equivalent to the no struc-

tural plasticity case. For example in Fig. 5.4, lines  $AB$  and  $CD$  are translated by  $BB'$  and  $DD'$  (i.e.  $u_{p,struct,B}$  and  $u_{p,struct,D}$ ), respectively, to find  $A'$  and  $C'$ . The points  $X'(u_{X'}, P_x)$  between  $A'$  and  $C'$  (the dashed curve in Fig. 5.3) can be obtained using the relation,  $u_{p,struct,X} = u_{p,struct,A} + \frac{u_{p,struct,C} - u_{p,struct,A}}{u_C - u_A}(u_X - u_A)$ , as explained earlier in section 5.2.1. Then, area  $A'C'D'B'$  represents the interface fracture energy  $\Phi_{int}$  for the crack to grow from  $a_A$  to  $a_C$ , which divided by  $\Delta a$  and  $w$  gives the interface fracture toughness.

Key part of the approach is the separation of the individual contribution of structural plasticity ( $u_{p,struct}$ ) and plasticity within the process zone at the interface ( $u_{p,int}$ ) from the total retained opening ( $u_p$ ), for which the following two additional assumptions are used:

- (3) The size and shape of the process zone is constant during the crack propagation regime. That means that after the initiation regime, the fully developed crack tip simply translates during further delamination. Most delamination growth experiments intrinsically use this assumption.
- (4) Plasticity in the sample structure develops only in the region surrounding the process zone since the stresses in the layers are the highest there. This means that the plastic curvature at a certain position does not change anymore after the process zone has passed by.

The procedure for obtaining the retained opening due to structural plasticity involves the following steps. First, for each layer the retained crack opening displacement (COD) profile,  $u_n$ , (defined with respect to the undeformed interface, i.e.  $Ox_{end}$  in Fig. 5.5) of the fully unloaded sample at the end of the delamination test is determined. The retained COD profiles of both adherent bulk layers can be obtained, for example, from a recorded micrograph of the fully unloaded sample, e.g. using a digital imaging correlation (DIC) technique as shown in Section 5.4. The process zone and the region close to the process zone (referred to as region 1 in Fig. 5.5), are influenced by both plasticity in the process zone and structural plasticity, whereas the measured retained curvature in the layers in region 2 is the result of structural plasticity only. Region 3 and 4 in Fig. 5.5 represent the crack initiation and pre-crack regions, respectively. Region 2 can be fitted with a low order polynomial equation, which can be extrapolated into region 1 to identify the point  $a_c^{fit}$  on the undeformed sample axis  $Ox_{end}$ , see Fig. 5.5. The tangent of the fitted curve at  $a_c^{fit}$  extended to  $x = x_{end}$  reveals the contribution of plasticity, in the process zone  $u_{p,int}$ , (i.e.  $u_{p,int} = (x_{end} - a_c^{fit}) \left[ \frac{d(u_n^{fit}(x=a_c^{fit}))}{dx} \right]$ ) at the end of the sample, where the load was applied. Next, the contribution of structural plasticity  $u_{p,struct}$ , to the total retained opening,  $u_p$ , is recovered by  $u_{p,struct} = u_p - u_{p,int}$ . In Fig. 5.5, this procedure is illustrated for the top bulk layer. The same procedure is repeated for the bottom layer if both sample layers undergo permanent deformation during delamination. The total retained openings due to structural plasticity,  $u_{p,struct}$ , and the plasticity within the process zone  $u_{p,int}$  are obtained by adding the corresponding individual contributions from both layers.

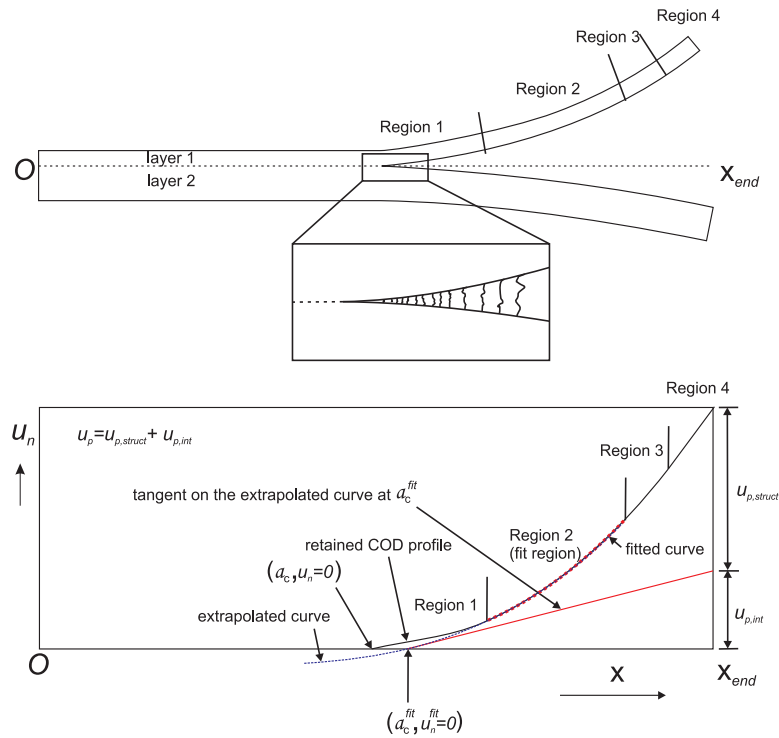


**Figure 5.5:** Schematic figure showing the fully unloaded sample (top) and the corresponding retained opening profile of the top layer (bottom) with respect to undeformed sample axis  $Ox_{end}$ . The figure also shows the four different regions of the delaminated sample, i.e. (1) the region influenced by both structural plasticity and plasticity within the fracture process zone, (2) the region where the measured retained curvature is influenced by structural plasticity only, (3) the crack initiation region and (4) the pre-cracked region. Region 2 is fitted with a low order polynomial and extrapolated into region 1 to identify the point  $u_n^{fit}(a_c^{fit}) = 0$  intersecting  $Ox$ . Separation of structural plasticity,  $u_{p,struct}$ , and the plasticity within the process zone,  $u_{p,int}$ , is obtained by constructing a tangent to the extrapolated curve at  $a_c^{fit}$ .

## 5.3 Numerical verification

In this section, first, the four assumptions made in the previous section are verified numerically using finite element simulations employing an interface cohesive zone (CZ) model that allows for modeling the irreversible unloading response that result from the combined damage and/or plasticity mechanisms within the process zone at the interface [121]. That means that all the dissipative (damage and plasticity) mechanisms within the fracture process zone are lumped into the interface behavior described with the cohesive zone model. A brief review of this CZ model is given in Section 5.3.1. After verification of the assumptions, the proposed approach to separate the structural plasticity contribution from the total energy dissipated during a

delamination experiment is verified, in order to recover the correct interface fracture toughness value.

### 5.3.1 Summary of the irreversible interface model

The combined plasticity-damage CZ model proposed by Kolluri et al. [121] allows for irreversible openings due to damage and/or plasticity. The combined (plasticity-damage) behavior depends on the ratio of the plastic energy and the total energy of separation using one additional parameter called the plastic limit,  $\delta_{pl}$ . The other parameters are standard ones (i.e. the interface fracture toughness  $\phi$  and critical displacement  $\delta$  characterizing the loading behavior of the traction-separation law). The plastic limit,  $\delta_{pl}$ , is defined such that for an effective maximum separation  $\Delta_{eff}$  smaller than  $\delta_{pl}$ , the cohesive zone behaves fully elasto-plastic (i.e. the interface stiffness,  $K$ , remains equal to the initial stiffness,  $K_o$ ). Once the effective maximum separation passes  $\delta_{pl}$ , the plastically deformed cohesive zone damages elastically with further separation (i.e. the interface stiffness decreases with damage parameter  $d$ ), as presented in Fig. 5.6(a). In this figure, this irreversible CZ behavior is used in conjunction with the improved Xu-Needleman CZ law for normal separation, which is used to describe the interface loading behavior.

Fig. 5.6(b) shows that by varying the plastic limit from 0 to  $\infty$ , the irreversible interface behavior of the CZ can be varied from full damage to a mixture of damage and plasticity to full plasticity. In this model, the compressive stiffness of the CZ is not influenced by the damage. For more details, the reader is referred to Chapter 4.

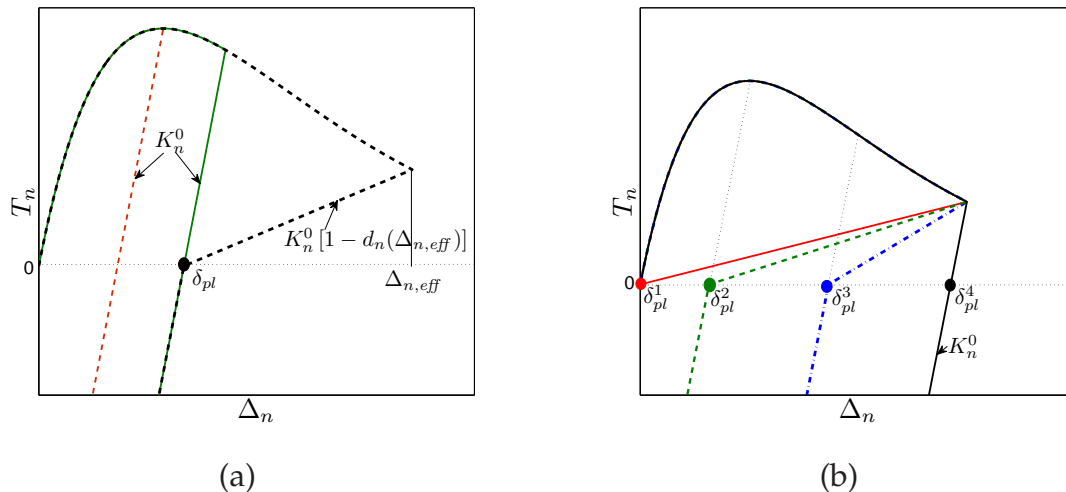


**Figure 5.6:** (a) The unloading behavior of the combined plasticity-damage CZ in normal opening above and below the plastic limit  $\delta_{pl}$ . (b) The influence of  $\delta_{pl}$  on the unloading behavior of the combined plasticity-damage CZ in normal opening.

### 5.3.2 Verification of the assumptions

In order to verify the assumptions made in the previous section, finite element simulations of a mode I delamination test on a dissimilar bilayer interface sample are performed for four classes of material behavior for the interface and bulk (representing the behavior of the fracture process zone and sample structure, respectively), given in Table 5.1. A 2D finite element model of the bilayer sample with the geometry and boundary conditions given in Fig. 5.7 has been made. The mesh was selectively refined at the interface to avoid mesh size dependency on the final results. Four-node quadrilateral elements with a maximum size of  $100\ \mu\text{m}$  and a minimum size of  $1.6\ \mu\text{m}$  are used to model the top and bottom layers of the sample. Frictionless contact conditions were used between the two surfaces of the precrack region of the specimen. Simulations were performed by assuming plane strain conditions. The CZ model described in Section 5.3.1 was implemented, whereby a return mapping solution procedure was employed to incorporate the plasticity. The behavior of the bottom layer is assumed to be elastic in all the simulations for simplicity. Hence, structural plasticity is only present in the top layer for simulations MB2 and MB4. The material properties of the two layers of the sample structure and the cohesive

**Table 5.1:** The four classes of interface (representing the fracture process zone) and bulk (representing the sample structure) material behavior used for the simulations.

Class	Interface (fracture process zone)	Bulk (sample structure)
MB1	full damage	elastic
MB2	full damage	elasto-plastic
MB3	partial damage - partial plasticity	elastic
MB4	partial damage - partial plasticity	elasto-plastic

zone parameters of the interface used in the simulations are given in Table 5.2. The cohesive zone parameters of the interface are chosen such that there is considerable permanent deformation due to plasticity in the fracture process zone (for a clear influence of process zone plasticity) and the interface strength is relatively low. Finally, the resulting load displacement responses from the simulations of the four different material classes are shown in Fig. 5.8.

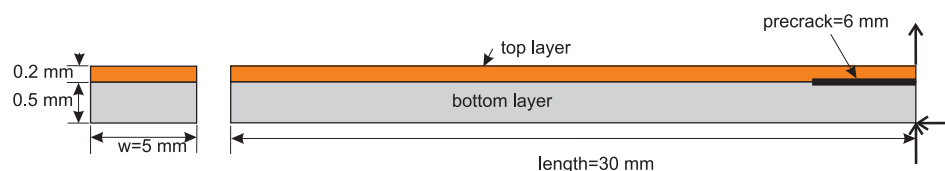


**Figure 5.7:** Geometry of the sample and the applied boundary conditions for simulations.

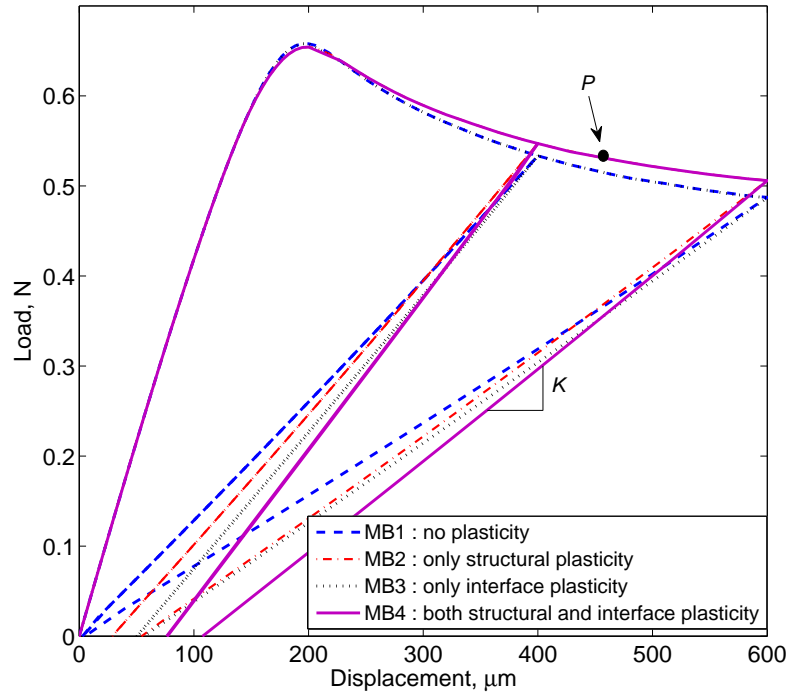


**Table 5.2:** Material properties of the sample layers and cohesive zone parameters of the interface.

Material parameters	Top layer	Bottom layer
Young's modulus (GPa)	120	30
Poisson's ratio	0.33	0.25
Yield stress (MPa)	67(for MB2 and MB4)	-
Hardening parameter (GPa)	5 (for MB2 and MB4)	-

Cohesive zone parameters	
$\phi_n$ (J/m <sup>2</sup> )	4.7
$\delta_n$ ( $\mu\text{m}$ ) or $T_{n,max}$ (MPa)	3 0.576
$\delta_{pl}$ ( $\mu\text{m}$ )	10 (MB1 and MB3)



**Figure 5.8:** Load-displacement results from the finite element simulations of a mode I delamination test performed with the four classes of interface and bulk structural material behavior given in Table 5.1.

To verify assumption 1, the (structural) unloading stiffness,  $K$ , corresponding to a given crack length,  $a$ , should not be influenced by the presence of structural plasticity, with and without interface plasticity. Because of the complications in controlling two simulations with different material behavior to unload at exactly the same crack length, a direct comparison of unloading stiffness values obtained from simulations

with structural plasticity (MB2 and MB4) with those from simulations without structural plasticity (MB1 and MB3), respectively, is not possible. To circumvent this problem, the unloading stiffness values of all four material behavior classes are plotted (in Fig. 5.9(a)) as  $K^{-1/3}$  versus the corresponding crack lengths  $a$  at each opening displacement (because  $K^{-1/3}$  should scale linearly with  $a$  when linear elastic beam theory would be valid). Note that each data point has been obtained from a separate simulation (from crack initiation to unloading) to exclude possible effects of a prior unloading. The data points from simulations with and without structural plasticity fall on one (quadratic) curve in the absence of interface plasticity (MB1 and MB2) (see Fig. 5.9(a)). Likewise, in the case with interface plasticity (MB3 and MB4), the simulations with and without structural plasticity fall on another (quadratic) curve. This demonstrates that there is indeed a negligible influence of structural plasticity on the unloading stiffness in both cases, which verifies assumption 1. Note that the slight non-linearity in relation between  $K^{-1/3}$  and  $a$  demonstrates that linear elastic beam theory oversimplifies the sample structure geometry. To check assumption 2,

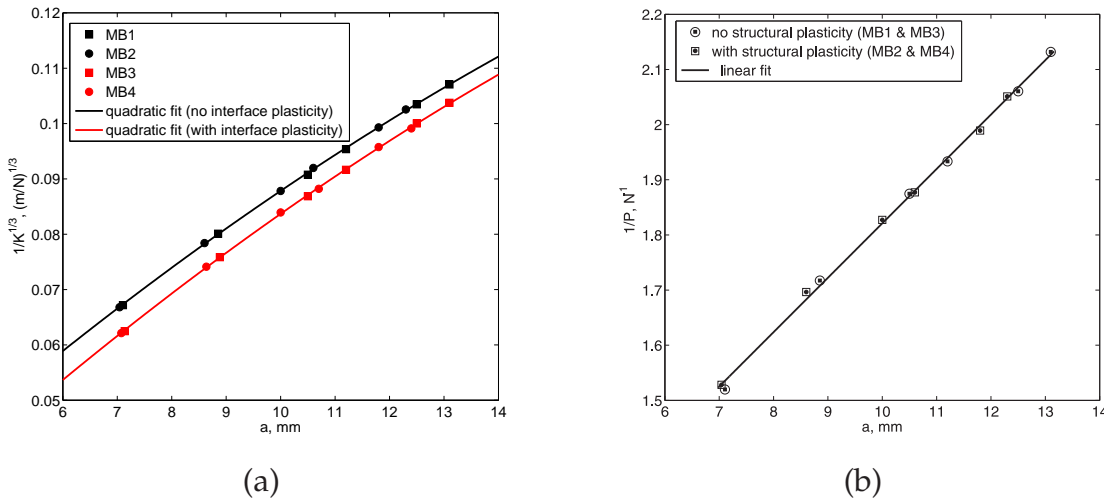


**Figure 5.9:** (a) The unloading stiffness,  $K$ , and the corresponding crack lengths  $a$  at each opening displacement are plotted as  $\frac{1}{K^{1/3}}$  versus  $a$  for all four classes of interface and bulk structural material behavior given in Table 5.1. The same (quadratic) dependency identified for cases without (MB1 and MB3) and with (MB2 and MB4) structural plasticity supports the assumption 1. (b) The inverse of the critical load points  $1/P$  of the delamination curve plotted as a function of the corresponding crack lengths  $a$  for cases without (MB1 and MB3) and with structural (MB2 and MB4) plasticity in order to verify assumption 2.

the inverse of the critical load points on the delamination curve are plotted as a function of the corresponding crack lengths for both cases with and without structural plasticity as shown in Fig. 5.9(b). The observed linear dependency between  $P^{-1}$  and  $a$  with the same slope for all cases (MB1 and MB3, MB2 and MB4) indicates that the

critical load for delamination is the same for samples with and without structural plasticity.

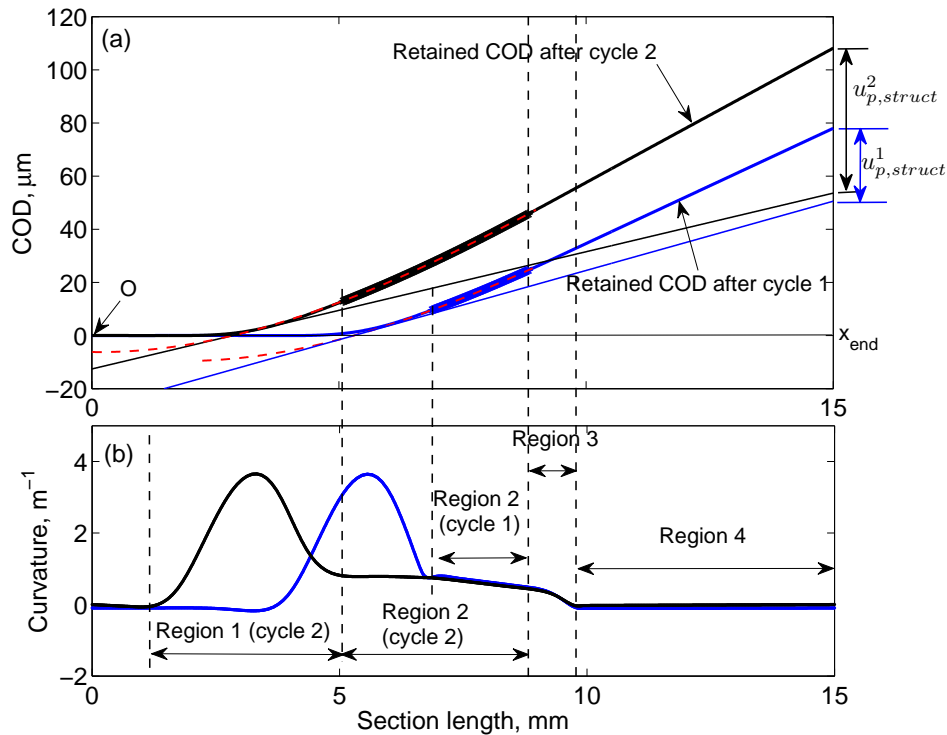


**Figure 5.10:** (a) Retained crack opening displacement (COD) profiles after complete unloading of cycle 1 and cycle 2 for the case of MB4 (both interface and structural plasticity), and (b) corresponding curvature plots illustrating the four different regions. Fig. (b) shows that the size and shape of the (fully developed) process zone remain constant with respect to the crack tip position during crack growth from cycle 1 to cycle 2, while the plastic curvature in region 2 stays nearly constant in time and place. Fig. (a) also shows the procedure to obtain the contribution of structural plasticity to the retained opening for cycle 1 and cycle 2 (i.e.  $u_{p,struct}^1$  and  $u_{p,struct}^2$  respectively) using the proposed approach.

To check the validity of assumption 3 and 4, the retained curvature after complete unloading of cycle 1 and cycle 2 for the case of MB4 is shown in Fig. 5.10. The different regions of the retained opening profile (of cycle 2) identified on the curvature plot are also shown in Fig. 5.10. The curvature graph (Fig. 5.10(b)) shows that the size and the shape of the (fully developed) process zone (region 1) stays nearly constant with respect to the crack tip location and simply traverses with further growth of delamination from the point of unloading of cycle 1 to unloading of cycle 2, i.e. supporting assumption 3. This figure also shows the same retained structural plastic

curvature in region 2 (of delaminated specimen arms) for both cycles, indicating that the plastic curvature stays nearly constant in time with further loading once the process zone has passed. Therefore, figure 5.10 shows that the structural layers of the sample deform plastically only in the region close to the process zone (i.e. region 1), consistent with assumption 4.

Since all four assumptions made in the previous section have been numerically verified, the proposed approach is next applied to a numerical problem for which both bulk and interface plasticity are present.

### 5.3.3 Numerical verification of the approach

Using the area  $ACDB$  from the load-displacement curve of MB4 (Fig. 5.11) for which both structural and interface plasticity are present, an interface fracture toughness value of  $6.05 \text{ J/m}^2$  would be obtained without separation of structural plastic contributions. This value is 29% larger than the actual input value of  $4.7 \text{ J/m}^2$ . Therefore, as a verification of the proposed approach, the structural plastic contribution to the dissipated energy is separated to assess the obtained value for the interface fracture toughness. The regions 2 of the retained COD profiles corresponding to the unloading of cycle 1 and cycle 2 are fitted with cubic polynomials (as shown in Fig. 5.10(a)). Cubic polynomials were selected because the curvature profiles vary nearly linear with section length for both cycles in region 2. The fitted curves are extrapolated into the corresponding region 1 of each cycle to find the intersection points on the axis  $Ox_{end}$ . The tangents drawn at these intersection points are extended to  $x_{end}$  to obtain the retained openings due to structural plasticity,  $u_{p,struct}^1$  and  $u_{p,struct}^2$  of cycle 1 and cycle 2, respectively (Fig. 5.10(a)). As explained in section 5.2.2, the unloading stiffness lines corresponding to cycle 1 and cycle 2 are then translated over a distance  $u_{p,struct}^1$  and  $u_{p,struct}^2$  towards the origin to identify the two points,  $A'$  and  $C'$ , (corresponding to  $A$  and  $C$  respectively) on the reconstructed curve. The points  $X'$  between  $A'$  and  $C'$  are obtained by linear scaling of  $u_{p,struct,X'}$  between  $u_{p,struct}^1$  and  $u_{p,struct}^2$  as explained in Section 5.2.2. Using the area  $A'C'D'B'$  from the reconstructed curve (Fig. 5.11), an interface fracture toughness of  $4.82 \text{ J/m}^2$  is obtained which is in good agreement with the input value of  $4.70 \text{ J/m}^2$ .

## 5.4 Application: determination of the interface fracture toughness in CuLF-MCE

In this section, the proposed approach for the separation of structural plastic contributions from the measured load-displacement response is experimentally assessed by separating the induced structural plasticity and comparing the resulting interface fracture toughness with the value obtained from another sample of the same interface in which no structural plasticity occurred. For this purpose, industrially relevant

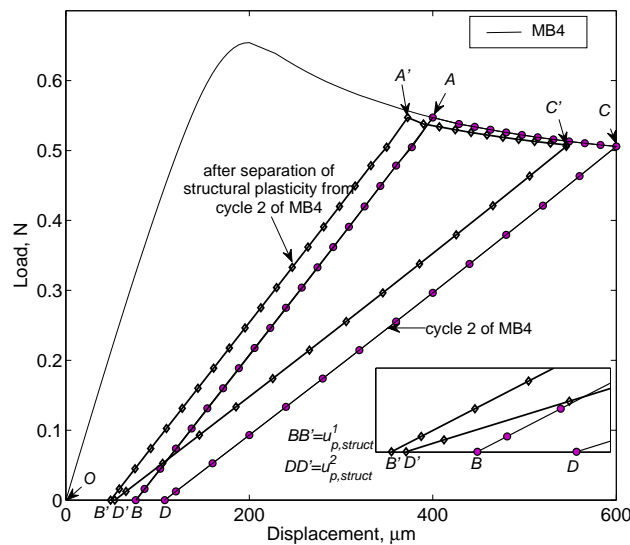


**Figure 5.11:** Load-displacement response for MB4 (structural and interface plasticity). The structural plastic contribution is separated from the total dissipated energy ( $ACDB$ ) for MB4 by employing the procedure described in Section 5.2.2 (i.e. by reconstructing  $A'C'D'B'$ ).

copper lead frame-molding compound epoxy (CuLF-MCE) bilayer samples with two different thicknesses, 0.2 mm and 0.15 mm, of the CuLF layer and, the same thickness 0.5 mm, of the MCE layer are chosen. Rest of the dimensions (5 mm width, 35 mm length and 0.5 mm MCE layer thickness) are the same for both samples. The thick CuLF layer shows no structural plasticity, whereas considerable structural plasticity occurs in the thin CuLF sample during delamination. The MCE layer is always elastic in both cases.

The load-displacement response of a mode I delamination experiment performed on the thick CuLF-MCE sample is shown in Fig. 5.12(a). From the graph it is clear that there is indeed no interface or structural plasticity present in this first experiment. An interface fracture toughness value of  $36 \text{ J/m}^2$  is obtained by simply dividing the energy dissipated in a loading-delamination-unloading cycle with the corresponding increase in crack length and sample width. Note that the first loading-unloading cycle is generally ignored because it includes the crack initiation regime and the development of the process zone. On the other hand, the load-displacement response of a mode I delamination experiment performed on a thin CuLF-MCE sample (black line in Fig. 5.12(b)) reveals considerable retained opening after unloading to zero load. The interface fracture toughness value calculated using the total energy spent in the second loading-unloading cycle (area  $BACD$  in Fig. 5.12(b)) and the corresponding increase in crack length during this cycle gives a value of  $73 \text{ J/m}^2$  which is more than twice the value measured for the thick copper layer.

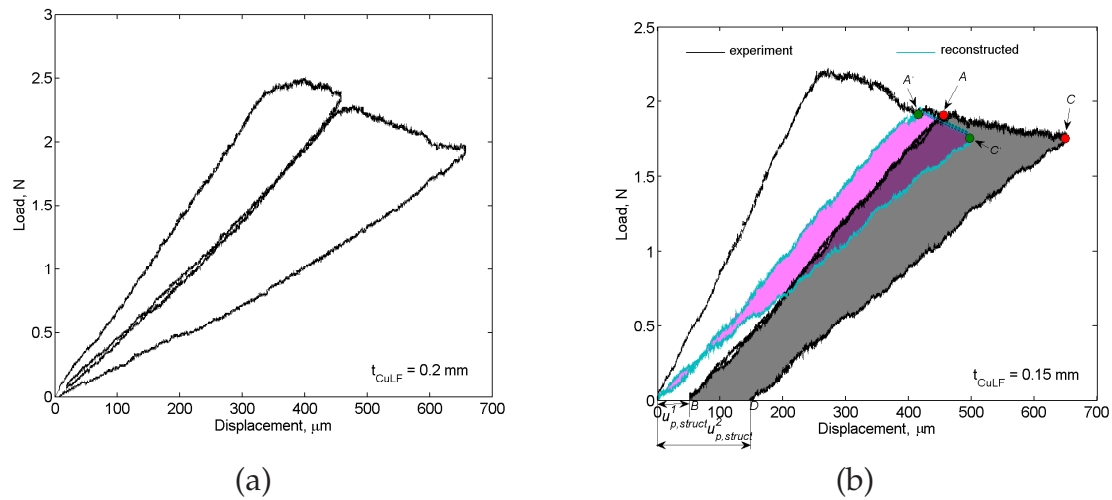


**Figure 5.12:** Load-displacement response of a mode I delamination experiment conducted on (a) a thick CuLF(0.2 mm)-MCE(0.5 mm) bilayer sample showing negligible retained opening after complete unloading; (b) a thin CuLF(0.15 mm)-MCE(0.5 mm) bilayer sample exhibiting a retained structural opening. The shaded grey area ( $ACDB$ ) shows the total energy spent during loading-unloading cycle 2. The reconstructed curve with the enclosed magenta filled area ( $OA'C'$ ) shows the delamination energy in cycle 2 after separation of the structural plastic contribution.

For the present situation, it is known that the complete retained opening in Fig. 5.12(b) and the additional dissipation originates from plasticity in the layers of the sample structure, because there was no interface plasticity observed for the thick CuLF-MCE sample. Nevertheless, the general procedure described for the case of both interface and structural plasticity (see Section 5.2.2) is applied for the separation of the structural plastic contribution. That means, first the retained COD profiles of the sample after unloading of cycle 1 and cycle 2 to zero load (i.e. at points  $B$  and  $D$  in Fig. 5.12(b)) are obtained by digital image correlation (DIC) analysis of images of the sample taken before the start and after each cycle of the delamination test. To obtain a random pattern that allows for accurate image correlation, the surface of each sample is carefully polished after which silver nano-particles (with a size of 50 - 100 nm) are applied before the beginning of the actual delamination test. The micrograph of the retained opening profile with the DIC measured displacement field overlay and the corresponding COD profile after unloading of cycle 2 are shown in Fig. 5.13. Region 2 (identified as outlined in Section 5.3.3) of the measured COD profiles are fitted accurately ( $R^2 > 0.9995$ ) with cubic polynomials and extrapolated into region 1 onto the axis  $Ox$ . The polynomial fit extrapolated to  $Ox$  for the unloaded COD profile (cycle 2) are shown in the middle figure of Fig. 5.13. It should be noted that the error between the measured COD profile and the fitted curve in region 2 is noticeably small as shown in the bottom graph of Fig. 5.13. The extrapolated cubic polynomial curve touches the axis  $Ox$  with an almost zero slope (lowest point in the zoom box of

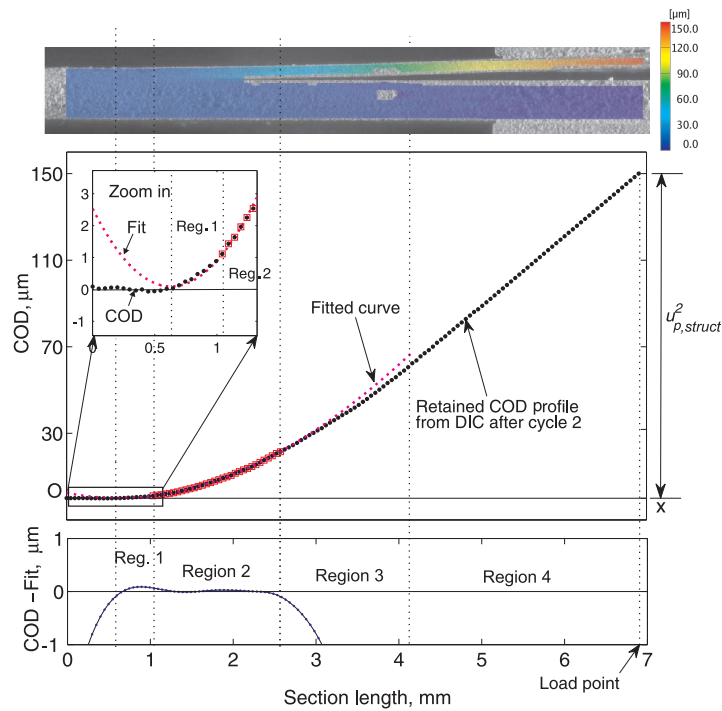


**Figure 5.13:** A micrograph of the sample taken after complete unloading of cycle 2 with a digital image correlation (DIC) displacement field overlay is shown in the top figure. The retained crack opening displacement (COD) profile measured (by DIC analysis) for the sample after complete unloading of cycle 2, and the different regions are shown in the middle figure. The error in the cubic polynomial fit of region 2 as a function of the section length is shown in the bottom figure. It can be observed that the polynomial fits the COD data with an error of less than  $0.1 \mu\text{m}$  over the full length of region 2.

Fig. 5.13) confirming that, indeed, there is only structural plasticity present during this delamination experiment. Accordingly, the identified values of  $u_{p,struct}^1 = 50 \mu\text{m}$  and  $u_{p,struct}^2 = 150 \mu\text{m}$  are exactly the same as the global retained openings  $u_p^1$  and  $u_p^2$  found from the load-displacement graph after unloading of each cycle. Subsequently, the unloading stiffness lines  $AB$  and  $CD$  are translated towards the origin over a distance  $u_{p,struct}^1$  and  $u_{p,struct}^2$  (or  $OB$  and  $OD$ ) to identify the two points  $A'$  and  $C'$  on the reconstructed curve, respectively. The points in between  $A'$  and  $C'$  on the reconstructed curve are obtained by using the interpolation function described in Section 5.2. The area surrounded by the curves  $OA'C'$  corresponds to the energy spent for interface delamination only. The fracture toughness value obtained is  $31 \text{ J/m}^2$  which is in adequate agreement with the value of  $36 \text{ J/m}^2$  for the thick CuLF-MCE sample without observable structural plasticity and which is less than 50% of the value ( $73 \text{ J/m}^2$ ) obtained before application of the structural plasticity separation method. The remaining deviation is attributed to measurement uncertainties in the delamination experiment (load, displacement, crack length and COD measure-

ments), statistical differences in the interface behavior of the two different sample (although they are from the same batch), and the model approximations made. The small error involved in fitting the plastically deformed region (region 2) contributes negligibly to the observed deviation. As a conclusion, it can be stated that, if ignored, the structural plastic deformation of the sample layers during delamination can introduce large errors in the measurement of the interface fracture toughness. The developed procedure for the separation of structural plasticity is a useful method that is generally applicable to most of the existing delamination growth experiments (that apply loads to trigger delamination) to obtain realistic values of the interface fracture toughness, if (structural) plastic deformation occurs in the adherent layers forming the interface.

## 5.5 Conclusions

Delamination characterization of multi-layer structures containing ductile layers is challenging because of the occurrence of permanent deformation of adherent layers of the sample structure during delamination. Large errors in the measurement of the interface fracture toughness can result if these structural plastic dissipations are neglected in the calculation of the interface fracture toughness. Therefore, a semi-analytical approach accounting for the structural plasticity in adherent layers of the sample is proposed, aiming for accurate values of the interface fracture toughness in a mode I experiment. The approach relies on the reconstruction of the equivalent force-displacement curve for the no structural plasticity case, departing from the measured force-displacement response. Individual contributions of structural plasticity and interface plasticity to the total retained opening are identified after complete unloading of the sample. This is achieved by assuming (for a given crack length) that both the structural unloading stiffness and the critical load for delamination are not affected by permanent deformation of the sample structure. The partitioning of the individual contributions of structural plasticity and interface plasticity to the total retained opening is achieved on the retained crack opening profiles of the sample. This procedure assumes a constant size and shape of the process zone and a sample structure that deforms plastically only in the region close to the process zone (i.e. no increase in structural plasticity after the process zone has passed by). The proposed approach and its underlying assumptions have been numerically verified by employing a finite element model with a known cohesive zone response at the interface. As a verification of the approach, the structural plastic contribution to the dissipated energy was successfully separated from a numerical simulation of a delamination experiment where both structural and interface plasticity are present thereby recovering the correct value for the interface fracture toughness. The proposed approach has also experimentally been assessed by characterizing the interface fracture toughness of industrially relevant copper lead frame-molding compound epoxy (CuLF-MCE) samples. In this example, it was found that a correction of the interface fracture toughness of more than a factor of two results by applying



this approach. The approach presented in this paper is generally applicable for most of the existing delamination growth experiments, as it only requires the determination of the crack opening displacement profile before and after the delamination test. Moreover, the approach does neither require any analytical solution or numerical simulation nor the explicit details of the constitutive behavior of the adherents. Finally, it is noted that the proposed approach is not applicable when the structural arms of the sample undergo plastic deformation during unloading (i.e. reverse plasticity), because reverse plasticity changes the structural unloading stiffness making assumption 1 no longer valid.

# Characterization of industrially relevant interface structures

---

## Abstract

In this Chapter, the experimental tools developed in this thesis are employed for the characterization of delamination in two types of industrially relevant interface samples, i.e. uncoated copper lead frame-white molding compound (uncoated CuLF-WMC) and coated copper lead frame-molding compound epoxy (coated CuLF-MCE). A comparative study of the differences in the load-displacement responses, critical energy release rate versus mode angle trends, cohesive zone traction-separation laws and the observed delamination mechanisms is presented. It was found that the fracture toughnesses of both interfaces differ by approximately a factor of two, whereas the measured traction-separation laws showed that the coated CuLF-MCE interface is approximately a factor of 14 more brittle than the uncoated CuLF-WMC interface. These differences in toughness and brittleness of the interfaces may be explained on the basis of microscopic examination of the delamination front, which provides evidence of large scale bridging in case of uncoated CuLF-WMC compared to localized, brittle de-adhesion behavior observed in coated CuLF-MCE samples.

## 6.1 Introduction

As already emphasized in the previous chapters, interface delamination is often considered as a reliability concern in packaging of micro-electronic systems due to the presence of (manufacturing induced) high thermal stresses at the interfaces between the encapsulant (which is typically a molding compound epoxy (MCE) and the dif-

ferent outer material layers of the micro-electronic system such as lead frame, die and die pad. Consequently, there is considerable interest in the development of new encapsulant materials with better adhesion properties. For example, a new molding compound epoxy encapsulant named white molding compound (WMC) is being developed by the industry to replace the conventional (black) MCE. Once a new material is developed, it is necessary to characterize the delamination behavior of the associated interfaces to assess the adhesion performance of the new interface system. Moreover, accurate quantification of interface properties is needed for further optimization of the overall design of micro-electronic systems, for example, by using predictive finite element models.

The goal of this chapter is to fully characterize and compare the delamination behavior (including the mixed mode cohesive zone (CZ) properties) of (i) an interface between a newly developed encapsulant (WMC) and an uncoated copper lead frame (CuLF), and (ii) a reference interface between conventional (black) molding compound epoxy and an alloy coated CuLF (for which the CERR values were already determined in Chapter 3). To this end, the developed miniature mixed mode bending (MMMB) setup (Chapter 3) and parameter identification procedure (Chapter 4) are employed.

This chapter is organized as follows. First, a brief description of the manufacturing procedure, geometry and material properties of the samples is given, followed by the specimen preparation procedure for digital image correlation (DIC) analysis on either optical microscopy or scanning electron microscopy (SEM) images. Next, a comparative discussion of the measured load-displacement responses, CERR versus mode angle trends, CZ traction-separation laws and the observed delamination mechanisms is given and, finally, conclusions are drawn.

## 6.2 Sample specification

Bi-layer samples of both the uncoated CuLF-WMC and coated CuLF-MCE interface systems have been manufactured at Philips Applied Technologies. The material properties of the adherent (bulk material) layers (supplied by the manufacturers) and geometry of both the bi-layer samples are given in Tab. 6.1 and Fig. 6.1, respectively.

**Table 6.1:** Material properties of the two different interface samples used in this study.

Material parameters	coated CuLF	MCE	uncoated CuLF	WMC
Young's modulus (GPa)	120	30	120	8
Poisson's ratio	0.33	0.25	0.33	0.25

A similar production procedure was applied for both sample types. First, the lead

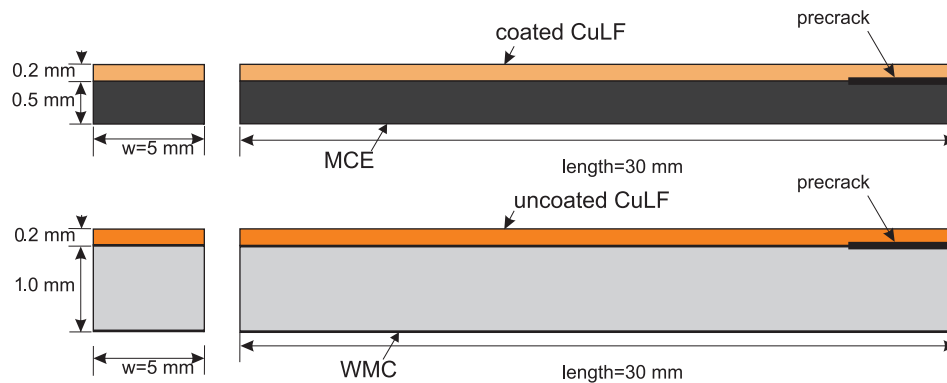


**Figure 6.1:** Geometry of both the interface samples used in this study.

frame was heated to  $180^{\circ}\text{C}$  for 2.5 minutes followed by high pressure hot injection molding of the molding compound. Afterwards, the samples were laser cut to the required dimensions ( $35 \times 5\text{ mm}$ ). After the molding process, the samples received a post mold cure for 4 hours at  $175^{\circ}\text{C}$ . At the end of each sample, a pre-crack ( $\sim 6\text{ mm}$ ) was created by sliding a thin ( $\sim 10\ \mu\text{m}$ ) knife edge between the two layers.

### 6.3 Specimen preparation for digital image correlation

The goal of the *in-situ* mixed mode delamination experiments is not only to obtain the CERR values at all mode mixities but also to quantitatively identify all the CZ parameters (e.g. the critical separation length) such that the interface traction-separation relation can be modeled using a cohesive zone approach. A procedure for extraction of all CZ parameters of the improved Xu-Needleman model (Eqs. 4.34 and 4.35) using the data obtained from the *in-situ* measurements was described in Section 4.5. To be able to use the proposed procedure for CZ parameter extraction, measurements of the local displacement field at the crack tip and rotations at the loading points are needed in addition to the global load-displacement response. Moreover, it is also important to capture the displacement fields to analyze and separate possible plasticity in the adherent bulk layers during delamination, as explained in Chapter 5, and to accurately measure the increase in crack length during delamination (to obtain correct CERR values). To obtain the displacement fields, the images captured during delamination are analyzed by digital image correlation (DIC). To be able to accurately determine the displacement fields using DIC analysis, a random grey scale speckle pattern without sharp variations in the averaged brightness between different regions of the surface is needed. For the current interface samples, without additional preparation, a sharp variation in the brightness levels is observed (under optical stereo microscopic visualization) because the layers forming the interface (metal and epoxy) have largely different light reflective properties. Moreover, the contrast of the microstructural features (on the surface) of the layers was insufficient

to obtain a sub-micron scale resolution in the displacement measurement. Therefore, the following specimen preparation procedure is applied in order to obtain a random pattern that allows for accurate high-resolution correlation. First, the surface (perpendicular to the plane of the interface) of each sample is carefully fine polished using a standard metallographic procedure (with a succession of intermediate and fine polishing steps), after which, the surface is cleaned with ethanol. Next, silver nano-particles (with a size of 50-100 nm) are applied by dipping the polished side of the surface in a container with nano particles. Figure 6.2 shows the distribution of nano-particles. It was observed that the nano particles form random clusters with sizes up to tens of micrometers which provide good randomness and contrast, as required for the speckle pattern for correlation. The particles are applied after introducing the required pre-crack at the end of the sample and attaching the dovetail connectors as explained in Section 3.5.1.

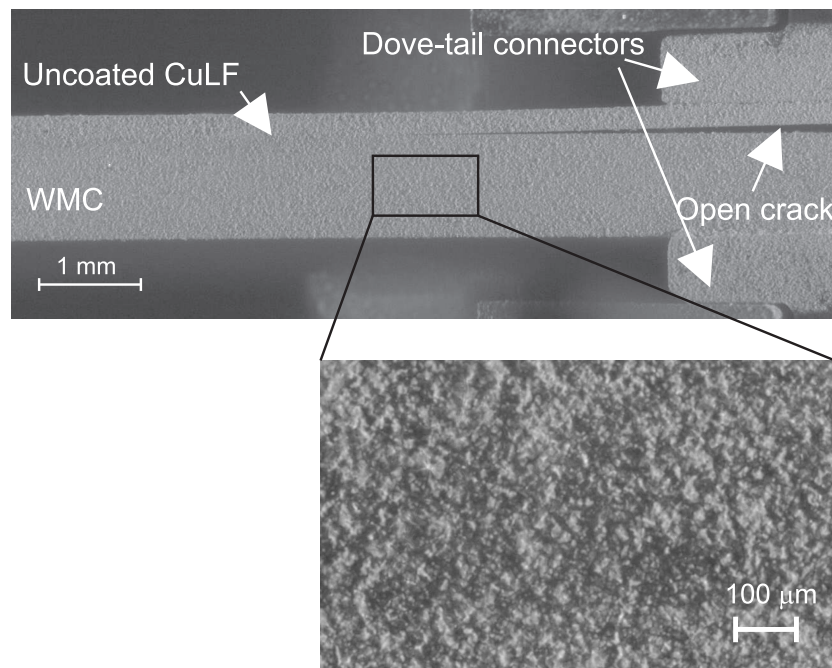


**Figure 6.2:** Micrograph of a bi-layer CuLF-WMC specimen (with attached dove-tail connectors) showing the distribution of nano particles on the surface (perpendicular to the plane of the interface) of the sample. Note that the specimen is loaded in normal direction (mode I), therefore, showing the crack in an open position.

Figure 6.3 shows the stereo micrographs of the uncoated CuLF-WMC samples taken at four different global opening displacements with a DIC total strain field overlay and corresponding position displacement profiles. From this figure, lateral movement of the crack tip with increase in global opening displacement can be clearly seen. The measured displacement field provides the data required for the measure-

ment of the traction-separation law, as explained in the next sections.

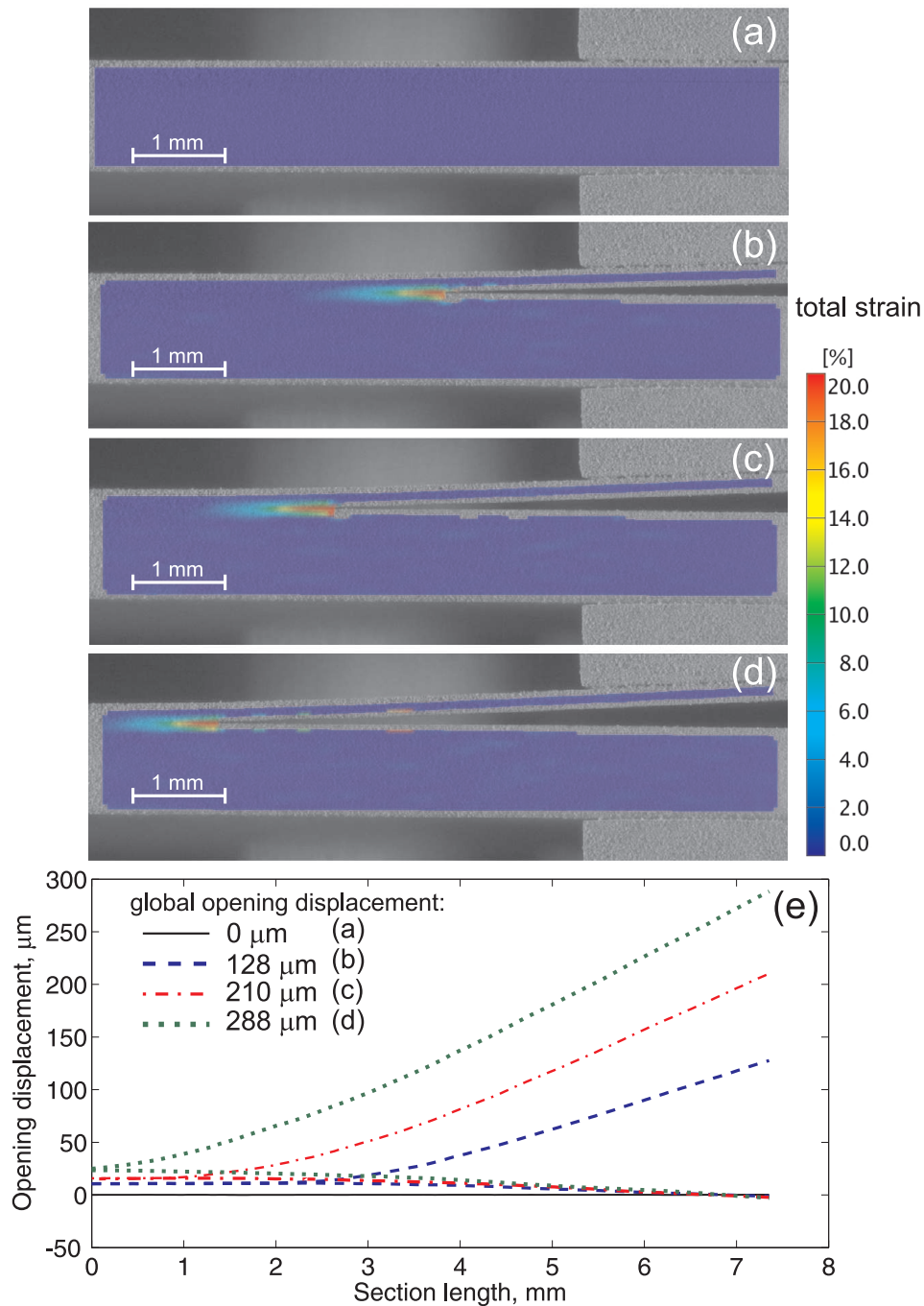


**Figure 6.3:** (a-d) Stereo micrographs of the uncoated CuLF-WMC samples with a DIC total strain field overlay taken at four different global opening displacements. (e) Vertical position displacement profiles, corresponding to the DIC strain fields of (a-d).

## 6.4 Experimental results and discussion

### 6.4.1 Measurement of CERR versus mode angle

Before conducting actual delamination experiments, to estimate the mode angle at the interface for different relative loading positions, finite element (FEM) simulations were performed for all loading positions using the full model of the setup and an elastic material model of both the coated CuLF-MCE sample and the uncoated CuLF-WMC samples as explained in Sections 2.2.3 and 3.4.2. The simulations of the mode angle ( $\psi$ , as defined in Eq. 3.8) versus the relative MMMB loading position ( $\xi$ , as explained in Section 2.2.1) for both samples are shown in Fig. 6.4. Pure mode II positions shown in the graph are obtained using Eq. 3.4. For a given relative loading position, the difference in the mode angle between the two samples (Fig. 6.4) is explained by the dependency of the mode angle on the geometry and the material properties of the two adherent layers.

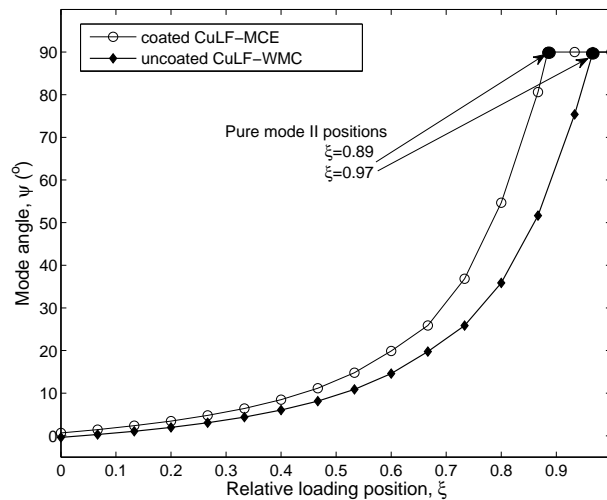


**Figure 6.4:** Mode angle obtained by FEM analysis as a function of relative loading position ( $\xi$ ) for (i) the coated CuLF-MCE samples and (ii) the uncoated CuLF-WMC samples used in this study, as simulated for a pre-crack length of 6 mm and a global displacement of 200  $\mu\text{m}$ .

Figure 6.5(a) shows the load-displacement plots of the *in-situ* delamination experiments conducted on the uncoated CuLF-WMC interface system under a stereo microscopic observation at mode I ( $\xi = 0$ ) and mixed mode loading positions ( $\xi = 0.27, 0.4, 0.53, 0.67$  and  $0.8$ ). For the sake of comparison, load-displacement plots of the coated CuLF-MCE (at  $\xi = 0, 0.4, 0.67$  and  $0.8$ ), which were already presented in

Chapter 3, are also shown in Fig. 6.5(b). For all experiments and at all mode mixities, first a linear increase in the load is observed with increasing displacement up to a critical load at which a sudden decrease in the load occurs with further increase in the displacement, which is caused by the onset of delamination for all mode mixities. A direct comparison of the load-displacement values at mode I ( $\xi = 0$ ) reveals that the critical load levels during delamination growth in the case of uncoated CuLF-WMC are higher compared to the coated CuLF-MCE case.

Critical energy release rate values are obtained by dividing the energy absorbed in each loading-delamination-unloading cycle with the corresponding increase in the crack length and the width of the sample. Comparison of the CERR versus mode angle curves (shown in Fig. 6.6) for both interface structures, shows that the CERR values at any given mode angle are higher for uncoated CuLF-WMC interface structures, which corresponds to the higher critical loads observed in Fig. 6.5. Moreover, there is a considerable difference in the overall trends of both interfaces. For example, differences in the rate of increase of CERR with increasing mode angle indicate a marked difference in the mixed mode coupling between the two interfaces. For coated CuLF-MCE structures, at low mode angles ( $\psi < 25^\circ$ ) this rate (i.e. mode angle dependency) is almost negligible, indicating that CERR values in the mode I dominant regime are not much influenced by a shear contribution. In contrast, for the uncoated CuLF-WMC interface, there is a strong influence of shear separation on mixed mode CERR values already starting from  $\psi = 10^\circ$ .

## 6.4.2 Extraction of cohesive zone parameters

### Extraction of mode I traction-separation law

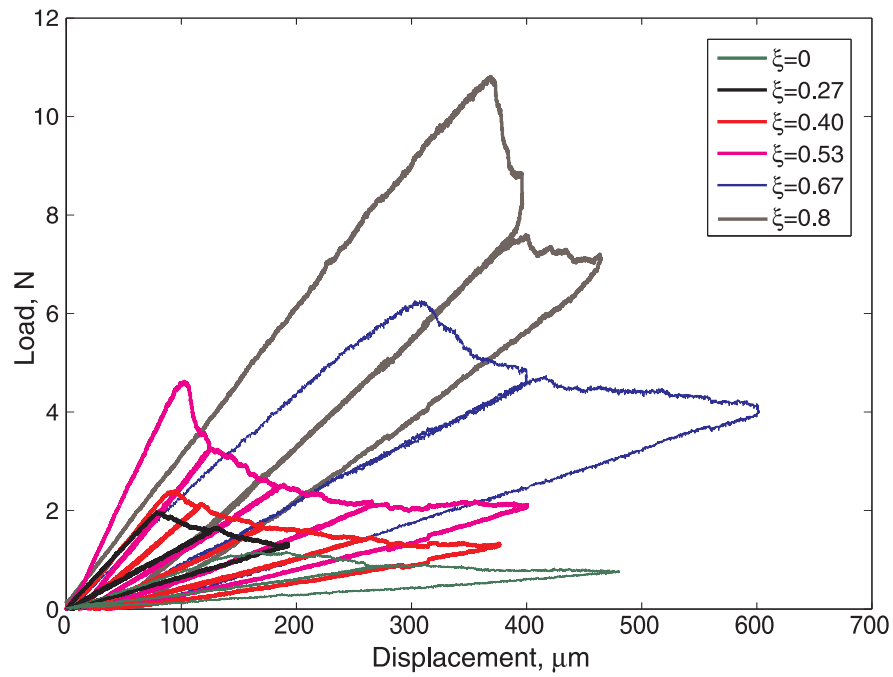
A procedure for extraction of all the parameters of a chosen mixed mode cohesive zone law, in this case the improved Xu-Needleman exponential CZ law, from the *in-situ* delamination experiments performed using the MMMB setup was given in Section 4.5. In this procedure, first, the full mode I traction-separation relation of the interface is extracted using Andersson and Stigh's approach [97]. The formula given by Andersson and Stigh is generalized for dissimilar DCB interface samples for the current purpose:

$$T_{n,exp} = \frac{d(F(\theta_t + \theta_b))}{Bd(\Delta_{n,exp})}, \quad (6.1)$$

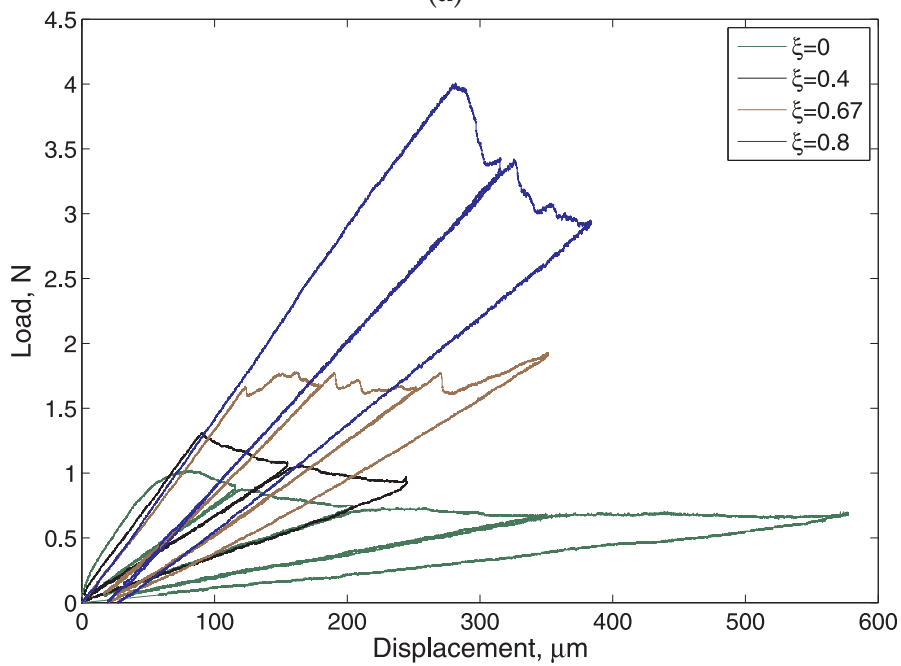
where,  $F$  is the force applied at the loading point on a DCB specimen (Fig. 6.7),  $\Delta_{n,exp}$  is the opening displacement of the interface layer at the initial crack tip,  $B$  is the width of the sample and  $\theta_t, \theta_b$  are the rotation at the loading points of the top and bottom layers of the DCB specimen, respectively.

The displacement field data obtained from the DIC analysis (see Section 6.3) was used to obtain the crack opening displacements at the initial crack tip ( $\Delta_{n,exp}$ ) and ro-





(a)



(b)

**Figure 6.5:** Comparison of load-displacement plots of mode I and mixed mode experiments conducted on (a) uncoated CuLF-WMC and (b) coated CuLF-MCE samples.

tations at the loading points of both layers ( $\theta_i$  and  $\theta_b$ ). Substituting this data together with the global force measurement into Eq. 6.1 yields the traction-separation relation of the interface for mode I loading. Figure 6.8 shows the traction-separation plots

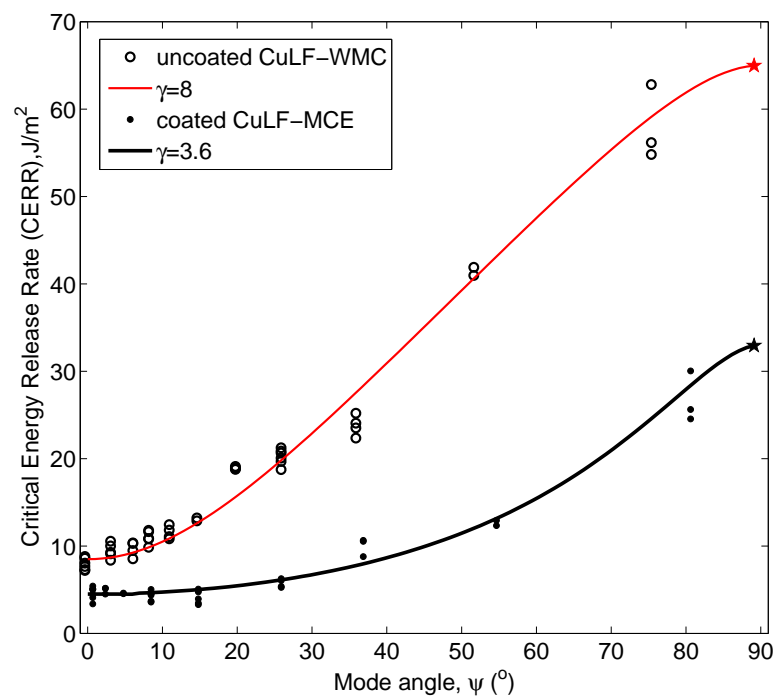


**Figure 6.6:** Experimentally obtained CERR values of uncoated CuLF-WMC and coated CuLF-MCE samples as a function of the mode angle,  $\psi$ . Also shown is the total work of separation of the improved Xu-Needleman cohesive zone model,  $\omega_{tot}$  (as given by Eq. 4.48), fitted to the experimental CERR versus model angle curves.

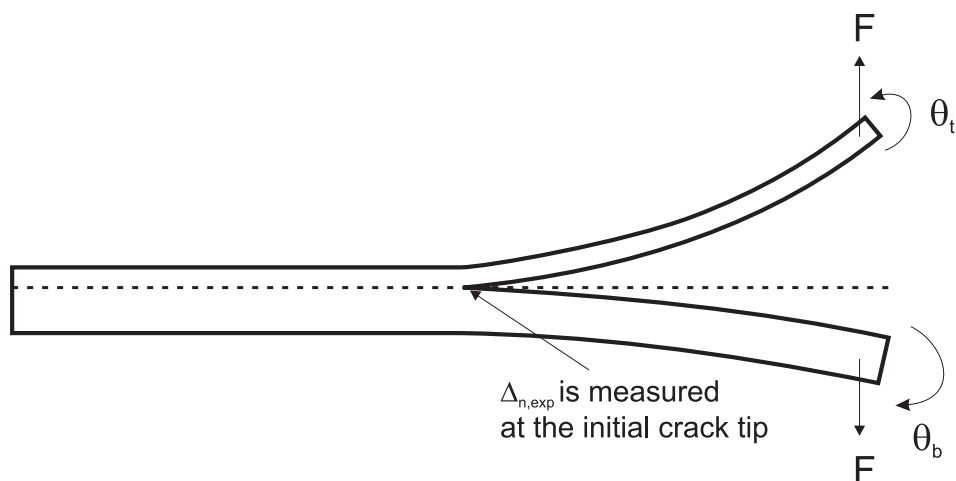


**Figure 6.7:** DCB specimen indicating the loading points and the corresponding rotations of the top and bottom layers.

obtained for both uncoated CuLF-WMC and coated CuLF-MCE interface samples.

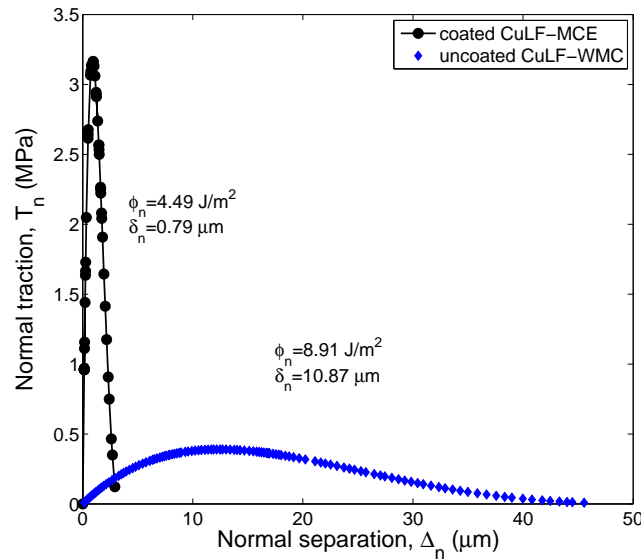


**Figure 6.8:** Comparison of the measured traction-separation behaviors of the uncoated CuLF-WMC and coated CuLF-MCE samples.

Note that the measured traction-separation curve can be directly used to model and predict the interface behavior for mode I loading. However, this method may not be straightforward for situations where modeling of the complete mixed-mode behavior of the interface is needed. Therefore, a mixed-mode CZ law that adequately represents the traction-separation behavior of the interface of interest is used, where identification of all parameters of the model allows to describe the full mixed-mode behavior of the interface. In the present study, the improved Xu-Needleman CZ law was chosen. Mode I parameters ( $\phi_n$  and  $T_{n,max}$  (or  $\delta_n$ )) are obtained by fitting the chosen CZ law to the measured traction-separation relation as shown in Fig. 6.9. It is obvious from Fig. 6.9 that the coated CuLF-MCE shows a relatively brittle behavior with a critical separation length ( $\delta_n$ ) that is 14 times lower compared to the uncoated CuLF-WMC interface, whereas the difference in the CERR ( $\phi_n$ ) is only a factor 2.

In situ SEM studies of the uncoated CuLF-WMC samples reveals the existence of a large fracture process zone with crack bridging over hundreds of microns away from the crack tip (see Fig. 6.10). This is illustrated in Fig. 6.10, in which several images taken along the interface are stitched together to show the large process zone and the details of the crack bridges along the process zone for uncoated CuLF-WMC. On the other hand, a brittle de-adhesion mechanism associated with rare bridging (see Fig. 3.16) within 100 microns from the crack tip was observed in the case of the coated CuLF-MCE samples. The observed difference in crack bridging behavior seems to be correlated to the measured difference in critical separation lengths  $\delta_n$ .

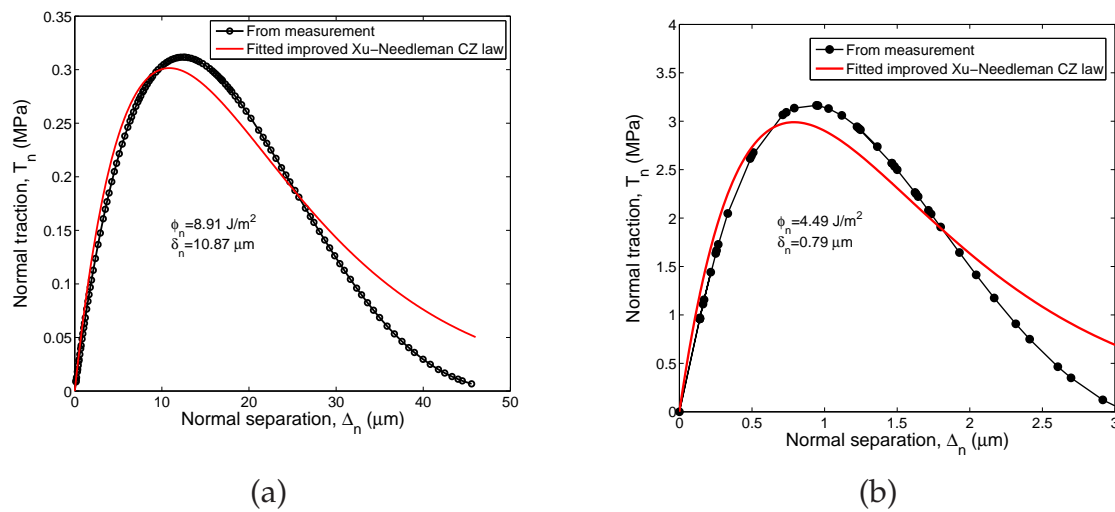


**Figure 6.9:** Normal traction-separation relations of (a) uncoated CuLF-WMC and (b) coated CuLF-MCE interfaces. The improved Xu-Needleman normal CZ law is fitted to extract the CZ parameters, i.e.  $\phi_n$  and  $\delta_n$ .

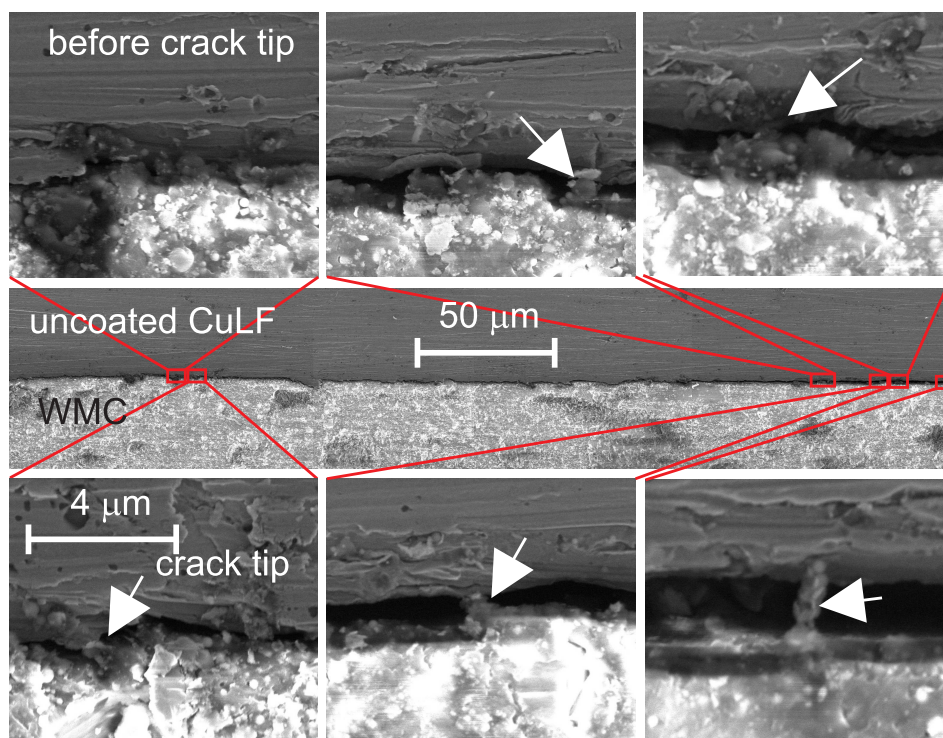


**Figure 6.10:** SEM micrographs showing the bridge ligaments (shown with arrows) far ( $> 100 \mu\text{m}$ ) from the crack tip for a mode I delamination test on uncoated CuLF-WMC.

Figure 6.10 also shows a maximum bridge length of  $\sim 3 \mu\text{m}$  for uncoated CuLF-

WMC compared to values of  $< 1 \mu\text{m}$  in case of coated CuLF-MCE. Even though the observed difference in the maximum bridge length of both interfaces may be related to the difference in measured traction-separation laws (shown in Fig. 6.8), there is an apparent discrepancy between the absolute values of microscopically observed maximum bridge lengths and fracture opening displacements, i.e.  $\delta_f \approx 4\delta_n$  (at which the traction drops (almost) to zero) obtained from the measured traction-separation responses. This discrepancy could be attributed to the following reasons. On one hand, in the Andersson and Stigh approach, the bulk adherent layers are assumed to be fully elastic, and therefore, the technique lumps all the dissipative mechanisms, which include both interface deadhesion, plastic deformation at the interface, and possible plastic deformation in an adjacent bulk region, into the measured traction-separation behavior of the interface. On the other hand, in the visual measurement of the crack bridge lengths on the basis of the SEM images, plastic deformation of the interface and plastic deformation in an adjacent bulk region are completely ignored. Indeed, a preliminary analysis shows that a normal opening of  $\sim 10 \mu\text{m}$  was measured from the DIC data (shown in Fig. 6.3) at the location where the interface appears to be still intact in the SEM micrograph just before the crack tip (Fig. 6.10), thereby indicating the presence of significant plastic deformation in the interfacial region that is ignored in the crack bridge length measurement. In addition to the above arguments, other sources of error might contribute to the above-mentioned apparent discrepancy, including the measurement uncertainties of both techniques, the possible significant influence of polishing of the side of the sample which may induce partial damage in the interface close to the edge due to material removal, and the possible systematic errors in the measured traction-separation behavior due to the underlying assumptions in the Andersson and Stigh approach. To conclude, it is clear that a complete (quantitative) understanding of the observed discrepancy requires a more detailed analysis of all the above mentioned issues.

## Mode II parameter extraction

Since the pure mode II loading position falls between two discrete loading positions for these specific interfaces, it is not possible to carry out pure mode II tests. Hence, the fitted curves are extrapolated to  $90^\circ$  to get the mode II CERR values (plotted as stars in Fig. 6.6). The mode II interface strength ( $T_{t,max}$ ) is determined using the CERR values obtained from mixed mode tests performed at different mode angles spanning mode I to mode II. This is done by fitting Eq. 4.48 to the CERR versus mode angle data. The same procedure as explained in Section 4.6.2 was used and hence not repeated here. Values for  $\gamma \sim 8$  (or  $T_{t,max} \simeq 2.3 \text{ MPa}$ ) and  $\sim 3.6$  (or  $T_{t,max} \simeq 7.3 \text{ MPa}$ ) are obtained for uncoated CuLF-WMC and coated CuLF-MCE samples, respectively.

## 6.5 Conclusions

In this study, the mixed mode delamination behavior of (industrially relevant) uncoated CuLF-WMC interfaces and coated CuLF-MCE interfaces was characterized using the various methods and tools developed in this thesis. The CERR versus mode angle trends showed that the fracture toughness of the uncoated CuLF-WMC interface is approximately a factor of two higher than that of the coated CuLF-MCE interface over the full range of mode mixities. From the CERR versus mode angle trends, it was also observed that there is a difference in the coupling between different opening modes of the two interfaces. For example, in the case of coated CuLF-MCE, the influence of shear separation on normal traction was almost negligible for low mode angle tests until  $\psi = 25^\circ$ , whereas a more dominant shear contribution was observed in case of uncoated CuLF-WMC. The traction-separation behavior of the two interfaces revealed a pronounced difference in the maximum traction illustrating the big difference in the brittleness of the behavior between the two interfaces. *In-situ* microscopic visualization revealed the presence of a large fracture process zone with crack bridging in uncoated CuLF-WMC samples compared to a more localized, brittle de-adhesive failure mechanism in coated CuLF-MCE interface samples, partly explaining the observed differences in the CERR versus mode angle and measured traction-separation curves. However, the maximum length of bridging ligaments, observed from *in-situ* microscopic visualization, particularly in the uncoated CuLF-WMC interface, did not correspond with the fracture length scale of opening in the measured traction-separation law. Although, preliminary studies indicated that the presence of significant plastic deformation in the interfacial region, which is ignored during the visual crack bridge measurement, might be a possible cause for the observed discrepancy, further investigation is required for a complete understanding.



# Conclusion and Recommendations

---

## Abstract

The aim of this thesis was to develop an experimental-numerical methodology for characterization and prediction of interface delamination in dissimilar multi-layer systems. To achieve this goal, (i) an experimental setup suitable to characterize delamination in dissimilar bi-layer material systems was designed and realized, (ii) a numerical model that can simulate the irreversible loading-delamination-unloading behavior of the interface was formulated and (iii) a procedure to extract the relevant parameters of the interface from the delamination experiments was developed. In this chapter, the methods, analyses, results and conclusions of the thesis are briefly summarized and finally an outlook on future work is given.

## 7.1 Conclusions

The development of the experimental setup began with a literature review to evaluate the suitability of existing experimental setups for characterization of delamination and to identify the requirements for the new setup. Experimental methods based on linear elastic fracture mechanics (LEFM) approaches [11, 13, 17, 19–24, 26] are widely used in the literature for delamination studies. The critical load for delamination together with information about the crack length are the only values required from the experiment to obtain the interface toughness using existing LEFM approaches (assuming the geometry and material properties of the adherent layers are known). Unfortunately, this approach might fail for cases where the interface exhibits a relatively large fracture process zone (compared to the crack length) for at least two reasons: (i) the validity of LEFM solutions for interface toughness is questionable, and (ii) a description/characterization of the interface behavior with



only one parameter is insufficient. Therefore, detailed characterization of the fracture process zone is needed to quantify the behavior of such interfaces. Cohesive zone (CZ) models, where the shape of the constitutive law is a priori assumed and is described with at least two parameters (e.g. interface toughness and characteristic fracture length scale), are widely used to describe the behavior of such interfaces. This means that apart from the interface toughness, additional parameters that quantify the fracture processes within the process zone are needed from the delamination experiments. Moreover, the setup should allow for the measurement of interface toughness without any LFM solution. Many reports in the literature [34–39] have shown that the interface fracture toughness varies significantly with mode mixity. Therefore, the interface toughness should be evaluated over the full range of mode mixities. Although several experimental setups for mixed mode delamination characterization are available in the literature [21–25], they are not suitable for *in-situ* visualization of the delamination process under a microscope which is mandatory for the evaluation of details of the process zone (e.g. local crack opening displacement fields at the delamination front) to quantify the input parameters needed for CZ models.

Therefore, in Chapter 2, a novel Miniature Mixed Mode Bending (MMMB) delamination setup, capable of *in-situ* characterization of interface delamination in miniature multi-layer structures, was designed and realized. An inventive loading configuration in combination with friction free elastic hinges is employed in the setup to sensitively measure global load-displacement delamination curves for the full range of mode mixities from which the interface toughness or Critical Energy Release Rate (CERR) can be determined. The setup was designed to work in a horizontal plane with sufficiently small dimensions to fit in the chamber of a scanning electron microscope or under an optical microscope allowing visualization of the detailed real-time fracture process during delamination. Finite element analysis of the setup proved the capability of the new setup to achieve a full range of mode mixities, with a constant mode angle as a function of the crack length and crack opening displacement. Analysis of the loading configuration revealed that the conventional end notch flexure test (ENF) may not be a good representation of mode II delamination, because the friction (resulting from the compressive normal stresses) between the two layers in the cracked region during the ENF test can lead to overestimation of the mode II interface toughness. This problem can be circumvented in the new MMMB setup by performing a delamination test in a pure mode II loading configuration. The measurement concept of the new MMMB setup was successfully validated by testing homogeneous bilayer samples with a glue interface system over the full range of mode mixities. Finally, it was also demonstrated that the crack length can be measured more precisely and the delamination mechanism (crack bridging) can be seen more in detail by performing *in-situ* delamination tests.

The validation experiments (on the glue interface system) also revealed room for improvement of the measurement accuracy, robustness, and applicability. Therefore, in Chapter 3, further optimization in the design was performed by (i) optimizing the number and location of the hinges, (ii) optimizing the elastic hinge geometries

for increased maximum rotation, (iii) minimizing clearance in the connectors and (iv) increasing the robustness of the setup with additional guiding and alignment tools. A simple finite element beam model, where the arms of the setup were modeled with 2-node beam elements and the hinges were modeled using nodal ties and rotational springs, was employed for identifying the optimal number and location of the hinges. Optimization of the thickness of the hinge was done using a closed form compliance equation for elliptic hinges. It was demonstrated that the improved setup exhibits (i) a wider application range to more interface systems because of its significant increase of the maximum accessible load and stroke for all mode mixities, (ii) high accuracy in measuring the load-displacement response, as demonstrated from experiments on validation samples, confirming the significantly reduced hysteresis, (iii) excellent experimental reproducibility characteristics due to the newly added alignment tools. The maximum accessible load of the improved setup is 50 N whereas the maximum achievable displacement will depend on the geometry and the material properties of the adherents.

The improved setup was used for testing industrially relevant (coated) CuLF-MCE samples for the full range of mode mixities. As explained earlier, loading-delamination-unloading tests were used to calculate the CERR for different mode mixities. In addition to the CERR measurements, real-time microscopic visualization allowed for the identification of the difference in the crack growth behavior between different mode mixity tests and the correlation of the observed behavior with the measured CERR. A relatively brittle cleavage type of fracture was observed for the investigated CuLF-MCE samples, although at high magnification, limited crack bridging was observed.

In the delamination growth experiments conducted in this thesis, the energy dissipated in one loading-delamination-unloading cycle (i.e. the area under the load-displacement curve) is divided by the corresponding increase in crack length during that cycle and the sample width to obtain the interface fracture toughness. This procedure for determination of the interface toughness is valid for any size of fracture process zone and only assumes that (i) the size and shape of (a fully developed) process zone remain constant during the crack growth, (ii) the energy supplied to trigger delamination growth is stored elastically in the specimen structure, without any plastic dissipation in the adherent layers (an assumption that is also employed for LEFM approaches). Consequently, the interface toughness can be straightforwardly obtained from the measured load-displacement response of delamination growth experiments when there is no plasticity in the layers of the sample structure. However, there is much evidence in the literature showing that plasticity often does occur in the layers of the sample structure, particularly, if the layers forming the interface are ductile and the interface is strong. Consequently, it has been reported that large errors in the measurement of the interface fracture toughness can occur if these structural plastic dissipations are neglected. Moreover, *in-situ* SEM observation of delamination on different interface structures revealed (Chapter 2 and 3) failure mechanisms ranging from interface damage to interface plasticity. However, identification and separation of structural plasticity contributions to the total dissipated energy dur-

ing a delamination experiment is not trivial, particularly in the presence of plasticity mechanisms within the fracture process zone which is part of the interface fracture toughness. To be able to understand the individual contribution of structural and interface plasticity to the total energy dissipated during a delamination experiment and to the global retained opening of the sample after complete unloading, a numerical model that can incorporate both damage and plasticity behavior of the interface along with plastic behavior of the sample structure was developed.

For this purpose, a combined plasticity-damage cohesive zone model that allows for modeling of irreversible unloading behavior with partial damage and partial plasticity by extending the existing coupled mixed mode (loading) CZ models with unloading behavior was implemented and presented in Chapter 4. The combined plasticity-damage formulation is generic in the sense that it can be applied irrespective of the shape of CZ law used. In the current research, it was implemented based on the improved Xu-Needleman CZ law. The combined plasticity-damage behavior is accomplished by altering the ratio of the plastic energy and the total energy of the separation with one additional parameter called the plastic limit in addition to the standard CZ parameters (such as the interface toughness and critical displacement) that characterize the loading behavior of the traction-separation law used. The plastic limit was defined such that until the effective maximum separation of the cohesive zone reaches the plastic limit, the cohesive zone behaves fully elasto-plastic. Once the effective maximum separation passes the plastic limit, the plastically deformed cohesive zone damages with further separation. It was demonstrated that by varying the plastic limit from 0 to  $\infty$ , the irreversible interface behavior of the CZ can be varied from full damage to a mixture of damage and plasticity to full plasticity. The CZ with a plastic limit (and without plasticity in adherent layers) provided a way to model the global retained opening due to only interface plasticity for mode I and mixed mode situations. A hybrid approach was proposed and demonstrated to determine all parameters of the mixed mode CZ law for a glue interface system. In this approach, first, Andersson and Stigh's method [97] is used to extract mode I parameters. Then, the mode II interface strength (and critical opening displacement) was determined using the fracture toughness values obtained from mixed mode tests performed at different mode angles ranging from mode I to mode II. Finally, the plastic limit was determined from an analysis of displacement field maps obtained with digital image correlation.

In Chapter 5, a semi-analytical approach was proposed that can be used to account for structural plastic contributions to the total energy dissipated during delamination experiment to obtain an accurate value for the interface fracture toughness from a mode I experiment. This approach is based on reconstructing the force-displacement curve equivalent to the plasticity free case from the measured force-displacement response by identifying the individual contribution of the retained openings due to structural and interface plasticity to the total retained opening after complete unloading of the sample. This was achieved by assuming (for a given crack length) that (i) both the structural unloading stiffness and (ii) the critical load for delamination remain constant with and without structural plasticity. The partitioning of the individ-

ual contribution of structural plasticity and interface plasticity to the total retained opening is obtained by using retained crack opening profiles of the sample together with the assumptions that (iii) the size and shape of the process zone are constant and (iv) the sample structure deforms plastically only in the region surrounding the process zone. The proposed approach and underlying assumptions were numerically verified by employing a finite element model with the combined damage-plasticity cohesive zone elements at the interface. An experimental assessment performed on CuLF-MCE samples with different thicknesses of the CuLF layers demonstrated that the correction of the interface fracture toughness due to structural plasticity, resulting from this approach, was more than a factor of 2. This approach was developed such that it is generally applicable for most of the existing delamination growth experiments, as it only requires the determination of the crack opening displacement profile before and after the delamination test. Moreover, the approach requires neither any analytical solution or numerical simulation nor the constitutive behavior of the adherents. Finally, it is noted that the proposed approach is not applicable when the structural arms of the sample undergo plastic deformation during unloading (i.e. reverse plasticity), because reverse plasticity changes the structural unloading stiffness making assumption 1 no longer valid.

In Chapter 6, the experimental tools developed in this thesis were employed for the characterization of delamination in (i) coated CuLF-MCE interface samples (for which the CERR values were already determined in Chapter 3) and (ii) uncoated CuLF-new MCE interface samples. The differences in the measured load-displacement responses, CZ traction separation laws, CERR versus mode angle trends and the observed delamination mechanisms were discussed.

In summary, the combined application of *in-situ* MMMB experiments, the analytical procedure to determine the CERR, and the cohesive zone model with a parameter identification procedure allows for accurate characterization of delamination mechanism(s) and prediction of interface mechanics.

## 7.2 Recommendations

In this section, the recommendations for future work are formulated:

- It was identified that large errors might occur due to visual analysis of the crack tip data for measuring the crack length (or increase in crack length) which is necessary for interface toughness determination. Instead, it is recommended to use DIC measurements to determine the increase in crack length, as was demonstrated in this thesis.
- The thermo-mechanical processing history of manufacturing the multi-layer structures typically induces (large) residual stresses into the layers. The influence of residual stresses on the measured interface properties could be analyzed by using the *in-situ* capabilities of the current setup in combination with

DIC analysis. DIC measured displacement and strain fields might provide a way to measure the residual stresses in the delaminated layers which can be analyzed by comparing with the corresponding analytical [124] or numerical predictions.

- *In-situ* study of interface delamination behavior for varying environmental conditions (e.g. variable humidity and temperature) could be interesting to correlate (i) the variability of the interface properties with corresponding changes in the delamination mechanism and (ii) the dependency of interface properties on environmental conditions. The MMMB setup has been designed such that it is small enough to fit in a climate box [125] which fits under an optical microscope. Therefore, these studies can be readily performed by using the MMMB setup.
- The methodology to account for a structural plasticity contribution to the total energy dissipated needs to be extended to mixed-mode and mode II experiments. A similar procedure developed for mode I might be used but then the approach and assumptions should first be verified numerically and experimentally for mixed mode and mode II loading conditions. This could be done relatively easily by employing the ingredients developed in this thesis, i.e. the combined plasticity-damage mixed mode CZ model and the MMMB setup.
- The applicability of the combined plasticity-damage cohesive zone model can be broadened (for brittle interfaces) by using advanced adaptive interface elements (e.g. the self-adaptive enriched element developed by Samimi et al. [117]) which lead to better convergence.
- The developed combined plasticity-damage cohesive zone model can be extended to 3D without any expected fundamental limitations.
- Micro-scale experimental setups that can test (real size) interfaces in microsystems taken directly from the photo lithography/micro-fabrication line have been developed recently. Calibration or validation of such setups is needed and could be performed by using a combination of various tools (MMMB setup, combined plasticity-damage cohesive zone model) developed in this thesis.
- The MMMB setup developed in this project is suitable for testing a wide range of dissimilar interfaces but requires macro-scale samples. Nevertheless, the setup could still be used to test micron-scale interfaces, such as a stack of thin films on a substrate, by attaching a stiffener on top of the thin film stack [62]. This might provide a way to test 3D interface structures over the full range of mode mixities under *in-situ* SEM observation in order to identify the weak spots and to analyse plasticity in the thin film stack (e.g. using DIC).

# Bibliography

---

- [1] K. Bose, P. A. Mataga, and P. P. Castaneda. Improved impact and delamination resistance through interleaving. *Journal Key Engineering Materials*, 37:317–348, 1991.
- [2] N. Srikanth, L. Chan, and C. J. Vath-III. Adhesion improvement of EMC-lead frame interface using brown oxide promoters. *Thin Solid Films*, 504:397–400, 2006.
- [3] O. van der Sluis, R. A. B. Engelen, R. B. R. van Silfhout, W. D. van Driel, and M. A. J. van Gils. Efficient damage sensitivity analysis of advanced Cu/low-k bond pad structures by means of the area release energy criterion. *Microelectronics Reliability*, 47:1975–1982, 2007.
- [4] W. D. van Driel, M. A. J. van Gils, R. B. R. van Silfhout, and G. Q. Zhang. Prediction of delamination related IC and packaging reliability problems. *Microelectronics Reliability*, 45:1633–1638, 2005.
- [5] O. van der Sluis, C. A. Yuan, W. D. van Driel, and G. Q. Zhang. *Nanopackaging*. Springer US, 2009.
- [6] A. Todoroki, M. Tanaka, and Y. Shimamura. Electrical resistance change method for monitoring delamination of CFRP laminates: effect of spacing between electrodes. *Composites Science and Technology*, 65:37–46, 2005.
- [7] G. A. O. Davies, D. Hitchings, and J. Ankersen. Predicting delamination and de-bonding in modern aerospace composite structures. *Composites Science and Technology*, 66:846–854, 2006.
- [8] S. A. Taylor and D. J. Carr. Post failure analysis of  $0^0/90^0$  ultra high molecular weight polyethylene composite after ballistic testing. *Journal of Microscopy*, 196:249–256, 1999.
- [9] R. Okada and M. T. Kortschot. The role of the resin fillet in the delamination of honeycomb sandwich structures. *Composites Science and Technology*, 62:1811–1819, 2002.

- [10] C. C. Ciang, J-R. Lee, and H-J. Bang. Structural health monitoring for a wind turbine system: a review of damage detection methods. *Measurement Science and Technology*, 19(122001):1–20, 2008.
- [11] A. G. Evans, M. Ruhle, B. J. Dalgleish, and P. G. Charalambides. The fracture energy of bimaterial interfaces. *Material Science and Engineering*, A126:53–64, 1990.
- [12] H. Yu and J. W. Hutchinson. Delamination of thin film strips. *Thin Solid Films*, 423:54–63, 2003.
- [13] G. Dreier, M. Meyer, S. Schmauder, and G. Elssner. Fracture mechanics studies of thermal mismatch using a four-point bending specimen. *Acta Metallurgica and Materialia*, 40:S345–S353, 1992.
- [14] V. Gupta and A. Pronin. New technique to measure the toughness of thin-film interfaces. *Journal of American Ceramic Society*, 78(5):1397–1400, 1995.
- [15] A. A. Volinsky, J. B. Vella, and W. W. Gerberich. Fracture toughness, adhesion and mechanical properties of low-k dielectric thin films measured by nanoindentation. *Thin Solid Films*, 429:201–210, 2003.
- [16] W. Li and T. Siegmund. An analysis of the indentation test to determine the interface toughness in a weakly bonded thin film coating - substrate system. *Acta Materialia*, 52:2989–2999, 2004.
- [17] L. Banks-Sills, V. Boniface, and R. Eliasi. Development of a methodology for determination of interface fracture toughness of laminate composites - the  $0^\circ/90^\circ$  pair. *International Journal of Solids and Structures*, 42:663–680, 2005.
- [18] I. Ocaña, J. M. Molina-Aldareguia, D. Gonzalez, M. R. Elizalde, J. M. Sánchez, J. M. Martinez-Esnaola, J. Gil Sevillano, T. Scherban, D. Pantuso, B. Sun, G. Xu, B. Miner, J. He, and J. Maiz. Fracture characterization in patterned thin films by cross-sectional nanoindentation. *Acta Materialia*, 54:3453–3462, 2006.
- [19] Jy-An. J. Wang, I. G. Wright, M. J. Lance, and K. C. Liu. A new approach for evaluating thin film interface fracture toughness. *Material Science and Engineering A*, 426:332–345, 2006.
- [20] Yu-Fu Liu, Y. Kagawa, and A. G. Evans. Analysis of a barb test for measuring the mixed-mode delamination toughness of coatings. *Acta Materialia*, 56:43–49, 2008.
- [21] J. R. Reeder and J. R. Crews. Mixed mode bending method for delamination testing. *AiAA Journal*, 28(7):1270–1276, 1990.
- [22] W. O. Soboyejo, G. Y. Lu, S. Chengalva, J. Zhang, and V. Kenner. A modified mixed-mode bending specimen for the interfacial fracture testing of dissimilar materials. *Fatigue and Fracture of Engineering Materials and Structures*, 22:799–810, 1999.

- [23] C. C. Merrill and P. S. Ho. Effect of mode mixity and porosity on interface fracture of low-k dielectrics. In *Materials Research Society Symposium Proceedings*, volume 812, 2004.
- [24] N. Blanco, E. K. Gamstedt, J. Costa, and D. Trias. Analysis of the mixed-mode end load split delamination test. *Composite Structures*, 76:14–20, 2006.
- [25] J. Thijsse, O. van der Sluis, J. A. W. van Dommelen, W. D. van Driel, and M. G. D. Geers. Characterization of semiconductor interfaces using a modified mixed mode bending apparatus. *Microelectronics Reliability*, 48:401–407, 2008.
- [26] J. D. Gunderson, J. F. Brueck, and A. J. Paris. Alternate test method for interlaminar fracture toughness of composites. *International Journal of Fracture*, 143:273–276, 2007.
- [27] S. Yu. Grachev, A. Mehlich, J.-D. Kamminga, E. Barthel, and E. Sndergrd. High-throughput optimization of adhesion in multilayers by superlayer gradients. *Thin Solid Films*, 518:6052–6054, 2010.
- [28] V. Tvergaard and J. W. Hutchinson. The relation between crack growth resistance and fracture process parameters in elastic-plastic solids. *Journal of the Mechanics and Physics of Solids*, 40:1377–1397, 1992.
- [29] V. Tvergaard and J. W. Hutchinson. The influence of plasticity on mixed mode interface toughness. *Journal of the Mechanics and Physics of Solids*, 41:1119–1135, 1993.
- [30] V. Tvergaard and J. W. Hutchinson. On the toughness of ductile adhesive joints. *Journal of the Mechanics and Physics of Solids*, 44:789–800, 1996.
- [31] Y. Wei and J. W. Hutchinson. Nonlinear delamination mechanics for thin films. *Journal of the Mechanics and Physics of Solids*, 45:1137–1159, 1997.
- [32] Y. Wei and J. W. Hutchinson. Interface strength, work of adhesion and plasticity in the peel test. *International Journal of Fracture*, 93:315–333, 1998.
- [33] Q. D. Yang and M. D. Thouless. Mixed-mode fracture analyses of plastically-deforming adhesive joints. *International Journal of Fracture*, 110:175–187, 2001.
- [34] M. S. Hu and A. G. Evans. The cracking and decohesion of thin films on ductile substrates. *Acta Metallurgica*, 37(3):917–925, 1989.
- [35] J. W. Hutchinson and Z. Suo. Mixed mode cracking in layered materials. *Advances in Applied Mechanics*, 29:63–191, 1992.
- [36] L. Banks-Sills, Nahum Travitzky, and Dana Ashkenazi. Interface fracture properties of a bimaterial ceramic composite. *Mechanics of Materials*, 32:711–722, 2000.



- [37] A. Kuhl and J. Qu. A technique to measure interfacial toughness over a range of phase angles. *Journal of Electronic Packaging*, 122:147–151, 2000.
- [38] X. Q. Shi, X. R. Zhang, and J. H. L. Pang. Determination of interface fracture toughness of the adhesive joint subjected to mixed-mode loading using finite element method. *International Journal of Adhesion and Adhesives*, 26:249–260, 2006.
- [39] S. Tang, T. F. Guo, and L. Cheng. Rate dependent interface delamination in plastic IC packages. In *9th Electronics packaging technology conference*, pages 680–685, 2007.
- [40] H. Hirakata, T. Kitamura, and Y. Yamamoto. Evaluation of interface strength of micro-dot on substrate by means of afm. *International Journal of Solids and Structures*, 41:3243–3253, 2004.
- [41] K. L. Rugg, B. N. Cox, and R. Massab. Mixed mode delamination of polymer composite laminates reinforced through the thickness by z-fibers. *Composites Part A: Applied Science and Manufacturing*, 33:177–190, 2002.
- [42] M. J. van den Bosch, P. J. G. Schreurs, and M. G. D. Geers. On the prediction of delamination during deep-drawing of polymer coated metal sheet. *Journal of materials processing technology*, 209:297–302, 2009.
- [43] D. R. Bloyer, K. T. Venkateswara rao, and R. O. Ritchie. Fracture toughness and r-curve behavior of laminated brittle-matrix composites. *Metallurgical and Materials Transactions*, 29A:2483–2496, 1998.
- [44] K. L. Rugg, B. N. Cox, and R. Massab. Delamination failure mechanisms in microlayers of polycarbonate and poly (styrene-co-acrylonitrile). *Journal of Applied Polymer Science*, 68:798–805, 1998.
- [45] D. Dugdale. Yielding of steel sheets containing slits. *Journal of the Mechanics and Physics of Solids*, 8:100–104, 1960.
- [46] G. Barenblatt. The mathematical theory of equilibrium cracks. *Advances in Applied Mechanics*, 7:55–129, 1962.
- [47] M. Comninou. An overview of interface cracks. *Engineering Fracture Mechanics*, 37:197–208, 1990.
- [48] V. Tvergaard. Effect of fibre de-bonding in a whisker-reinforced metal. *Material Science and Engineering A*, 125:203–213, 1990.
- [49] A. Hillerborg. Application of the fictitious crack model to different types of materials. *International Journal of Fracture*, 51(2):95–102, 1991.
- [50] X. P. Xu and A. Needleman. Void nucleation by inclusion de-bonding in a crystal matrix. *Modeling and Simulation in Material Science and Engineering*, 1(2):111–132, 1993.

- [51] V. Tvergaard and J. W. Hutchinson. Effect of strain-dependent cohesive zone model on predictions of crack growth resistance. *International Journal of Solids and Structures*, 33:3297–3308, 1996.
- [52] G. T. Camacho and M. Ortiz. Computational modeling of impact damage in brittle materials. *International Journal of Solids and Structures*, 33:2899–2938, 1996.
- [53] M. G. A. Tijssens, B. L. J. Sluys, and E. van der Giessen. Numerical simulation of quasi-brittle fracture using damaging cohesive surfaces. *European Journal of Mechanics A: Solids*, 19:761–779, 2000.
- [54] M. Elices, G. V. Guinea, J. Gomez, and J. Planas. The cohesive zone model: advantages, limitations and challenges. *Engineering Fracture Mechanics*, 69:137–163, 2002.
- [55] B. F. Sørensen. Cohesive law and notch sensitivity of adhesive joints. *Acta Materialia*, 50:1053–1061, 2002.
- [56] T. E. Tay. Characterization and analysis of delamination fracture in composites: An overview of developments from 1990 to 2001. *Applied Mechanics Reviews*, 56(1):1–32, 2003.
- [57] S. Li, M. D. Thouless, A. M. Waas, J. A. Schroeder, and P. D. Zavattieri. Use of a cohesive-zone model to analyze the fracture of a fiber-reinforced polymer-matrix composite. *Composites Science and Technology*, 65:537–549, 2005.
- [58] M. J. van den Bosch, P. J. G. Schreurs, and M. G. D. Geers. An improved description of the exponential Xu and Needleman cohesive zone law for mixed-mode decohesion. *Engineering Fracture Mechanics*, 73:1220–1234, 2006.
- [59] B. A. E. van Hal, R. H. J. Peerlings, M. G. D. Geers, and O. van der Sluis. Cohesive zone modeling for structural integrity analysis of IC interconnects. *Microelectronics Reliability*, 47:1251–1261, 2007.
- [60] I. Ozdemir, W. A. M. Brekelmans, and M. G. D. Geers. A thermo-mechanical cohesive zone model. *Computational Mechanics*, 46(5):735–745, 2010.
- [61] A. G. Evans and J. W. Hutchinson. The thermo-mechanical integrity of thin films and multilayers. *Acta Metallurgica and Materialia*, 43(7):2507–2530, 1995.
- [62] R. H. Dauskardt, M. Lane, Q. Ma, and N. Krishna. Adhesion and de-bonding of multi-layer thin film structures. *Engineering Fracture Mechanics*, 61:141–162, 1998.
- [63] J. J. Vlassak, Y. Lin, and T. Y. Tsui. Fracture of organosilicate glass thin films: environmental effects. *Material Science and Engineering A*, 391:159–174, 2005.

- [64] ASTM-D-5528-01. *Standard test method for mode I interlaminar fracture toughness of unidirectional fiber-reinforced polymer matrix composites*, *Annual book of ASTM standards*, volume 15.03. American Society for Testing and Materials, West Conshohocken, PA., 2001.
- [65] L. A. Carlsson, J. W. Gillespie, and J. R. Pipes. On the analysis and design of the end notched flexure specimen for mode II testing. *Journal of Composite Materials*, 20:594–604, 1986.
- [66] B. F. Sørensen, K. Jørgensen, T. K. Jacobsen, and R. C. Østergaard. DCB-specimen loaded with uneven bending moments. *International Journal of Fracture*, 141:163–176, 2006.
- [67] B. D. Davidson and V. Sundararaman. A single leg bending test for interfacial fracture toughness determination. *International Journal of Fracture*, 78:193–210, 1996.
- [68] P. Davies, B. R. K. Blackman, and A. J. Brunner. Standard test methods for delamination resistance of composite materials: current status. *Applied Composite Materials*, 5:345–364, 1998.
- [69] A. J. Vinciquerra and B. D. Davidson. Effect of crack length measurement technique and data reduction procedures on the perceived toughness from four-point bend end-notched flexure tests. *Journal of Reinforced Plastics and Composites*, 23:1051–1062, 2004.
- [70] B. F. Sørensen, E. K. Gamstedt, R. C. Østergaard, and S. Goutianos. Micromechanical model of cross-over fibre bridging prediction of mixed mode bridging laws. *Mechanics of Materials*, 40:220–234, 2008.
- [71] ASTM-D-6671-01. *Standard test method for mixed mode I-mode II interlaminar fracture toughness of unidirectional fiber reinforced polymer matrix composites*, *Annual book of ASTM standards*, volume 15.03. American Society for Testing and Materials, West Conshohocken, PA., 2001.
- [72] P. Davies. Influence of ENF specimen geometry and friction on the mode II delamination resistance of carbon/PEEK. *Journal of Thermoplastic Composite Materials*, 10(4):353–361, 1997.
- [73] C. Fan, P. Y. Ben Jar, and J. J. Roger Cheng. A unified approach to quantify the role of friction in beam-type specimens for the measurement of mode II delamination resistance of fibre-reinforced polymers. *Composites Science and Technology*, 67:989–995, 2007.
- [74] Q. Bing and C. T. Sun. Effect of compressive transverse normal stress on mode II fracture toughness in polymeric composites. *International Journal of Fracture*, 145:89–97, 2007.

- [75] S. T. Smith, V. G. Badami, J. S. Dale, and Y. Xua. Elliptical flexure hinges. *Rev. Sci. Instrum.*, 68(3):1474–1483, 1997.
- [76] R. Boyer, G. Welsch, and E. W. Collings. *A materials properties hand book: Titanium alloys*. ASM international, 1994.
- [77] Z. Suo and J. W. Hutchinson. Interface crack between two elastic layers. *International Journal of Fracture*, 43:1–18, 1990.
- [78] S. Li, J. Wang, and M. D. Thouless. The effects of shear on delamination in layered materials. *Journal of the Mechanics and Physics of Solids*, 52:193–214, 2004.
- [79] T. C. Chu, W. F. Ranson, and M. A. Sutton. Applications of digital-image-correlation techniques to experimental mechanics. *Experimental Mechanics*, 25(3):232–244, 1985.
- [80] M. Lane, R. H. Dauskardt, A. Vainchtein, and H. Gao. Plasticity contributions to interface adhesion in thin-film interconnect structures. *Journal of Material Research*, 15(12):2758–2769, 2000.
- [81] S. Strohband and R. H. Dauskardt. Interface separation in residually-stressed thin-film structures. *Interface Science*, 11:309–317, 2003.
- [82] H. Y. Lee and G. S. Park. Failure paths at copper-base leadframe/epoxy molding compound interfaces. *Journal of Materials Science*, 37:4247–4257, 2002.
- [83] N. Tanaka, M. Kitano, T. Kumazawa, and A. Nishimura. Evaluating IC-package interface delamination by considering moisture-induced molding-compound swelling. *IEEE Transactions on Components and Packaging Technology*, 22(3):426–432, 1999.
- [84] F. M. Pan, S. R. Horng, T. D. Yang, and V. Tang. Studies of the interface between the epoxy molding compound and the copper lead frame by X-ray photoelectron spectroscopy, auger electron spectroscopy, and secondary electron spectroscopy. *Journal of Vacuum Science and Technology A*, (6):4074–4078, 1990.
- [85] L. Xu, X. Lu, J. Liu, X. Du, Y. Zhang, and Z. Cheng. Adhesion behavior between epoxy molding compound and different lead frames in plastic packaging. In *Proceedings of International Conference on Electronic Packaging Technology and High Density Packaging (ICEPT-HDP)*, pages 1039–1042, 2009.
- [86] A. Xiao, L. G. Wang, W. D. van Driel, L. J. Ernst, O. van der Sluis, D. G. Yang, and G. Q. Zhang. Characterization and modeling of thin film interface strength considering mode mixity. In *IEEE Transactions of Electronic Components and Technology Conference*, ISBN 1-4244-0985-3:1925–1930, 2007.
- [87] R. Borg, L. Nilsson, and K. Simonsson. Simulating DCB, ENF and MMB experiments using shell elements and a cohesive zone model. *Composite Science and Technology*, 64:269–278, 2004.

- [88] K. M. Liechti and Y. S. Chai. Asymmetric shielding in interfacial fracture under in-plane shear. *Journal of Applied Mechanics*, 59:295–304, 1992.
- [89] R. Rikards, F. G. Buchholz, H. Wang, A. K. Bledzki, A. Korjakin, and H. A. Richard. Investigation of mixed mode I/II interlaminar fracture toughness of the laminated composites by using a CTS type specimen. *Engineering Fracture Mechanics*, 61:325–342, 1998.
- [90] G. Wang, C. Merrill, J-H Zhao, and S. K. Groothuis. Packaging effects on reliability of cu/low-k interconnects. *IEEE Transactions on Device and Materials Reliability*, 3(4):119–128, 2003.
- [91] G. V. Marannano and A. Pasta. An analysis of interface delamination mechanisms in orthotropic and hybrid fiber-metal composite laminates. *Engineering Fracture Mechanics*, 74:612–626, 2007.
- [92] R. T. Tenchev and B. G. Falzon. A correction to the analytical solution of the mixed-mode bending (mmb) problem. *Composite Science and Technology*, 67:662–668, 2007.
- [93] M. Kolluri, M. H. L. Thissen, J. P. M. Hoefnagels, J. A. W. van Dommelen, and M. G. D. Geers. *In-situ* characterization of interface delamination by a new miniature mixed mode bending setup. *International Journal of Fracture*, 158:183–195, 2009.
- [94] G. Chen, J. Jia, and Q. Han. Geometrical profile optimization of elliptical flexure hinge using a modified particle swarm algorithm. *ICIC 2005, part I, LNCS 3644*, page 533–542, 2005.
- [95] G. Chen, X. Shao, and X. Huang. A new generalized model for elliptical arc flexure hinges. *Review of Scientific Instruments*, 79(095103):18, 2008.
- [96] M. Kolluri, M. H. L. Thissen, J. P. M. Hoefnagels, J. A. W. van Dommelen, and M. G. D. Geers. Study of interface delamination by a newly designed miniature mixed mode bending setup. In *Proceedings of European conference on fracture (ECF) 17, CD-ROM*, 2008.
- [97] T. Andersson and U. Stigh. The stress-elongation relation for an adhesive layer loaded in peel using equilibrium of energetic forces. *International Journal of Solids and Structures*, 41:413–434, 2004.
- [98] A. L. Loureiro, L. F. M. da Silva, C. Sato, and M. A. V. Figueiredo. Comparison of the mechanical behaviour between stiff and flexible adhesive joints for the automotive industry. *The Journal of Adhesion*, 86(7):765–787, 2010.
- [99] J. P. Parmigiani and M. D. Thouless. The effects of cohesive strength and toughness on mixed-mode delamination of beam-like geometries. *Engineering Fracture Mechanics*, 74:2675–2699, 2007.

- [100] Y. Freed and L. Banks-Sills. A new cohesive zone model for mixed mode interface fracture in bimetals. *Engineering Fracture Mechanics*, 75:4583–4593, 2008.
- [101] C. G. Davila, C. A. Rose, and P. P. Camanho. A procedure for superposing linear cohesive laws to represent multiple damage mechanisms in the fracture of composites. *International Journal of Fracture*, 158:211–223, 2009.
- [102] M. Ortiz and A. Pandolfi. Finite deformation irreversible cohesive elements for three dimensional crack propagation analysis. *International Journal for Numerical Methods in Engineering*, 44:1267–1282, 1999.
- [103] D. Xie and A. M. Waas. Discrete cohesive zone model for mixed-mode fracture using finite element analysis. *Engineering Fracture Mechanics*, 73:1783–1796, 2006.
- [104] S. Marzi, O. Hesebeck, M. Brede, and F. Kleiner. A rate dependent, elastoplastic cohesive zone mixed-mode model for crash analysis of adhesively bonded joints. In *7th European LS-DYNA conference*, 2009.
- [105] A. Biel and U. Stigh. Damage and plasticity in adhesive layer: an experimental study. *International Journal of Fracture*, 165:93–103, 2010.
- [106] M. Samimi, M. Kolluri, J. A. W. van Dommelen, and M. G. D. Geers. Simulation of interlaminar damage in mixed-mode bending tests using large deformation self-adaptive cohesive zones. (*to be submitted*).
- [107] M. Kolluri, J. P. M. Hoefnagels, J. A. W. van Dommelen, and M. G. D. Geers. An improved miniature mixed mode delamination setup for *in-situ* microscopic interface failure analyses. *Journal of Physics D: Applied Physics*, 44:1–13, 2011.
- [108] G. Barenblatt. The formation of equilibrium cracks during brittle fracture. general ideas and hypothesis: axysymmetrical cracks. *Journal of Applied Mathematics and Mechanics (PMM)*, 23:434–444, 1959.
- [109] A. Needleman. A continuum model for void nucleation by inclusion debonding. *Journal of Applied Mechanics*, 54:525–531, 1987.
- [110] A. Needleman. An analysis of decohesion along an imperfect interface. *International Journal of Fracture*, 42:21–40, 1990.
- [111] J. R. Rice and Jian sheng. Wang. Embrittlement of interfaces by solute segregation. *Materials Science and Engineering*, 109:23–40, 1989.
- [112] P.H. Geubelle and J. Baylor. Impact-induced delamination of laminated composites: a 2d simulation. *Composites, Part B*, 29:589–602, 1998.

- [113] N. Valoroso and R. Fedele. Characterization of a cohesive-zone model describing damage and de-cohesion at bonded interfaces. Sensitivity analysis and mode-I parameter identification. *International Journal of Solids and Structures*, 47:1666–1677, 2010.
- [114] M. J. van den Bosch, P. J. G. Schreurs, and M. G. D. Geers. A cohesive zone model with a large displacement formulation accounting for interfacial fibrillation. *European Journal of Mechanics*, 26(1):1–19, 2007.
- [115] A. Abdul-Baqi, P. J. G. Schreurs, and M. G. D. Geers. An improved description of the exponential Xu and Needleman cohesive zone law for mixed-mode decohesion. *International Journal of Solids and Structures*, 42:927–942, 2005.
- [116] Z. Y. Zhang and G. H. Paulino. Cohesive zone modeling of dynamic failure in homogeneous and functionally graded materials. *International Journal of Plasticity*, 21:1195–1254, 2005.
- [117] M. Samimi, J. A. W. van Dommelen, and M. G. D. Geers. An enriched cohesive zone model for delamination in brittle interfaces. *International Journal for Numerical Methods for Engineering*, 80:609–630, 2009.
- [118] B. F. Sørensen and T. K. Jacobsen. Determination of cohesive laws by the J integral approach. *Engineering Fracture Mechanics*, 70:1841–1858, 2003.
- [119] J-K. Kim and Y-W. Mai. High strength, high fracture toughness fibre composites with interface control – A review. *Composites Science and Technology*, 41(4):333 – 378, 1991.
- [120] N. Blanco, A. Turon, and J. Costa. An exact solution for the determination of the mode mixture in the mixed-mode bending delamination test. *Composite Science and Technology*, 66:1256–1258, 2006.
- [121] M. Kolluri, J. P. M. Hoefnagels, J. A. W. van Dommelen, and M. G. D. Geers. Modeling and characterization of irreversible mixed mode interface delamination using a cohesive zone with combined damage and plasticity. (*to be submitted*).
- [122] Q. D. Yang, M. D. Thouless, and S. M. Ward. Numerical simulations of adhesively-bonded beams failing with extensive plastic deformation. *Journal of the Mechanics and Physics of Solids*, 47:1337–1353, 1999.
- [123] M. D. Thouless, M. S. Kafkalidis, J. L. Adams, S. M. Ward, R. A. Dickie, and G. L. Westerbeek. Determining the toughness of adhesives in plastically-deforming joints. *Journal of Materials Science*, 33:189–197, 1998.
- [124] Chun-Hway Hsueh. Modeling of elastic deformation of multilayers due to residual stresses. *Journal of applied physics*, 91(12):9652–9657, 2002.

- 
- [125] W. D. van Driel, P. J. J. H. A. Habets, M. A. J. van Gils, and G. Q. Zhang. Characterization of interface strength as function of temperature and moisture conditions. In *Electronic Packaging Technology, 2005 6th International Conference on*, pages 1–6, 2005.





# Een *in-situ* experimenteel-numerieke aanpak voor karakterisatie van interface delaminatie

## Samenvatting

---

Interface delaminatie is een belangrijke uitdaging voor de betrouwbaarheid van composieten en microelektronische systemen door de integratie van verschillende materialen op kleine schaal. Delaminatie treedt op als gevolg van aanzienlijke spanningen op de interfaces, die bijvoorbeeld worden veroorzaakt door thermische belasting ten gevolge van de verschillen in thermische uitzettingscoëfficiënt en Poisson-verhouding tussen de aangrenzende lagen. Voorspellende eindige elementenmodellen worden gebruikt tijdens de ontwerp- en optimalisatiefase om het falen van deze materialen en systemen door delaminatie te minimaliseren. Succesvolle voorspelling is echter alleen mogelijk met een relevant interface model dat het (onomkeerbare) scheurinitiatie- en scheurgroegedrag beschrijft zoals waargenomen in experimenten. Dientengevolge, zijn toegespitste delaminatieproeven met *in-situ* microscopische visualisatie nodig om de relevante delaminatiemechanismen te identificeren en de grensvlakeigenschappen, zoals de scheurtaaiheid, nauwkeurig te meten als een functie van de belastingshoek, ook wel 'modehoek' genoemd. Daarom is het doel van dit onderzoek om experimenteel-numerieke instrumenten te ontwikkelen die nodig zijn voor nauwkeurige karakterisatie en voorspelling van interface delaminatie.

Als eerste stap om dit doel te bereiken, is een nieuwe Miniatuur Mixed Mode Buigopstelling (MMMB) ontworpen en gerealiseerd, waarmee grensvlakdelaminatie in kleinschalige multilaagstructuren *in-situ* kunnen worden gekarakteriseerd. De delaminatieopstelling past een inventief mechanisme toe om nauwkeurig het verband tussen de globale belasting en verplaatsing tijdens de scheurgroei onder elke modehoek te kunnen meten. Hiermee kan de scheurtaaiheid worden bepaald als functie van de modehoek. De opstelling is tevens voldoende klein om in de kamer van een scanning elektronenmicroscop (SEM) of onder een optische microscoop te passen, wat het mogelijk maakt de scheurgroei rechtstreeks onder hoge vergroting te volgen. De mogelijkheden van de opstelling zijn aangetoond met behulp van speciale interface preparaten, ondersteund door een eindige elementenanalyse. Het meetconcept is succesvol gevalideerd op metingen aan een preparaat van twee homogene lagen verbonden met een lijmlaag. De validatieproeven toonden ook ruimte voor verbetering van de meetnauwkeurigheid, robuustheid en toepasbaarheid. Daarom is het ontwerp verder geoptimaliseerd wat tot een verbeterde versie van de MMMB opstelling heeft geleid. Deze verbeterde opstelling is robuuster en kan een aanzienlijk groter scala aan grensvlaksystemen karakteriseren met een significant hogere nauw-

keurigheid en reproduceerbaarheid in de belasting-verplaatsingsmeting. Vervolgens is de potentie van de nieuwe in-situ experimentele techniek voor identificatie van de interface parameters gellustreerd. Onder andere is gedemonstreerd dat in-situ hoge resolutie SEM visualisatie van de lopende scheurgroei het mogelijk maakt de faalmechanismen van het grensvlak te identificeren en kwantitatieve rekvelden en scheuropeningsprofielen met behulp van digitale beeldcorrelatie te meten.

In-situ SEM observatie van het loslaten van verschillende interface structuren laat faalmechanismen zien variërend van schade tot plasticiteit in de grenslaag. Daarom is een model nodig dat het experimenteel waargenomen onomkeerbare belasting-ontlastingsgedrag van het grensvlak kan beschrijven. Wanneer zo'n model wordt gecomplementeerd in een eindige elementenmodel, kan, bijvoorbeeld, scheurvertakking en scheurpropagatie van meerdere grensvlakken nauwkeurig worden voorspeld. Een gecombineerde schade- en plasticiteitsformulering is ontwikkeld die geschikt is voor de modellering van interface ontlasting variërend van volledige schade tot volledige plasticiteit. De formulering introduceert een minimum aantal modelparameters, welke ook experimenteel kunnen worden bepaald. Het ontlastingsmodel kan worden gebruikt in combinatie met bestaande 'cohesive zone' beschrijvingen die worden gebruikt om de belasting van het grensvlak onder een gemengde modehoek te modelleren. De relevantie en de toepasbaarheid van het ontlastingsmodel zijn aangetoond, in combinatie met de zogenaamde 'verbeterde Xu-Needleman cohesive zone' beschrijving, door de schade en plasticiteit die beide zijn waargenomen tijdens het loslaten van bovengenoemde lijmlaagstructuren te modelleren. Bovendien is een procedure aangereikt om de modelparameters te identificeren.

Blijvende vervorming van de structuur van het preparaat treedt vaak op tijdens delaminatietests, in het bijzonder, als de lagen aangrenzend aan de interface ductiel zijn of de interface sterk is. Nauwkeurige bepaling van de scheurtaaiheid van de interface vereist daarom identificatie en scheiding van de bijdrage van structurele plasticiteit aan de totale energiedissipatie, waarbij rekening gehouden dient te worden met plastische mechanismen binnen de scheurzone van het grensvlak die bedragen aan de scheurtaaiheid van het grensvlak. Derhalve is een semi-analytische procedure ontwikkeld om voor de structurele plasticiteit in de lagen van het proefstuk te compenseren, ter verkrijging van een nauwkeurige waarde voor de scheurtaaiheid van de interface in een mode I experiment. De procedure is numeriek geverifieerd met behulp van een eindige elementenmodel met cohesive zone elementen (op het grensvlak). De voorgestelde procedure is experimenteel gecontroleerd door de scheurtaaiheid van de interface van industrieel relevante CuLF-MCE structuren (d.w.z. epoxycomposiet spuitgegoten op een koperen 'lead frame') te karakteriseren voor verschillende laagdiktes.

Samenvattend kan worden gesteld dat de gecombineerde toepassing van de in-situ MMMB experimenten, de semi-analytische procedure ter bepaling van de scheurtaaiheid, en het cohesive zone ontlastingsmodel met bijbehorende parameter identificatieprocedure het mogelijk maakt om delaminatiemechanisme(n) nauwkeurig te karakteriseren en de interface mechanica te voorspellen. Als demonstratie zijn twee

---

typen van de industrieel relevante CuLF-MCE structuren (met of zonder coating en met, respectievelijk, wit of zwart epoxycomposiet) in detail in kaart gebracht met het ontwikkelde experimentele gereedschap.



# Acknowledgements

---

There are many people who contributed for the successful completion of this PhD. I would like to express my gratitude to each and every one who helped directly or indirectly in making my journey smooth and successful, in the past four and half years.

First of all, I would like to thank my promoter prof. Marc Geers for giving me this opportunity to do PhD research in his group. Marc, it was really a wonderful experience to work under your esteemed guidance. Your inputs during monthly meeting discussions were truly valuable. I admire your constructive criticism which motivated me to keep the focus on my targets in finishing my PhD. Thanks a lot for all the support and guidance during the past four and half years.

Next, I like to acknowledge my daily supervisor, Johan Hoefnagels, for his extraordinary support and guidance in my day to day research activities. Johan, I really enjoyed all the lengthy (but very useful) discussions that we had during our regular weekly meetings as well as in the evening and weekend encounters. Especially, your pragmatic thinking combined with a never ending enthusiasm (that you have shown in our meetings) provided me with a good learning experience and interest towards research. Thank you very much for being always approachable, giving useful inputs and spending many extra office hours for me.

I also acknowledge my other daily supervisor, Hans van Dommelen, particularly for his supervision in the numerical part of my project. Being a metallurgist (before coming here) with no knowledge of numerical modeling, I wouldn't have been succeeded in modeling the interface behavior without his help and guidance. I also benefited from his valuable inputs during the MMMB setup design and from his judicious comments on my journal papers (and reports). Hans, thanks for everything.

I am grateful to the committee members, prof. M. Thouless, prof. A. Corigliano, prof.dr. A.H. Dietzel and prof.dr.ir. A. van Keulen for their critical comments to this thesis and their attendance to my defense. I also thank prof.dr. L.P.H. de Goey for being the chairman during my defense.

I would like to thank M2i for employing me and providing the required funding to carry out this research. I also like to acknowledge all the staff members of m2i office.

You are always helpful and easy to approach.

I am also grateful to our industrial partners (from Philips), dr.ir. Olaf van der Sluis and dr.ir. Ruud Vonken for their very healthy cooperation through out this project. My special thanks go to dr. ir. Peter Timmermans from Philips for arranging many different batches of samples in very short time notice periods.

I am very grateful to Erwin Dekkers from GTD for his creative ideas and valuable inputs during the setup design. I extend my thanks to Jeroen Baijens, Peter Minten, Patrick de Laat and Marielle from GTD and Sjef from work shop for their help in the design and manufacturing of the setup and for the fast delivery of the samples.

Many thanks go to Marc van Maris for his assistance in all the experiments I performed (in multi-scale lab) for this thesis. Marc, your extraordinary support in the lab made my life easier. It was really nice to work with you.

I also thank Ron, Piet, Leon and other Mate staff members for sharing their knowledge through nice presentations and discussions.

I specially thank our system administrator Leo Wouters for his timely assistance in all computer related issues. I like to thank Alice, Yvon and Marleen for always being helpful in all matters.

I am very thankful to all my students, Thijs, Robert, Caspar and Lianne for their valuable contributions to this thesis.

Furthermore, I want to thank M. K. Singh (thanks for your help when I first arrived here), Cem (thanks for all your guidance in the lab), Rudy (I still remember, you helped me out with my moving), Peter (thanks for inviting for your wedding), Mohammad (sorry man, I bothered you a lot for m2i quarterly reports), Lambert (very helping, you even fixed lights in my house), Tomas (good Czech friend), Marco (thanks for your CZ files), Lars (thanks for arranging dinner parties), Britta (thanks for attending my wedding), Erica (thanks for clarifying MSc. Marc and Matlab issues), Bhairav, Muge, Matej, Frederico, Izzet, Tuncay, Ana, Graham, Sabastiaan, Vinayak, Tom Engels, Gwen, Petra, Mieke, Carlos, Pooya, Isa, Poh, Michael, Reza, Amin, Michel, Joris, Jan, Rick, Jeroen, Daniel, Salim, Yang, Lieke, David and all my friends and colleagues at the university who made my life more enjoyable at the university.

I want to express my special thanks to Hamid for being my true companion at the university for the past four and half years. I still remember the first day that we met in the Crown inn hotel in centrum when we came here for the interview. I always cherish all the chit chats and discussions we had. Thanks for being such a good friend.

I also thank Loes for her special care and love on my wife. Loes, I always remember your help and support during my wife's hospitalization.

I also want to thank all my Indian friends here, Ravi, Jogi-Sushu, Madan-Rithika, Gopi-Sravani, Shazi, Guna-Purnima, Vamsi-Sirisha, Ujjwal, Kaushik-Kamakshi, Sunil, Prasanna, Jagan-Surya, Vamsi, Sekhar-Vasanthi, Srinidhi, Kiran, Yogesh (Bhai), Sridhar, Raghu-Teja, Tiru, Suresh, Muru, Raj, Satya-Sudha, Siva Ram-Bhargavi and

Bharat-Shilpa for making me feel at home. It was fun spending time with them with lot of parties, cinemas, combined cooking, AH coffees, night walks, week end gatherings, card games, small trips, Indian festival celebrations. I extend my thanks to my friends back at home, Ramki, Rajesh, Guppu, Kiran, Hari, Veera, Vyshnu, Ravi, Prasad, KD, Kota, Paladi and Suresh for their support and friendship.

I am also grateful to my masters supervisors prof. U. Ramamurty and dr. S. Karthikeyan for guiding and helping me in finding a good PhD position.

Then, I move on to my parents who always supported me morally, monetarily and physically for all the endeavors in my life. Thanks *amma*, thanks *nannagaru*. Without your blessings, support and love I wouldn't have reached to this stage. I also want to thank my *sister-bava* (for their love), *father-in-law*, *mother-in-law*, *naveen*, *vamsipriya*, *jaggampeta ayagaru-aama*, *babai*, *sita pinni*, *bavani akka-bavagaru*, *harika-naveen* and all my cousin sisters and brothers and other relatives for their support and good wishes.

Last but not least, I would love to express my deep gratitude to my wife, *Sowjanya*, for her enormous love and support, particularly, in final stressful phase of my PhD. *Sowju*, without your cooperation this journey wouldn't have been possible. Thank you and I love you for always being with me during all the ups and downs.

Murthy Kolluri

Eindhoven, April 2011.





# Curriculum Vitae

---

Murthy Kolluri was born on September 5th 1980 in Rajanagaram, India. After finishing his high school education in 1996 at Zilla Parishad High School Rajanagaram in India, he obtained in 1999 a (pre-university) diploma in metallurgical engineering at the Government Polytechnic College Visakhapatnam in India. He continued his education in metallurgical engineering to obtain a Bachelor of Technology (B.Tech.) degree in 2004 from the National Institute of Technology, Warangal, and the Master of Engineering (ME) degree in 2006 from the Indian Institute of Science, Bangalore, India. His master thesis research on "Strain hardening and fatigue in metal foams: The effect of constraint" was done under the supervision of Prof. U. Ramamurty at the department of Materials Engineering. In December 2006, he moved to the Netherlands to work as an M2i PhD researcher in the group of Prof. Marc Geers in the department of Mechanical Engineering at the Eindhoven University of Technology. His PhD research was on developing an in-situ experimental-numerical approach for interface delamination characterization. The results of his PhD research are presented in this dissertation.